People's Democratic Republic of Algeria

Ministry of Higher Education and Scientific Research

UNIVERSITY OF ABBES LAGROUR KHENCHELA

Faculty of Sciences and Technology

Department of Material Sciences

Order N°:

Serial N°:

THESIS

For obtaining the LMD Doctorate Degree in Chemistry

Specialty: materials chemistry

Presented by:

Khemissi LAHOUEL

Entitled

Synthesis and characterisation of pure and doped metal oxide thin films for photocatalytic and ultraviolet photodetector applications

Publicly defended on: 21/06/2026

In front of the Jury committee composed of:

Mrs. Amel MESSAI	Professor	University of Khenchela	President
Mr. Abdecharif BOUMAIZA	Professor	University of Khenchela	Supervisor
Mr. Abdelkader DJELLOUL	Professor	University of Khenchela	Co-Supervisor
Mrs. Sabrina ROGUAI	Professor	University of Khenchela	Examiner
Mr. Salah Eddine DJILANI	Professor	Universite of Annaba	Examiner
Mr. Noureddine DADDA	MCA	Universite of Annaba	Examiner

Academic Year: 2025-2026

Acknowledgments

I want to convey my profound gratitude to Allah for the strength, endurance, and confidence. He has imparted to me the ability to accomplish this task.

I would like to convey my profound appreciation to my thesis supervisor, ***Professor Abdecharif*** **BOUMAIZA**, *and my co-supervisor,* ***Professor Abdelkader DJELLOUL****, for their enduring patience, tenacity, steadfast support, and excellence in their invaluable guidance, which informed and enhanced my journey throughout this endeavour.*

I like to convey my profound appreciation to the jury members for the privilege they grant me by consenting to assess and critique this work.

Mrs Amel MESSAI*, a professor at the University of Khenchela*

Mrs Sabrina ROGUAI*, professor at the University of Khenchela*

Mr Salah Eddine DJILANI, *professor at the University of Annaba*

Mr Noureddine DADDA*, Ph.D. in Chemistry (MCA) at the University of Annaba*

I am profoundly appreciative of all my educators for their indispensable assistance and unwavering encouragement during my path.

To my friends, colleagues, and everyone, the spirit of camaraderie and support you have shown has been a source of strength and joy.

It was a significant honour for me to complete this thesis at the Laboratory for Structures, Properties, and Interatomic Interactions (LASPI²A).

Dedication

To my esteemed parents,

May this endeavour be the realisation of your frequently spoken desires and the result of your numerous deeds of dedication.

To my dear sisters and brothers,

I am at a loss for words to convey my love and appreciation for having you as siblings.

To my heart,

You are the light of my life, you are the dream I never stop dreaming, the wish I have always had.

To my cherished flowers, Arinas, Amaris, and Numenssa,

whose smiles and purity have brightened my journey and perpetually sustained my inspiration and happiness. You are my profound inspiration and the impetus for my daily self-improvement.

to all teachers and professors in the world without exception.

To all those whose assistance and smiles have illuminated my journey.

K. LAHOUEL

Abstract

This research examines the manufacture of pure zinc oxide thin films doped with sulfur and then cadmium. were applied to glass substrates using the sol-gel method and dip coating technique, prior to the systematic evaluation of their various properties.

Structural (X-ray diffraction: XRD), morphological (field-emission scanning electron microscopy: FE-SEM), compositional (energy-dispersive X-ray spectroscopy: EDS), topographic (high-resolution atomic force microscopy: AFM), and optical (UV-visible spectroscopy) analyses were employed to characterise the fabricated films.

The photocatalytic effectiveness of the films was assessed by degrading methylene blue (MB) under direct sunlight for 120 minutes, utilising cadmium-doped ZnO. The photocatalytic increase of sulfur-doped ZnO transpires in 90 minutes under sunlight and 50 minutes under UV irradiation.

An enhancement in photocurrent characteristics, including sensitivity, responsivity, and detectivity, was noted following doping with sulfur and cadmium.

The best photocatalytic performance was attained with the 3% cadmium-doped zinc oxide sample and the 2% sulfur-modified zinc oxide sample. Following six test cycles, the samples exhibited enhanced reusability, recoverability, and stability, with just a minor decline, suggesting promising potential for diverse technological applications, validating their efficacy for wastewater treatment.

Keywords: S-modified ZnO, Cd-doped ZnO, Dip coating, Thin films, Wastewater treatment, Photocurrent, Photocatalytic, Sunlight illumination, UV irradiation.

Contents

Acknowledgements i

Dedication ii

Abstract iii

List of Figures vii

List of Tables x

List of Abbreviations xi

General Introduction 1

Chapter I Overview of Zinc Oxide Thin Film Properties and Their Uses

I.1 Introduction 4

I.2 Theoretical background of thin films 4

I.2.1 Definition 4

I.2.2 Thin film growth mechanisms 4

I.3 Semiconductors 5

I.3.1 Definition 5

I.3.2 Classification of Semiconductor 7

I.3.2.1 Intrinsic Semiconductor 7

I.3.2.2 Extintrinsic Semiconductor 8

I.3.3 Semiconductor based on metal oxides 8

I.3.4 Transparent conductive oxides (TCO) 9

I.4 Zinc Oxide 9

I.4.1 General properties of ZnO 10

I.4.1.1 Structural proprieties 10

I.4.1.2 Electronic and optical proprieties 10

I.4.1.3 Chemical and catalytic proprieties 13

I.4.1.4 Main proprieties of defects in ZnO 14

I.4.2 Applications of ZnO 14

I.5 Photocatalytic oxidation process 15

I.5.1 Advantages and disadvantages of ZnO thin film photocatalyst 16

I.5.2 General photocatalytic mechanism of ZnO thin film 18

I.5.3 Kinetics of photocatalytic reaction 19

I.5.3.1 Pseudo first ordre 19

I.5.3.2 Pseudo second ordre 20

I.5.4 Factors affecting photocatalytic efficiency 21
I.5.5 Photocatalyst deactivation 26
I.6 UV photodetection application 27
1.6.1 Fundamentals of photodetectors 27
1.6.2 Classification of UV photodetectors 27
1.6.3 Performance parameters of photodetectors 29
Chapter II Deposition and Characterization Techniques of Thin Films
II.1 Introduction 33
II.2 Thin film deposition techniques 33
II.2.1 Sol-gel technique 34
II.2.2 Dip coating 35
II.2.2.1 Step dip coating process 35
II.2.2.2 Thickness of the film in the dip-coating 36
II.2.2.3 Control of microstructure 38
II.2.2.4 Advantages of dip coating 39
II.2.2.5 Disadvantages of dip coating 40
II.2.2.6 Various factors influencing dip coating 40
II.3 Characterisation techniques of thin film 41
II.3.1 X-ray diffraction analysis (XRD) 41
II.3.2 Morphological analysis 45
II.3.3 Energy Dispersive X-ray Spectroscopy analysis (EDX or EDS) 47
II.3.4 Atomic force microscope analysis (AFM) 48
II.3.5 Optical analysis (UV-VIS Spectroscopie) 49
Chapter III Synthesis and characterisations of pure ZnO and sulfur-modified Zinc oxide thin layers for optoelectronic and environmental applications
III.1 Introduction 53
III.2 Thin film manufacturing 53
III.2.1 Preparing the substrate 53
III.2.2 Chemical and materials 54
III.2.3 Synthesis of thin films 54
III.3 Results and discussion 54
III.3.1 Structural investigation 54
III.3.2 Morphological investigation 57

III.3.3 Topographical investigation (AFM) 61

III.3.4 Optical investigation 63

III.4 Photocatalytic investigation 66

III.4.1 Experimental protocol 66

III.4.2 Photodegradation of MB 67

III.4.3 Photodegradation kinetic study 71

III.4.4 Mechanism of photodegradation behavior 72

III.4.5 Trapping test 74

III.4.6 Reusability test 75

III.5 Photodetection investigation 77

III.6 Conclusion 80

Chapter IV Synthesis and Characterisations of pristine ZnO and cadmium-modified Zinc oxide thin layers for optoelectronic and environmental applications

IV.1 Introduction 83

IV.2 Thin film manufacturing 83

IV.2.1 Preparing the substrate 83

IV.2.2 Chemical and materials 83

IV.2.3 Synthesis of thin films 83

IV.3 Results and Discussion 84

IV.3.1 Structural investigation 84

IV.3.2 Morphological investigation 87

IV.3.3 Topographical investigation (AFM) 91

IV.3.4 Optical investigation 93

IV.4 Photocatalytic activity study 95

IV.4.1 Photodegradation of MB 96

IV.4.2 Mechanism of photodegradation behaviour 99

IV.4.3 Trapping element study 101

IV.4.4 Stability and reusability study 103

IV.5 Photodetection investigation 105

IV.6 Conclusion 107

General Conclusions and future works 109

Bibliography 111

List of Figures

Figure I.1	The growth models of the thin films	**5**
Figure I.2	Band gaps of different solid materials	**6**
Figure I.3	Energy Band Diagram of intrinsic Semiconductor at (**a**) Temperature = 0 K, and (**b**) Temperature > 0 K	**7**
Figure I.4	The wurtzite structure of ZnO. The tetrahedral coordination of Zn-O is shown. Source: Reprinted with permission from	**10**
Figure I.5	Brillouin zone of a wurtzite crystal. The coordinates of some points are A2(0,0,1/2c), L2(0,1/3a,1/2c), M 2(0,1/3a,0), H2(1/3a,1/3a,1/2c), K2 (1/ 3a,1/3a,0)	**12**
Figure I.6	Band structures of wurtzite ZnO	**13**
Figure I.7	Applications of ZnO in different fields	**15**
Figure I.8	Advantages and disadvantages of different forms of photocatalyst	**17**
Figure I.9	General photocatalytic degradation mechanism of ZnO	**19**
Figure I.10	Degradation efficiency and surface area of (0–1.5%) W-doped TiO2 in the presence of xylene under the following conditions: light intensity = 132.6 W/m², [xylene] = 0.05 mL, flow rate = 300 mL/min	**22**
Figure I.11	Effect of band gap on photocatalytic performance	**24**
Figure I.12	The mechanism of metal doping on metal oxide semiconductor for enhanced photocatalytic activity	**25**
Figure I.13	Diagrammatic illustration of the different types of photodetectors (**a**) phototransistor (**b**) photoconductor (**c**) photodiode	**29**
Figure II.1	Thin film deposition technique classification	**33**
Figure II.2	Thin film deposition using the sol gel method	**34**
Figure II.3	Dip-coating process levels	**36**
Figure II.4	Areas of dip coating film development	**37**
Figure II.5	Schematic depiction of the dip-coating procedure	**39**
Figure II.6	A graphic depiction of the interaction between X-rays and matter, along with the condition for reflection as defined by Bragg's law	**42**
Figure II.7	Brucker D8 ADVANCE diffractometer	**43**
Figure II.8	Schematic diagram of FESEM (a) and its operating principle (b), and The Thermo Scientific Quattro S, FESEM equipment (c).	**46**
Figure II.9	(a) Graphical representation of X-ray emission during electron-atom interaction, and (b) Conventional interactions between electrons and specimens in the electron microscope.	**47**

Figure II.10	Schematics of atomic force microscopy operation (static mode)	**48**
Figure II.11	(**a**) Single beam UV-Vis transmission setup with the monochromator positioned before to the sample, and (**b**) the SpectroScan 80D device with V-770 spectrophotometer	**49**
Figure. III.1	Demonstrates the procedure for preparing thin film samples via dip coating methodology	**53**
Figure III.2	(**a**) XRD patterns of pure and sulfur-doped ZnO nanostructured thin films at varying sulfur doping concentrations; (**b**) strong diffraction peaks (002) in the XRD of the samples	**55**
Figure III.3	Structural parameters: (**a**) crystallite size, micro-strain, and dislocation density; (**b**) bond length, X-ray density, and specific surface area	**57**
Figure III.4	SEM images of (**a**) ZnO, (b) 2% S-ZnO, (**c**) 5% S-ZnO thin films	**59**
Figure III.5	Histograms distribution of grain size for samples (**a**) ZnO, (b) 2% S, and (**c**) 5% S-ZnO, together with (**d**) porosity and average grain size	**60**
Figure III.6	The EDS pictures of the as-deposited films: (**a**) ZnO, (**b**) 2% S-ZnO, and (**c**) 5% S-ZnO	**61**
Figure III.7	2D and 3D AFM images, along with a zoomed-in view of (**a**) ZnO, (**b**) 2% S-ZnO, and (**c**) 5% S-ZnO thin films	**63**
Figure III.8	(**a**) Transmission and (**b**) refractive index curves as a function of wavelength for deposited layers	**64**
Figure III.9	Energy gap measurements of the synthesized specimens	**66**
Figure III.10	MB absorbance at various time intervals with pure ZnO and S-doped ZnO catalysts under UV and solar exposure	**69**
Figure III.11	Degradation rate of MB over time for pure and S-doped ZnO under (**a**) UV radiation and (**b**) sunlight presence	**71**
Figure III.12	The reaction kinetics of methylene blue dye degradation for pure ZnO and sulfur-doped ZnO thin films under (**a**) ultraviolet and (**b**) solar light	**72**
Figure III.13	Mechanism of photocatalytic MB degradation in S-doped ZnO films	**73**
Figure III.14	Effectiveness of MB degradation over the 2% S-ZnO catalyst in the absence and presence of various scavengers under (**a**) UV irradiation, and (**b**) sunlight illumination	**74**
Figure III.15	Evaluation of the reusability of the 2% S-ZnO thin film for MB dye through photocatalytic testing under (**a**) UV rays, (**b**) sunlight exposure, and (**c**) XRD analysis following the sixth cycle of photocatalytic studies	**77**
Figure III.16	Schematic for a fabricated photodetector device	**79**
Figure III.17	Current measured as a function of voltage in darkness mode and under UV light for	**80**

	pure ZnO, 2% S-doped ZnO, and 5% S-doped ZnO thin films	
Figure IV.1	(a) XRD intense diffraction peaks (002) of samples, (b) XRD patterns of undoped and Cd-doped ZnO nanostructured thin films	**87**
Figure IV.2	FESEM images of (**a**) ZnO, (**b**) 3% Cd-ZnO, (**c**) 7% Cd-ZnO, (**c**), 10% Cd-ZnO thin films	**89**
Figure IV.3	The EDS images of as-deposited layers (**a**) ZnO, (**b**) 3% Cd-ZnO, (**c**) 7% Cd-ZnO, and (**d**) 10% Cd-ZnO	**90**
Figure IV.4	2D AFM images of (**a**) ZnO, (**b**) 3% Cd-ZnO, (**c**) 7% Cd-ZnO, and (**d**) 10% Cd-ZnO thin films	**92**
Figure IV.5	3D AFM images of (**a**) ZnO, (**b**) 3% Cd-ZnO, (**c**) 7% Cd-ZnO, and (**d**) 10% Cd-ZnO thin films	**92**
Figure IV.6	Transmission spectra as a function of the wavelength and photon energy for all deposited films	**93**
Figure IV.7	refractive index spectra as a function of the wavelength for all deposited films	**94**
Figure IV.8	(**a**), and (**b**) Energy gap values of the prepared samples	**95**
Figure IV.9	MB absorbance at different time intervals in the presence of ZnO, and Cd-doped ZnO catalysts under sunlight irradiation	**97**
Figure IV.10	Photocatalytic efficiency of pure and Cd-doped ZnO of MB as a function of time under sunlight exposure	**98**
Figure IV.11	Photocatalytic dye degradation kinetics of the prepared pure and Cd-doped ZnO thin films	**98**
Figure IV.12	Photocatalytic dye degradation mechanism of Cd-ZnO film	**101**
Figure IV.13	Degradation efficiency of MB over the 3% Cd-ZnO catalyst in the absence and presence of different scavengers under sunlight irradiation	**102**
Figure IV.14	Photocatalytic test of reusability of the 3% Cd-ZnO thin film for MB dye under sunlight irradiation, (**b**) XRD pattern, and (**c**) FESEM after the sixth cycle of photocatalytic experiments	**104**
Figure IV.15	Schematic for a fabricated photodetector device	**105**
Figure IV.16	Current measured as a function of voltage in darkness mode and under UV light for (**a**) pure ZnO, (**b**) 2% S-doped ZnO, and (**c**) 5% S-doped ZnO thin films	**107**

List of tables

Table III.1	Structural properties obtained from XRD data for all thin films produced via the dip coating process	**57**
Table III.2	The mean roughness, root mean square roughness, and surface area of the samples were determined using Gwyddion software based on AFM images	**62**
Table III.3	The gap energy, thickness, average refractive index (obtained from the curve), and refractive index measured via the Hervé-Vandamme model were examined using UV-visible spectroscopy measurements	**65**
Table III.4	Kinetic characteristics for each catalyst, including sulfur-doped ZnO	**68**
Table III.5	Recently published studies on metal and non-metal doped ZnO nanomaterials for the photocatalytic destruction of organic contaminants	**70**
Table III.6	Recycling of the catalyst, reaction duration, and degradation effectiveness (D) of methylene blue for 2% S-doped ZnO	**76**
Table III.7	Photocurrent performance of pure and sulfur-doped ZnO thin films measured at 5 volts	**78**
Table IV.1	Structural parameters derived from XRD data for all thin films deposited using the dip coating technique.	**86**
Table IV.2	The Grain size, and porosity of the samples were calculated using ImageJ software based on FESEM images	**88**
Table IV.3	Root mean square roughness, mean roughness, and surface area of the samples were calculated using Gwyddion software based on AFM images	**91**
Table IV.4	The gap energy, average refractive index (derived from the curve), refractive index computed via the Hervé-Vandamme model, and sample thickness were assessed using UV-visible spectroscopy measurements	**95**
Table IV.5	Kinetic parameters for each catalyst, both undoped and cadmium-doped ZnO	**97**
Table IV.6	Reusability of the catalyst, reaction time, and degradation efficiency (D) of methylene blue for 3% Cd-doped ZnO	**104**
Table IV.7	Photocurrent performance of pure and sulfur-doped ZnO thin films measured at 12 volts	**106**

List of Abbreviations

XRD: X-ray diffraction.

SEM: Scanning Electron Microscopy.

FESEM: Field Emission Scanning Electron Microscopy.

AFM: Atomic Force Microscopy.

EDS or EDX: Energy Dispersive X-ray Spectroscopy.

MB: Methylene blue.

JCPDS: Joint Committee on Powder Diffraction Standards.

ICDD: International Centre for Diffraction Data.

ZnO: Zinc oxide.

EDTA: Ethylenediaminetetraacetic Acid.

IPA: Isopropyl alcohol.

AscA : L-ascorbic acid.

CN: Cupric nitrate.

2D: Two-dimensional.

3D: Three-dimensional.

S: Sulfur.

Cd: Cadmium.

CO_2: Carbon dioxide.

H_2O: Water.

CB: Conduction band.

VB : Valence band.

UV : Ultraviolet.

VIS : Visible.

a, b, c: Lattice parameters.

V_{cell}: Unit cell volume.

$D_{(hkl)}$: The crystallite size.

$\varepsilon_{(hkl)}$: Lattice strain.

$B_{(hkl)}$: The width at half height.

FWHM: Full Width at Half Maximum.

$\delta_{(hkl)}$: Dislocation density.

$R_{(hkl)}$: Degree of crystal lattice distortion.

$APF_{(hkl)}$: Atomic Packing Factor.

$\rho_{X\text{-}ray}$: X-ray density.

S*: Surface area.

$\theta_{(hkl)}$: The diffraction angle.

Sin: Sinus.

Cos: Cosinus.

tan: Tangente.

Z: Atomic number.

λ: The wavelength (nm).

d_{hkl}: Interplanar spacing.

hkl: Miller indices.

°C: Degre Celsius.

K: Kelvin.

w: Watt.

Sol-gel : Solution-gelation.

PVD : Physical vapor deposition.

CVD: Physical vapor deposition.

Eg: Band gap energy.

h+/e-: Electron-hole pair.

OH^-: Ion hydroxyde.

H^+: Ion hydrogène.

$^{\bullet}OH$: Hydroxyl radical.

$^{\bullet}O_2^-$: Superoxide radical.

H_2O_2: Peroxide.

ROS: Reactive oxygen species.

pH: Potential of hydrogen.

V: Volt.

s: Second.

cm: Centimeter, **mm:** millimeter, **µm:** micrometer, **nm:** nanometer, and **Å:** Angstrom.

KeV : Kilo electron Volt.

UV-Vis : Ultraviolet-Visible.

e: Thickness of layer.

α: The absorption coefficient.

k: Extinction coefficients.

n: Refractive Index

I: Transmitted light.

I_0: Incident light.

A: Absorbance.

T: Transmittance.

R: Reflectance.

A_0: Area of Sample.

h: Planck's constant.

v: Photon frequency.

Hz: Hertz.

Iph: Photocurrent.

J_d : Dark current density.

I_{light} (Ion): light current.

I_d (Iof): dark current.

P_{in}: incident light power.

h: Planck's constant.

c: speed of light.

q: elementary charge.

λ: wavelength.

C_0 (A_0): The initial concentration.

Ct (At): The concentration after time t of irradiation.

k: rate constant.

S: sensitivity.

R: responsivity.

D^*: detectivity.

General Introduction

In recent years, a lot of researchers have proven the exclusive properties of nano-thin layers that pertain to the semiconductor material family, due to their distinct features, which have been revealed in both theoretical and applied investigations. They are being used in many potential applications, such as, antimicrobial, antibacterial, and photocatalytic activities [1]. In this respect, a number of metal oxide-based semiconductor materials have been investigated; among these, ZnO and doping ZnO have garnered interest due to their varied characteristics. ZnO has exceptional stability in n-type semiconducting materials that are both chemically and thermally stable, making it appropriate for a variety of applications in transparent electronics and optoelectronics [2].

Currently, a number of techniques are employed to deposit layers, including as co-precipitation, electrochemical, spray pyrolysis, and pulsed laser deposition. Among these techniques, the sol-gel method is usually used in both laboratory and industrial settings because of its advantages over alternative methods, which include low cost, the potential for large-scale production, precise control over the thickness and shape of the film, and low fabrication temperature [3], [4], [5].

The goal of this work is to develop and analyze thin films based on ZnO deposited on glass substrates by sol-gel dip-coating method and their application in dye removal and photodetectors.

This work is organized into three chapters:

First chapter, a theoretical and literature review research is done to provide an explanation for understanding the objective of the experimental results in the following chapters. Where the first part of this chapter presents a brief description of semiconductor materials and the thin film growth mechanism. Additionally, a detailed description of the thin film deposition methods and physicochemical characterization tools (X-Ray Diffraction, morphological: AFM and FESEM and UV-vis spectrophotometry) that were used in this work will also be presented. The development of semiconductor applications, particularly their function in photocatalytic activity and UV photodetection applications. In addition, it talks about Zinc oxide, doping ZnO, defects types, the structural, optical and electronic properties.

Second chapter, an overview of the most common chemical and physical methods used for the production of thin films will be presented. We will choose some of the methods, and specifically the technique used for preparing our films, then explanation of the experimental protocols and

methodologies employed for the characterization of all samples.

***Third* chapter**, aimed to synthesize pure ZnO and Sulfur-doped ZnO thin films by dip coating method. The obtained specimens were investigated employing structural, morphological, and optical characterization techniques. The pristine and doped thin films also were tested in the photocatalytic degradation activity for methylene blue dye under both direct sunlight and UV irradiation. It also explores the potential of all samples for photodetector applications.

Fourth chapter, presents the results associated with the preparation and characterization of undoped and Cd-doped ZnO thin films. Additionally, the photocatalytic and photocurrent properties of ZnO doped with Cd are discussed.

Finally, this thesis ends with a general conclusion that highlights the basic and significant results obtained from this study and ends with perspectives.

Chapter I Overview of ZnO Thin layer Properties and Their Uses

I.1 Introduction

Currently, thin films are utilized significantly owing to their unique chemical, physical, electrical, magnetic, optical, and mechanical capabilities. The attributes can be regulated by modifying their crystal structure, composition, and dimensions. Recently, researchers have demonstrated considerable interest in nano-sized metal-oxide-based semiconductors due to their potential for many physicochemical applications. Among these, ZnO thin films are distinguished by their efficiency, chemical durability, minimal toxicity, and narrow energy band gap. ZnO thin films are notably important for applications like water splitting, CO_2 reduction, sensors, and photocatalysis.

I.2 Theoretical background of thin films

II.2.1 Definition

A thin film is a layer that stretches endlessly in two dimensions while being constrained in the third dimension, with a thickness ranging from several nanometers to a few micrometers. The primary benefit of thin film technology is the minimization of dimensions and the adjustment of material characteristics. Additional thin films facilitate cost reduction and downsizing of the device [6]. The characteristics of the films are primarily influenced by their structure; however, the mechanical and thermal properties are contingent upon the reaction conditions and deposition techniques employed [7].

I.2.2 Thin film growth mechanisms

Thin films are produced through the deposition of atomic material onto a substrate. The standard thin film growth process on a substrate by the deposition of material atoms is illustrated in Figure. I.1.

Thin-film growth shows following features:

- **a.** The formation of thin films from various materials using any deposition technique begin with a stochastic nucleation process, succeeded by nucleation and growth phases.
- **b.** The stages of nucleation and growth are contingent upon several deposition parameters, including growth temperature, growth rate, and substrate chemistry.
- **c.** The nucleation stage can be substantially altered by external factors, such as electron or ion bombardment.
- **d.** The microstructure of films, the corresponding defect structure, and film stress are reliant upon the deposition conditions during the nucleation phase.

e. The crystal phase and orientation of the films are determined by the deposition conditions.

The fundamental properties of thin films, including chemical composition, structural characteristics, and thickness, are regulated by the deposition conditions. The thin films display distinctive features not present in bulk materials:

- Distinct material characteristics arising from the atomic development process on the substrates during growth.
- Size effects, especially quantum size effects, are defined by thickness, crystal orientation, and multilayer qualities.

Bulk materials are typically sintered from powdered raw materials. The powder's particle size is around 1 µm in diameter. Thin films are produced from ultrafine particles, specifically atoms or clusters of atoms. Ultra uniform compound materials may be generated through atomic collisions among adatoms on a substrate surface.

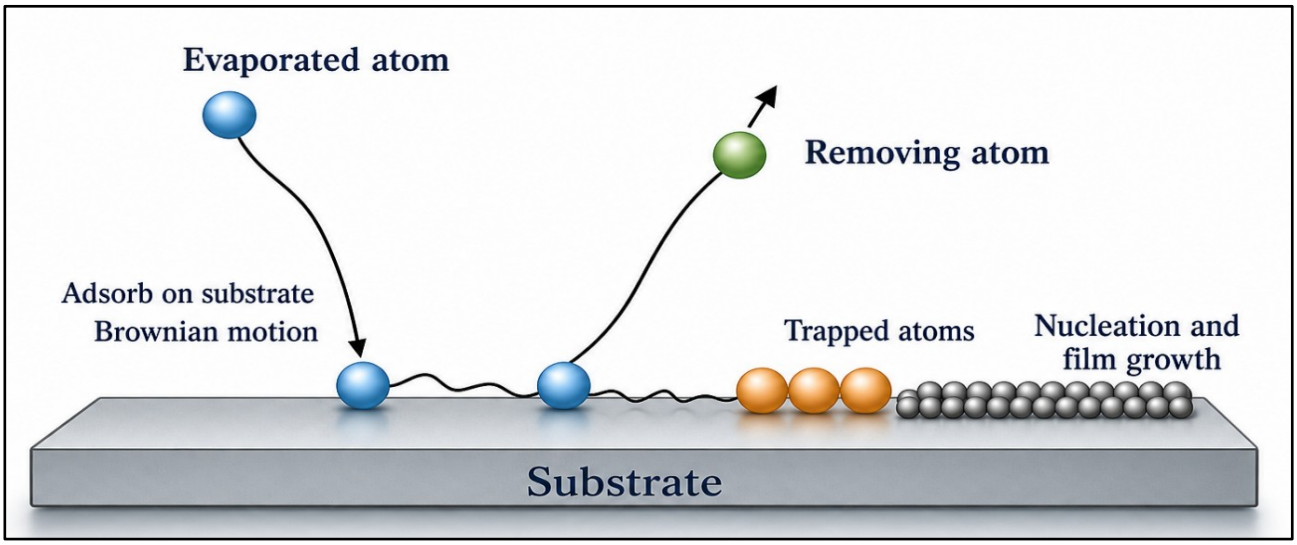


Figure I.1: The growth models of the thin films [8].

I.3 Semiconductors

I.3.1 Definition

Semiconductors are solid materials that are neither excellent conductors (metals) nor insulators (glass), possessing a crystalline structure and containing a minimal number of free electrons at ambient temperature. They possess resistivities and energy gaps that are intermediate between those of conductors and insulators. Their conductivity exceeds that of dielectrics but is inferior to that of conductors [1]. Figure I.2 elucidates the energy band gap of insulators, semiconductors, and conductors (metals).

Semiconductors function as insulators at ambient temperature; however, their electrical conductivity enhances with rising temperature, in contrast to metals [1]. The conductivity of semiconductors can be regulated by the introduction of appropriate impurities. Examples of semiconductors include silicon, germanium, and carbon. Semiconductors constitute the fundamental component of contemporary electronics, encompassing transistors, solar cells, light-emitting diodes (LEDs), and both digital and analog integrated circuits. The contemporary comprehension of semiconductor qualities is grounded in quantum physics, which elucidates the behavior of electrons and holes inside a crystal structure and a lattice. Enhanced knowledge about semiconductor materials and fabrication techniques has facilitated ongoing progress in the complexity and speed of microprocessors.

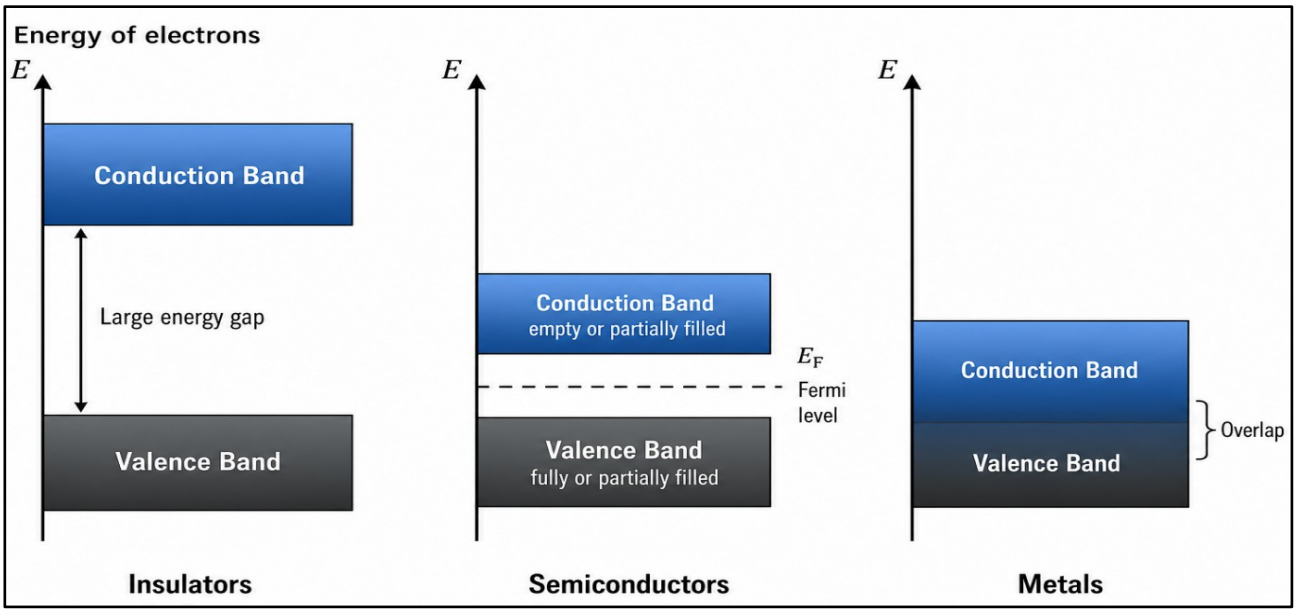


Figure I.2: Band gaps of different solid materials [1].

Semiconductor devices have various advantageous characteristics, including unidirectional current conduction, changeable resistance, and sensitivity to light or heat. The electrical characteristics of semiconductor materials can be altered through the deliberate introduction of impurities or the application of electric fields or light, enabling semiconductor devices to function in amplification, switching, and energy conversion. Current conduction in a semiconductor transpires via the mobility of free electrons and "holes," collectively referred to as charge carriers. The introduction of impurity atoms to a semiconductor, termed "doping," significantly enhances the quantity of charge carriers present. A semiconductor predominantly containing free holes is termed "p-type," whereas one primarily including free electrons is

referred to as "n-type". Semiconductor materials utilized in electronic devices are doped under specific conditions to regulate the position and concentration of p- and n-type dopants.

I.3.1 Classification of semiconductors

Semiconductors can be generally categorized into intrinsic and extrinsic types. Intrinsic semiconductors, also known as pure or undoped elements (Si, Ge), compare with extrinsic semiconductors, which are doped with other materials, referred to as impurities, and can be classified as n-type or p-type.

I.3.2.1 Intrinsic semiconductors

An intrinsic semiconductor is defined as a highly pure semiconductor material, characterized by an equal number of holes and electrons in the conduction band, as illustrated in Figure I.3. The forbidden energy gap in these semiconductors is minimal, allowing room temperature energy to suffice for valence electrons to transition to the conduction band. A defining trait of intrinsic semiconductors is that their Fermi level is situated between the valence band and the conduction band. When a potential difference is provided across an intrinsic semiconductor, electrons migrate towards the positive terminal, whereas holes drift towards the negative terminal. The total current within the semiconductor is a total of the current generated by free electrons and holes. An increase in the temperature of the semiconductor results in a rise in the number of hole-electron pairs and an enhancement in the current flowing through the semiconductor. If the temperature decreases, the opposite occurs [9]. In other terms, it is contingent upon temperature.

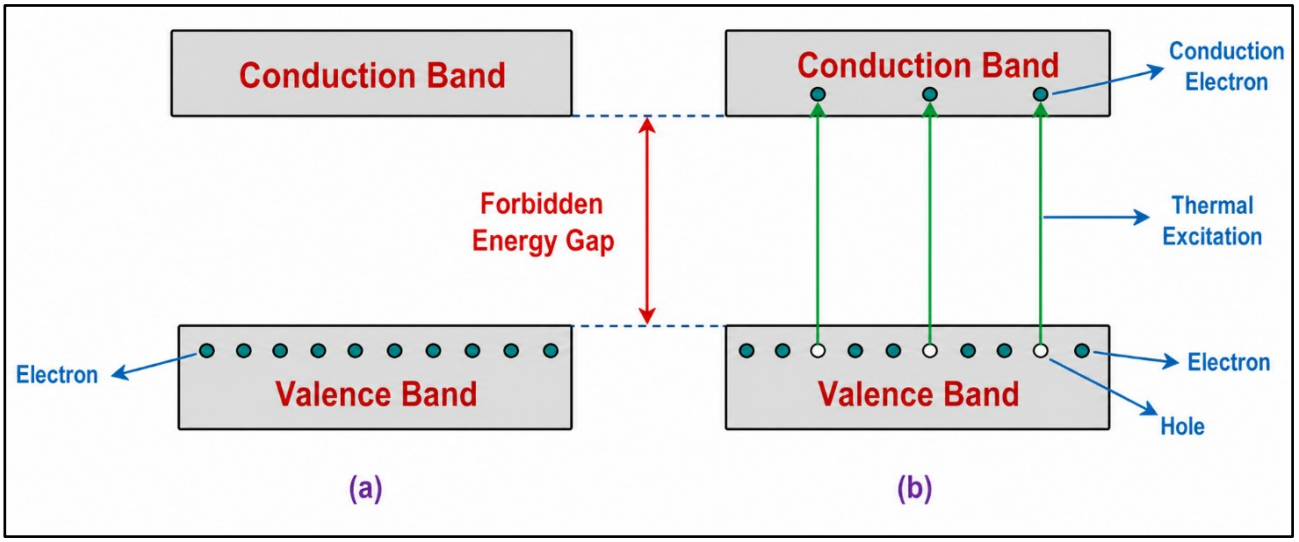


Figure. I.3: Enegy Band Diagram of intrinsic Semiconductor at (a) Temperature = 0 K, and (b) Temperature > 0 K [1].

I.3.2.2 Extrinsic semiconductors

These are semiconductors in which the pure status of the semiconductor material is intentionally compromised by the addition of small quantities of elements. This enhances their conductivity and characteristics relative to intrinsic semiconductors. The impurities are referred to as dopants or doping agents. When trivalent (3 electrons) or pentavalent (5 electrons) materials are employed as dopants in a tetravalent base material (e.g., Ge), p-type or n-type semiconductors are produced subsequently. The trivalent atom, such as boron, provides three electrons to the tetravalent atom, resulting in one unoccupied position that requires an electron. This results in a greater number of holes than electrons, and it is referred to as a p-type semiconductor. In p-type semiconductors, holes serve as the predominant charge carriers, while electrons function as the minority carriers. Conversely, when a pentavalent dopant like antimony gives an additional electron to the crystal structure, which is unnecessary for covalent bonding, the electron moves to the conduction band. This electron does not create a matching hole in the valence band due to its excess presence; hence, upon doping with such a substance, the base material possesses a greater number of electrons than holes, thus the term n-type extrinsic semiconductors. In n-type materials, electrons serve as the predominant carriers of current, whereas holes function as the minority carriers. The Fermi level resides about equidistant between the valence band and the conduction band, ascending in n-type materials and descending in p-type materials.

I.3.3 Semiconductors based on metal oxides

Metal oxide semiconductors (MOS) constitute a distinct category of materials owing to their electronic charge transport characteristics in contrast to traditional covalent semiconductors like silicon (Si). Metal oxide semiconductors are valence compounds characterized by a significant degree of ionic bonding. The conduction band minimum (CBM) and valence band maximum (VBM) mostly comprise the metal (M) ns and oxygen (O) 2p orbitals, respectively. The interaction between metal and oxide orbitals leads to a substantial discrepancy in charge carrier transport. Generally, the M ns orbitals exhibit considerable dispersiveness, but the O 2p orbital is confined, resulting in a decreased effective mass for electrons in comparison to holes. Conventional metal oxide semiconductors, including In_2O_3, ZnO, and SnO_2, along with their solid solutions, primarily exhibit n-type conductivity.

Conversely, to attain p-type conductivity in metal oxides, the effective mass of holes must be considerably reduced. This necessitates a higher dispersive VBM. The essential factor for achieving dispersive valence band maximum in metal oxides is the design of materials

incorporating metal cations that contribute occupied d or s states in proximity to the valence band maximum. The resultant p–d and p–s combination of the metal cation and oxygen orbitals amplifies the dispersion of the valence band maximum, hence diminishing the effective mass of holes. Numerous families of metal oxides have been identified as potential p-type semiconductors, such as NiO and Cu_2O [10].

I.3.4 Transparent conductive oxides (TCO)

Transparent conducting oxide (TCO) layers are defined as thin films that have both great transparency in the visible spectrum and electrical conductivity. The predominant TCO materials are n-type semiconductors, wherein defects such oxygen vacancies, impurity replacements, and interstitials provide electrons to the conduction band, hence supplying charge carriers for electric current flow [11]. Nonetheless, hole doping through ionized cation vacancies, impurity acceptor ion replacements, and/or oxygen interstitials that function as electron acceptors is feasible, resulting in p-type TCO materials. The first report on transparent conducting thin films of cadmium oxide (CdO) was released in 1907 by Badekar [12]. Who synthesized the films using thermal oxidation of sputtered cadmium films. Since then, significant advancements have been made in TCO technology to develop new varieties of TCOs with diverse applications [13]. The prominent and extensively utilized transparent conductive oxides (TCOs) encompass SnO2: Sb/F, ZnO:In/Al/F/B/Ga, In2O3: Sn/F/Sb/Pb, and Cd2SnO4, among others, alongside emerging TCOs such as Zn2SnO4, ZnSnO3, GaInO3: Ge/Sn, AgInO2: Sn, MgIn2O4, CdSb2O6: Y, Zn2In2O5, ZnGa2O4, In4Sn3O12, and CdIn2O4: Sn.

I.4 Zinc oxide

Zinc oxide (ZnO) is an II-VI semiconductor characterized by a broad band gap of 3.37 eV at ambient temperature. ZnO, as a multifunctional semiconductor, has been the subject of study for over 80 years since the 1930s. The first study phase culminated in the end of the 1970s and the beginning of 1980s, focusing mostly on bulk ZnO. It subsequently diminished, primarily due to the challenges associated with doping ZnO for both n- and p-type conductivity. Since the mid-1990s, the capabilities of ZnO have been reexamined, resulting in extensive documentation focused on applications in UV/blue optoelectronics, including light-emitting diodes, lasers, photodetectors, radiative-resistive electronic devices, diluted or ferromagnetic materials, nanoscale energy harvesting devices, and cost-effective TCO alternatives to ITO. is important to highlight that a significant advantage of ZnO is the availability and low cost of Zn metal, which enables the extensive manufacturing and utilization of ZnO-related materials and devices.

I.4.1 General properties of ZnO

I.4.1.1 Structural properties of ZnO

ZnO predominantly crystallizes in a hexagonal wurtzite form with lattice parameters a = 3.25 Å and c = 5.20 Å, as illustrated in Figure I.4. This structure generates spontaneous polarization along the c-axis. This property promotes the preferential growth of ZnO crystals, films, and nanostructures along the [0001] direction, as well as the manifestation of piezoelectric and thermoelectric phenomena in these materials [14].

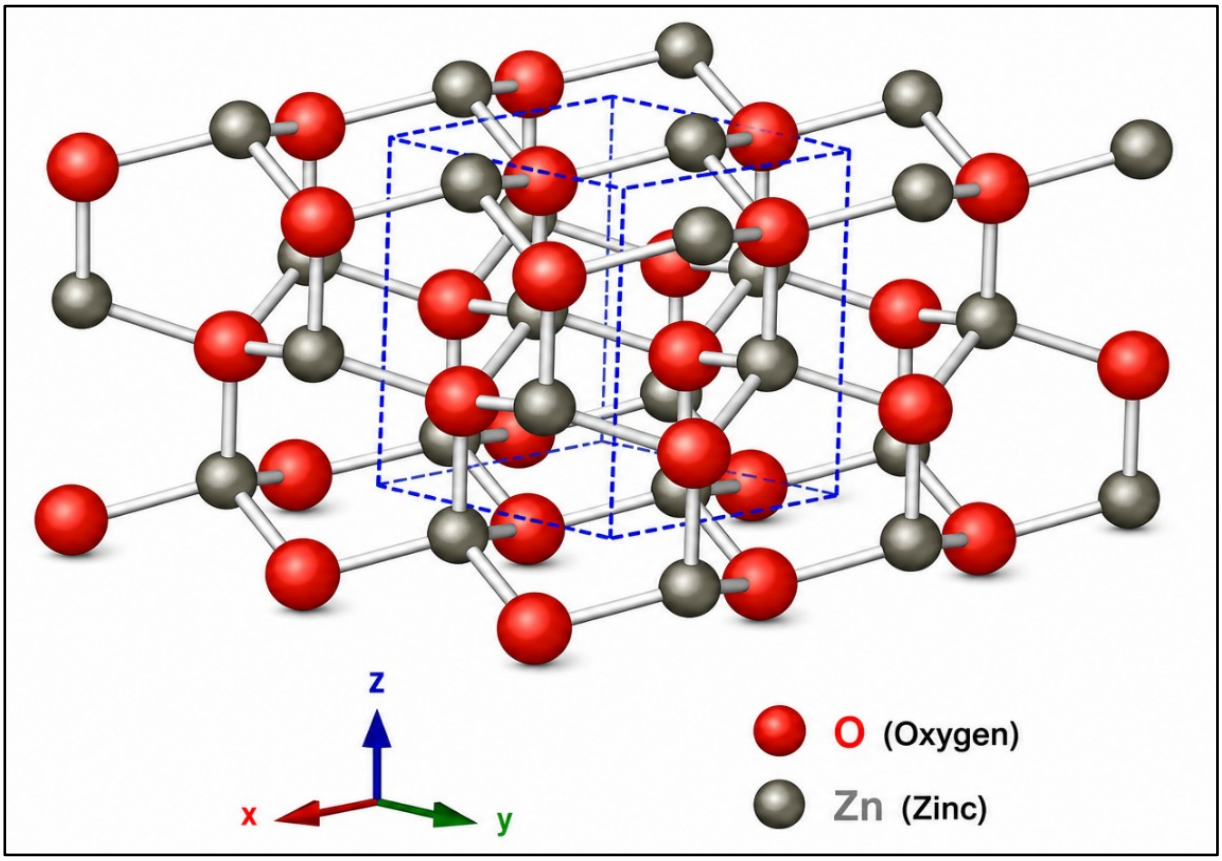


Figure I.4: The wurtzite structure of ZnO. The tetrahedral coordination of Zn-O is shown. *Source*: Reprinted with permission from [14].

I.4.1.2 Electronic and optical properties

Zinc oxide as a transparent material with a refractive index of 2 in its bulk state; however, in thin film form, its refractive index and absorption coefficient depend on the processing conditions. According to various authors, the refractive index value varies between 1.90 and 2.20 [15]. This material can transmit over 90% of visible light, dependent to possessing sufficient crystalline quality, owing to its large band gap. To accurately comprehend the electrical and dynamic properties of materials, it is essential to grasp the Brillouin zone

corresponding to their crystal structure. Figure I.5 illustrates the Brillouin zone corresponding to the wurtzite structure of ZnO, featuring multiple high symmetry points. The Γ-A direction aligns with the z-axis in actual space.

The band structure of ZnO is associated with its crystallographic structure and the electronic configurations of oxygen ($1s^2 2s^2 2p^4$) and zinc ($1s^2 2s^2 2p^6 3s^2 3p^6 3d^{10} 4s^2$), wherein the 2p states of oxygen comprise the valence band and the 4s states of zinc form the conduction band of the ZnO semiconductor. Figure I.6 illustrates the separation of these two bands. This image illustrates the presence of a vacant band of roughly 3.37 eV at 300 K [16]. This band represents the band gap of the material. Another significant aspect depicted in the image is that in reciprocal space, the point Γ, where k=0, corresponds to an absolute lowest energy of the conduction band and an absolute maximum energy of the valence band, so classifying ZnO as a direct band-gap semiconductor. This final point is critically significant for optics, particularly relevant for optoelectronic applications in the near-ultraviolet (UV) spectrum at 380 nm. Another significant characteristic of ZnO is its robust excitonic binding energy, approximately 60 meV. This is frequently referenced as facilitating radiative recombination of the electron-hole pair and reducing the excitation threshold for stimulated emission. The exciton strength in GaN is roughly 20 meV.

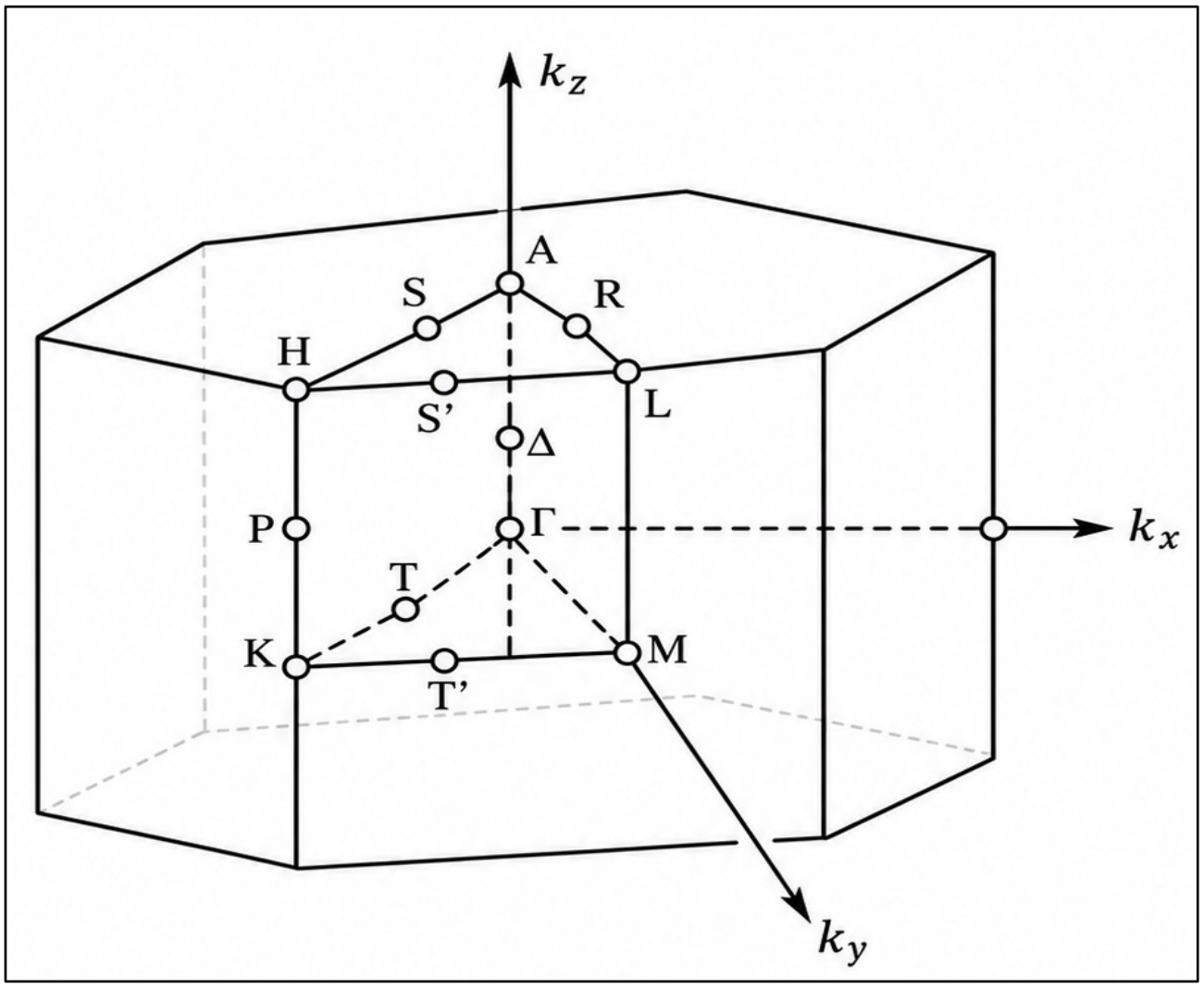


Figure I.5: Brillouin zone of a wurtzite crystal. The coordinates of some points are A2(0,0,1/2c), L2(0,1/3a,1/2c), M 2(0,1/3a,0), H2(1/3a,1/3a,1/2c), K2 (1/ 3a,1/3a,0) [16].

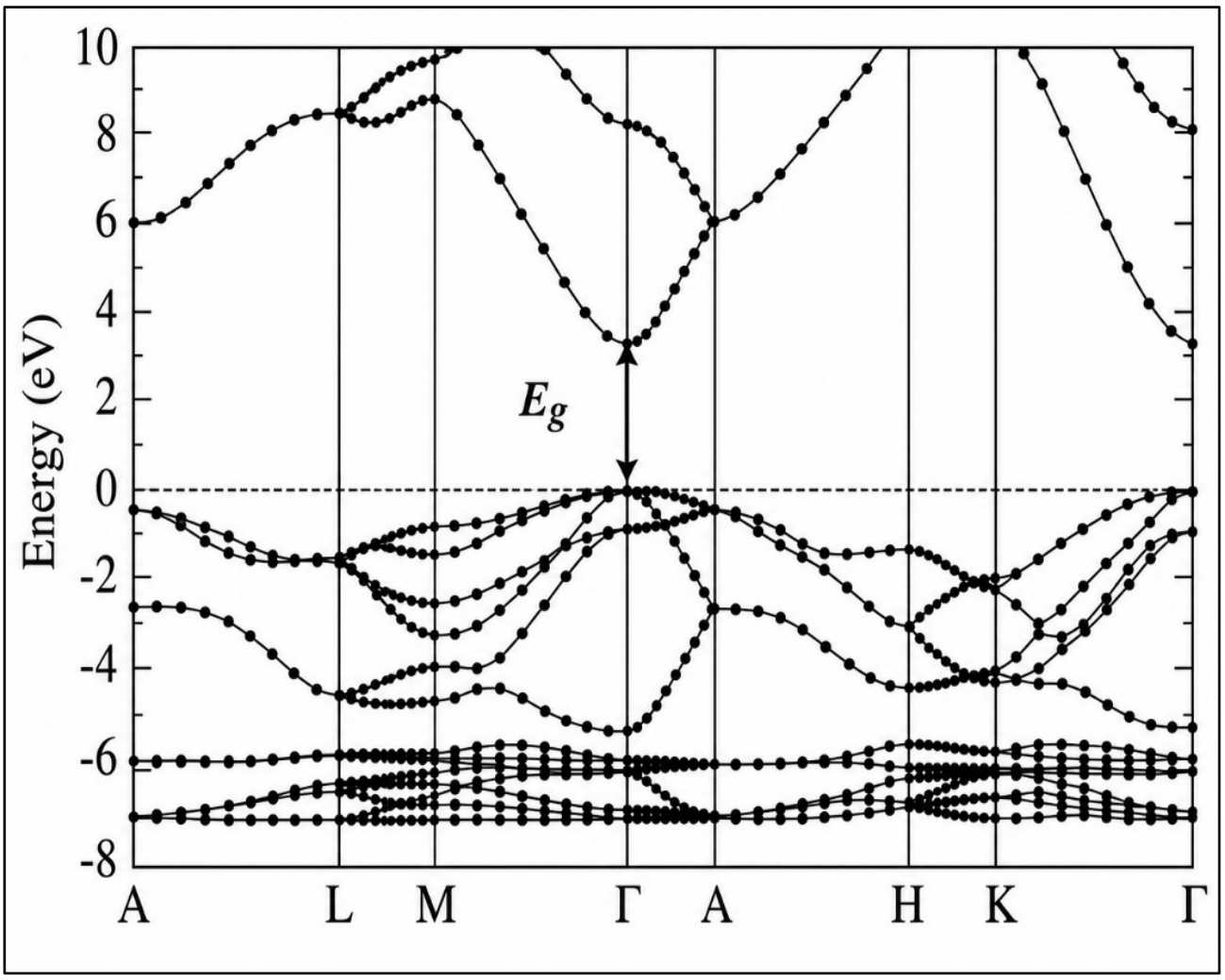


Figure I.6: Band structures of wurtzite ZnO [17].

I.4.1.3 Chemical and catalytic properties

The capacity of a substance to function as a catalyst in a particular system is contingent upon its chemical composition and surface characteristics. The efficacy of zinc oxide is contingent upon its production process. The phenomenon is fundamentally attributed to the perfection of the crystalline lattice and the semiconductor characteristics, including vacancies and interstitial atoms.

Zinc oxide functions as a chemical trap and gas detector for H_2S, CO_2, H_2, and CH_4 [18]. When immersed in water, it can function as a photochemical catalyst for many reactions, including the oxidation of oxygen to ozone, the oxidation of ammonia to nitrate, the reduction of methylene blue, the creation of hydrogen peroxide, and the oxidation of phenols. Recent research is investigating novel forms of ZnO for applications in catalysis and sensing, exhibiting favorable chemical characteristics.

I.4.1.4 Main properties of defects in ZnO

A. Native defects

Defects like **oxygen vacancies** exhibit low formation enthalpies in p-type ZnO and are thus anticipated to occur easily. Thirty Although they may serve as compensatory centers, oxygen vacancies and other native point defects are improbable to be the primary cause of unintended n-type conductivity in ZnO. The oxygen vacancy serves as a profound donor, whereas **zinc interstitials** exhibit instability at ambient temperature. **Zn vacancies** function as compensating acceptors in n-type ZnO. Additional intrinsic defects, including Zn antisites, O antisites, and O interstitials, have elevated formation energies. Under typical conditions, they are likely not found in significant concentrations, although oxygen interstitials may play a crucial role in oxygen self-diffusion.

Intrinsic defects influence the efficacy of Ohmic and Schottky connections. Depth-resolved cathodoluminescence (CL) demonstrated the emergence of point defects at metal-ZnO interfaces, resulting in alterations to the characteristics of the Schottky barriers. The deposition of metals resulted in the creation of point defects with CL energies approximately at 2.1, 2.5, and 3 eV. Processing conditions are critical; for instance, the creation of an AuZn eutectic at 625 °C may induce Zn deficit in the neighboring ZnO material [19].

B. Extended defects

Extended defects in ZnO, such as stacking faults, dislocations, and grain boundaries, represent intricate structural imperfections essential for modulating its optoelectronic characteristics. These defects frequently arise from interactions among point defects (vacancies, interstitials) during processing (ion implantation, annealing) and act as sinks for mobile defects, thereby influencing conductivity, luminescence, and radiation resilience in devices such as UV detectors and solar cells [20].

I.4.2 Applications of ZnO

Owing to the characteristics of ZnO nanostructure previously discussed, zinc oxide (ZnO) is extensively utilized in society and serves as a crucial element in various industrial manufacturing processes, including paints, cosmetics, pharmaceuticals, plastics, batteries, electrical equipment, rubber, textiles, and floor coverings. ZnO has been utilized in acoustic wave devices, gas sensors, solar cells, piezoelectric transducers, light-emitting diodes (LEDs), laser diodes (LDs), and transparent electrodes [21], [22], [23].

Zinc oxide has been utilized in numerous technical applications (Figure I.7), including porcelain enamels, heat-resistant glass, vulcanization activators, additives for rubber and plastics,

pigments in paints with UV-protective and fungistatic properties, protective coatings for spacecraft, components of cigarette filters, healing ointments, and optical waveguides.

Finally, it is worthy to note that ZnO has been also used in medical applications such as sunburn prevention, nappy rash, skin irritations, cold sores, cuts and burns treatments [24].

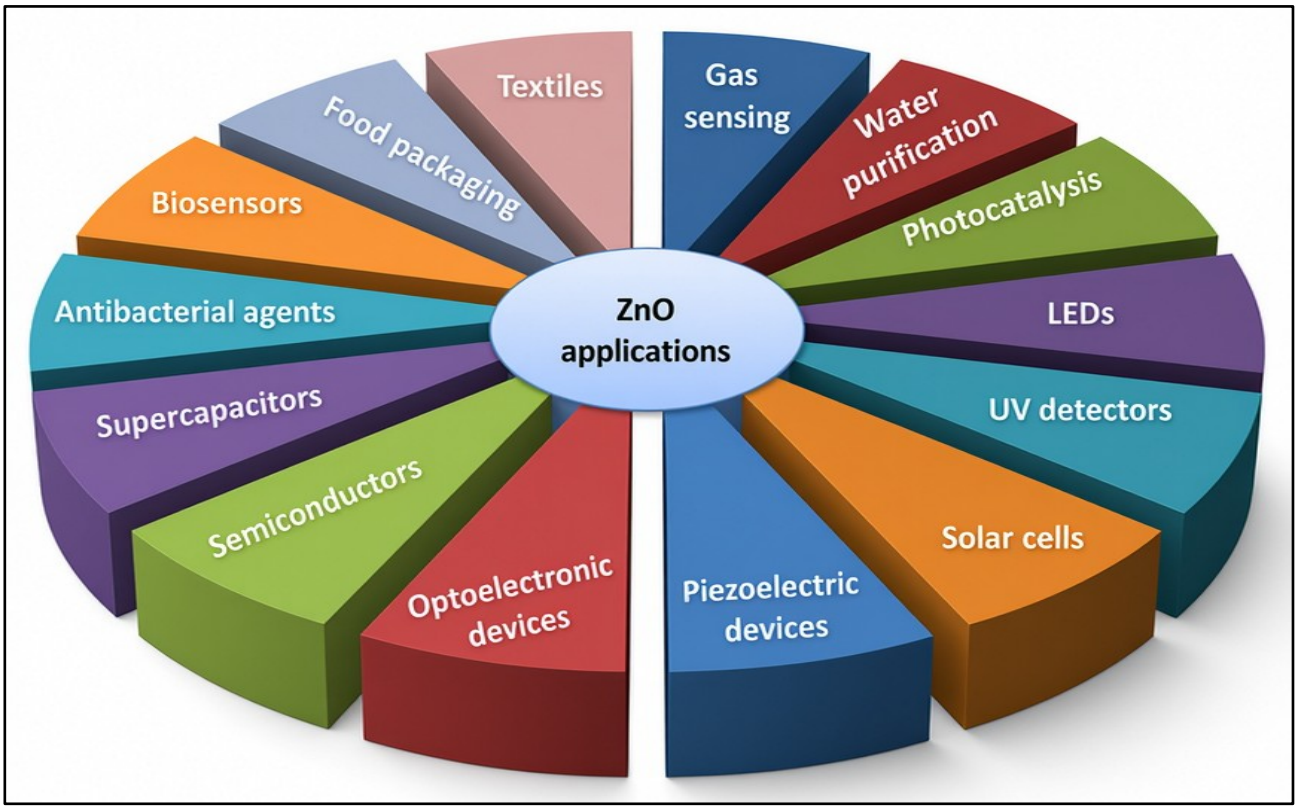


Figure I.7: Applications of ZnO in different fields.

I.5 Photocatalytic oxidation process

The significant prevalence of organic dyes in industrial effluent from sectors such as textiles, paper, and garment manufacture contributes to environmental pollution. The dye effluents contain highly toxic and carcinogenic substances that may present significant health hazards to humans; these dyes are exceedingly detrimental to aquatic habitats. Consequently, the elimination of organic dyes from wastewater is important.

Traditional water treatment techniques frequently fail to adequately eliminate such contaminants, as their degradation may produce hazardous byproducts. This challenge highlights the imperative for Advanced Oxidation Processes (AOPs), which provide a comprehensive solution by ensuring total mineralization of pollutants, thus obviating the requirement for further post-treatment and averting the generation of secondary waste. Photocatalysis has garnered significant attention among advanced oxidation processes (AOPs)

for its effectiveness in converting organic contaminants into harmless compounds under light exposure. Photocatalysis distinguishes itself from other Advanced Oxidation Processes (AOPs) by virtue of its minimal energy demands, capacity to function under sun illumination, catalyst reusability, and more temperate reaction conditions [25].

In 1972, Fujishima and Honda conducted innovative studies that provided the first report on the photoelectrochemical degradation of water. Two electrodes were employed, one composed of platinum and the other of TiO_2, to effectively generate H_2 and O_2 [26]. In 1979, Bard enhanced the electrochemical concept established by Fujishima and Honda by introducing an innovative method for photoelectrochemistry with TiO_2 and platinum cells [27]. This method illustrated that the photoelectrochemical processes of semiconductors can produce powdered systems or particles, which promote non-homogeneous photoreactions. This method illustrated that the photoelectrochemical process of semiconductors can produce powdered systems or particles, which promote non-homogeneous photoreactions.

Zinc oxide (ZnO) is a semiconductor material extensively utilized as a photocatalyst, owing to its properties such as water insolubility, stability in acidic or alkaline conditions, strong corrosion resistance, non-toxicity, abundance, and low cost [28], [29]. The utilization of ZnO in powder or slurry form for wastewater treatment presents challenges in the separation process; hence, the development of ZnO materials immobilized on a support surface was undertaken to address this issue [30]. ZnO, when utilized as thin layers or thin films, represents a notable way of ZnO immobilization that attracts significant interest due to its potential to enhance material and time efficiency in photocatalytic applications compared to ZnO in powder or slurry form [31]. Another disadvantage of ZnO, aside from the separation issue, relates to its properties. The photocatalytic efficacy of ZnO is constrained for practical applications due to its broad band gap energy, elevated recombination rate of photogenerated charge carriers, and inadequate adsorption capacity for visible light. Consequently, the modification of ZnO using various approaches is essential to improve its photocatalytic efficacy, for example, coupling with other semiconductor materials, surface modification with inorganic acids, and metal or non-metal doping [31], [32].

I.5.1 Advantages and disadvantages of ZnO thin film photocatalyst

Thin films exhibit numerous advantages over powder photocatalysts, notably the simplicity of recycling or recovering photocatalysts at the end of the wastewater treatment process (Figure I.8). This may reduce the duration of the process and improve the usage of the photocatalyst, hence minimizing consumption costs. Furthermore, powder photocatalysts suspended in

solution are susceptible to aggregation as concentration increases, hence diminishing photocatalytic efficacy by modifying the optical characteristics that influence light absorption of the photocatalysts [33]. Thin films composed of two-dimensional materials facilitate quantum confinement. The integration of bound and free dimensions facilitates a synergistic enhancement of material characteristics in both bulk and nanoscale forms [34].

The disadvantage of synthesizing photocatalysts as thin films is the difficulty in producing stable thin films, together with limitations in the characterisation procedure. Moreover, in comparison to powdered ZnO, the surface area of thin films is generally more limited, potentially diminishing photocatalytic efficacy. Consequently, the synthesis and modification processes of ZnO as a thin film photocatalyst material must be advanced to address these issues [35].

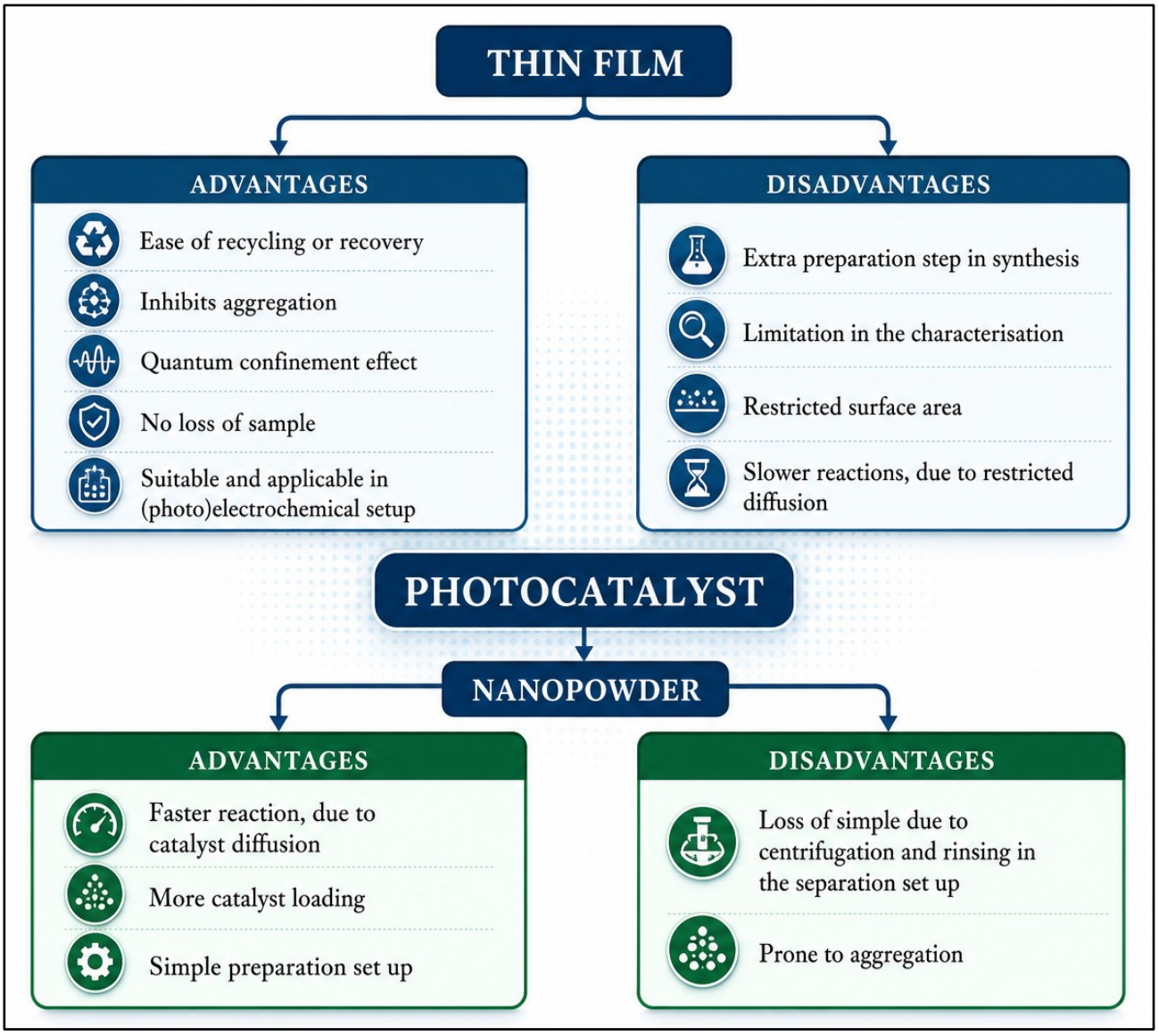


Figure I.8: Advantages and disadvantages of different forms of photocatalyst [34].

I.5.2 General photocatalytic mechanism of ZnO thin film

The mechanism of the ZnO thin film photocatalyst is predicated on its properties as a semiconductor, which features an energy band consisting of a valence band (VB), a conduction band (CB), and a band gap. Electrons in the VB undergo excitation to the CB and produce holes when exposed to light radiation with energy greater than the band gap energy. Electrons (e^-) in the CB will be involved in the reduction process, whereas holes (h^+) in the VB facilitate the oxidation process. The photoexcitation process will result in redox reactions of O_2 and H_2O from the environment, resulting in the formation of superoxide ($\bullet O_2^-$) and hydroxyl radicals ($\bullet OH$). These radical species will contribute to the degradation of pollutants [26]. The mechanism of ZnO photocatalysis is depicted in Figure I.9.

The ZnO photodegradation reaction specifically entails the mechanisms of charge carrier generation, carrier trapping, recombination, and interfacial reactions as illustrated in the following equations.

Carrier generation:

$$ZnO + hv \rightarrow e_{CB}^- + h_{VB}^+ \quad (I.1)$$

Charge carriers trapping:

$$h_{VB}^+ + Zn^{IV}OH \rightarrow \{Zn^{IV}\bullet OH\}^+ \quad (I.2)$$

$$e_{CB}^- + Zn^{IV}OH \rightarrow \{Zn^{III}OH\} \quad (I.3)$$

$$e_{CB}^- + Zn^{IV} \rightarrow \{Zn^{III}\} \quad (I.4)$$

Recombination:

$$e_{CB}^- + \{Zn^{IV}\bullet OH\}^+ \rightarrow \{Zn^{IV}OH\} \quad (I.5)$$

$$h_{VB}^+ + \{Zn^{III}OH\} \rightarrow Zn^{IV}OH \quad (I.6)$$

Interfacial reactions:

$$\{Zn^{IV}\bullet OH\}^+ + \text{pollutant} \rightarrow Zn^{IV}OH + \text{oxidized pollutant} \quad (I.7)$$

$$\{Zn^{III}OH\} + O_2 \rightarrow Zn^{IV}OH + \bullet O_2^- \quad (I.8)$$

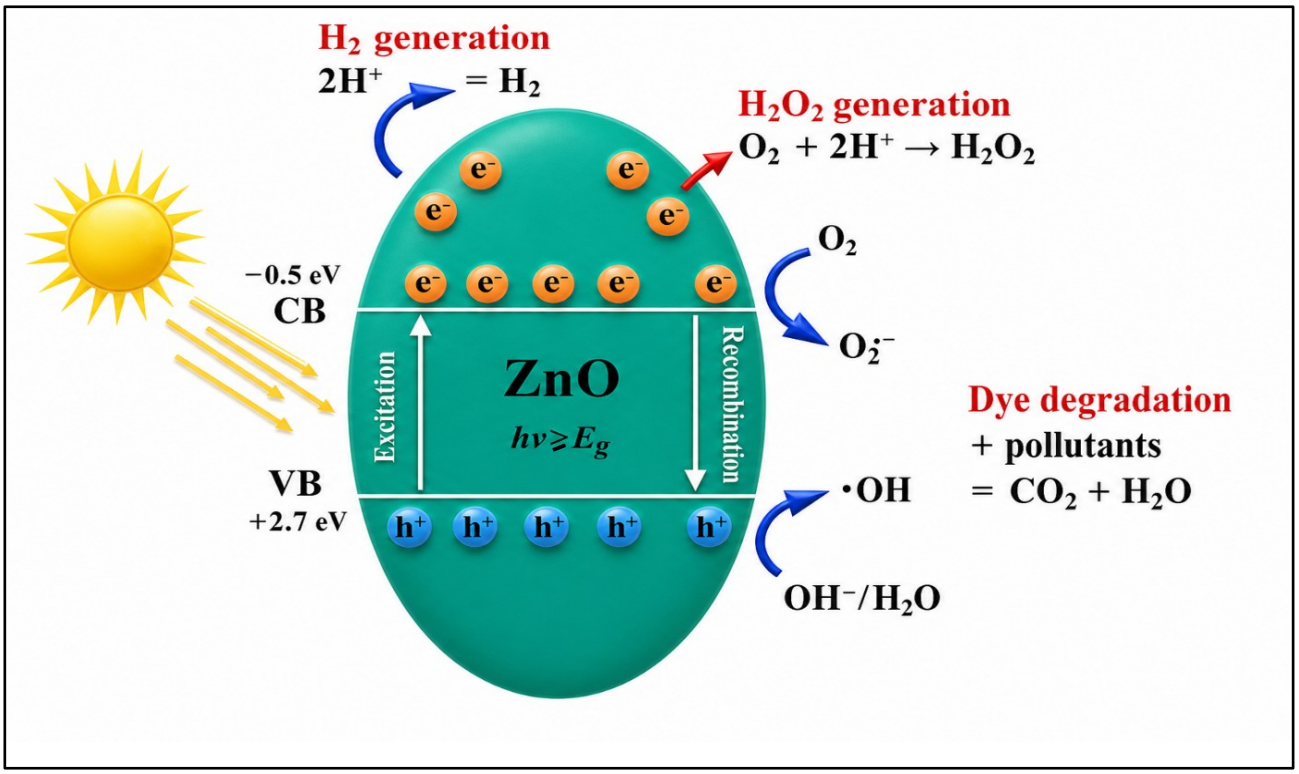


Figure I.9: General photocatalytic degradation mechanism of ZnO [36].

I.5.3 Kinetics of photocatalytic reactions

Generally, the photocatalytic degradation of contaminants by metal oxides is often assessed using spectrophotometers. The photocatalyst was placed into the pollutant solution and the mixture was thereafter agitated immediately. Following the preparation of the mixture, it is allowed to stand for a certain duration to determine the adsorption capacity of metal oxides. Next, the mixture is agitated under UV-visible light or direct sunlight, and the sample is analyzed after a certain interval. Throughout this performance, the λmax value of pollutants consistently diminishes, signifying a reduction in pollutant concentration within the mixture as a result of the degrading response. The reduction in the λmax value is employed to assess the kinetics of this degrading reaction. The kinetics dictate the rate of the degradation reaction, which is the optimal method for assessing the efficacy of a photocatalyst.

I.5.3.1 Pseudo first order

The equations numbered I.9 to I.29 are employed to derive the final equation applicable to the kinetics of photocatalytic degradation reactions. This derived equation refers to pseudo first-order reactions.

Rate of photocatalytic degradation reaction∝ [Concentration].

$$-\frac{dC_t}{dt} \propto C_t \quad \text{(I.9)}$$

$$-\frac{dC_t}{dt} = K_t C_t \quad \text{(I.10)}$$

Rearranging of eq (I.11) gives

$$-\frac{dC_t}{C_t} = K_1\, dt \quad \text{(I.11)}$$

Integrating both sides of eq (I.12) as

$$-\int \frac{dC_t}{C_t} = K_1 \int dt \quad \text{(I.12)}$$

$$-\ln C_t = K_t + C \quad \text{(I.13)}$$

Initial reaction condition (t = 0 and Ct = Co) was applied to find C value than eq (I.14) becomes as

$$-\ln C_0 = C \quad \text{(I.14)}$$

Putting eq (I.14) in eq (I.13) then eq (I.15) becomes

$$-\ln C_0 = K_1 t + (-\ln C_0) \quad \text{(I.15)}$$

$$-\ln C_0 = K_1 t - \ln C_0 \quad \text{(I.16)}$$

Rearrange eq (I.16) as

$$\ln C_0 - \ln C_0 = K_1 t \quad \text{(I.17)}$$

$$\ln \frac{C_0}{C_t} = K_1 t \quad \text{(I.18)}$$

$$\ln \frac{C_t}{C_0} = K_1 t \quad \text{(I.19)}$$

Here, Co denotes the initial concentration of pollutants, Ct represents the pollutant concentration at time t, t signifies the reaction period, and k1 is the rate constant for pseudo first-order degradation reactions, referred to as the apparent rate constant (k1app). Equation (I.19) can also be articulated in terms of absorbance (A) utilizing the Beer-Lambert law as follows:

$$\ln \frac{A_t}{A_0} = -K_1 t \quad \text{(I.20)}$$

This equation indicates that a graph is constructed plotting the natural logarithm of the ratio of the absorbance value at any given time to the initial absorbance against the degradation reaction time. The slope derived from this graph signifies the k1app value of these pseudo first-order degradation reactions.

I.5.3.2 Pseudo second order

To derive the equation utilized for pseudo second-order reactions, one must follow each step from equation (I.21) to equation (I.29).

Rate of photocatalytic degradation∝[Concentration]^2

$$-\frac{dC_t}{dt} \propto C_t^2 \quad \text{(I.21)}$$

$$-\frac{dC_t}{dt} = K_2 C_t^2 \quad \text{(I.22)}$$

Rearrange eq (I.22) as

$$-\frac{dC_t}{C_t^2} = K_2 dt \quad \text{(I.23)}$$

Integrating both sides of eq (I.23) as

$$-\int \frac{dC_t}{C_t^2} = K_2 \int dt \quad \text{(I.24)}$$

$$\frac{1}{C_t} = K_2 t + C \quad \text{(I.25)}$$

The initial reaction condition (t = 0 and Ct = Co) was utilized to determine the C value, leading to the transformation of equation (I.25) as follows:

$$\frac{1}{C_0} = C \quad \text{(I.26)}$$

Substituting equation (I.26) into equation (I.25) transforms equation (I.25) into

$$\frac{1}{C_t} = K_2 t + \frac{1}{C_0} \quad \text{(I.27)}$$

$$\frac{1}{C_t} - \frac{1}{C_0} = K_2 t \quad \text{(I.28)}$$

In this context, k_2 denotes the rate constant of pseudo-order degradation reactions, referred to as the apparent rate constant (k_{2app}) for second-order reactions. Equation (I.28) can alternatively be expressed in terms of absorbance (A) utilizing the Beer-Lambert rule, as follows:

$$\frac{1}{A_t} - \frac{1}{A_0} = K_2 t \quad \text{(I.29)}$$

I.5.4 Factors affecting photocatalytic efficiency

The catalytic activity of various metal oxides differs markedly, and this variation is a crucial element of heterogeneous catalysis, although it remains inadequately comprehended in numerous practical applications. Despite extensive application in environmental cleanup, energy conversion, and chemical synthesis, a comprehensive knowledge of how these intrinsic features influence catalytic performance continues to pose a difficulty. The absence of clarity constrains the logical design and selection of catalysts for certain industrial or environmental processes.

Numerous factors affect the catalytic efficacy of metal oxides, including particle size, morphology, surface area, bandgap energy, and defect chemistry.

A. Effect of surface area

The surface area of metal oxide photocatalysts is a crucial factor affecting photocatalytic performance, as it directly determines the number of active sites accessible to light-induced redox reactions. An expanded surface area improves the adsorption of reactant molecules, hence facilitating charge transfer at the catalyst-reactant interface and rising the density of surface hydroxyl groups important to the generation of reactive oxygen species (ROS). Consequently, optimizing surface area is an effective approach to enhance photocatalytic performance without modifying the bulk electrical structure [37]. Nonetheless, surface area alone is inadequate to ensure activity; it must be tuned alongside characteristics like as crystallinity, pore shape, and charge carrier mobility. Excessively elevated surface areas may result in amorphous phases or surface defects that function as charge recombination sites, undermining the advantages of photocatalysis. Degradation efficiency of pollutants increases with increasing the surface area of metal oxides as given in Figure I.10.

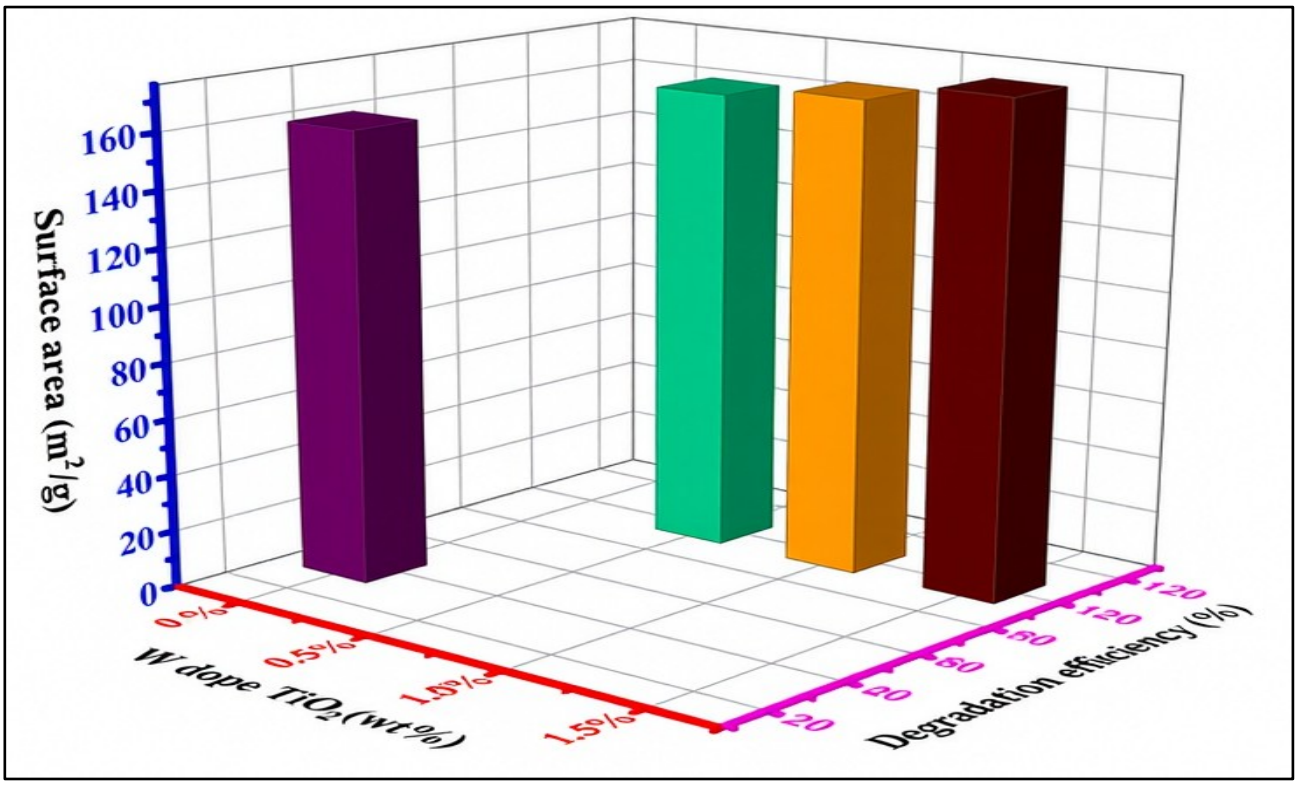


Figure I.10: Degradation efficiency and surface area of (0–1.5%) W-doped TiO2 in the presence of xylene under the following conditions: light intensity = 132.6 W/m², [xylene] = 0.05 mL, flow rate = 300 mL/min [38].

B. Effect of band gap

Band gap engineering is a crucial strategy for improving the catalytic efficiency of metal oxide photocatalysts by adjusting their light absorption characteristics and charge carrier dynamics. The band gap energy (Eg) represents the minimal photon energy necessary to promote an electron from the valence band (VB) to the conduction band (CB), therefore initiating photocatalytic processes. Generally, a narrower bandgap often allows for the absorption of a greater portion of the solar spectrum (i.e., visible light); nevertheless, this is frequently linked with an increased rate of electron-hole recombination and reduced oxidative ability of photogenerated protons [39]. Conversely, a large band gaps provide more energetic charge carriers with elevated redox potentials; nonetheless, activation is predominantly confined to the ultraviolet spectrum of sunlight (about 3–5%). TiO_2 (3.2 eV) and ZnO (3.2 eV) are broad-band gap photocatalysts that exclusively absorb UV irradiation ($\lambda < 400$ nm) and demonstrate exceptional photocatalytic activity under UV light, although possess restricted responsiveness to visible light [40]. This limits their activation to UV light, which constitutes only a minor portion (about 5%) of the solar spectrum, hence limiting their effectiveness in natural sunlight [39].

To address this limitation, band gap strategies have been utilized to reduce the band gap or adjust its position to improve visible light absorption and promote redox processes. Methods comprise non-metal (e.g., N, C, S) and metal (e.g., Fe, Co, Cu) doping, coupling with narrow-bandgap semiconductors that generate oxygen vacancies, and the formation of heterojunctions. These adjustments not only redirect the optical response to the visible spectrum but also affect charge carrier recombination rates and redox potential alignment. Upon light energy absorption by a photocatalyst, electrons are excited to the conduction band, resulting in the formation of holes in the valence band. If the conduction band potential is more negative than the $O_2/O_2^{\bullet-}$ redox potential (−0.13 V vs. NHE), these electrons may decrease oxygen to generate $O_2^{\bullet-}$, thereby enhancing pollutant degradation and inhibiting electron-hole recombination (depicted in Figure I.11). [41].

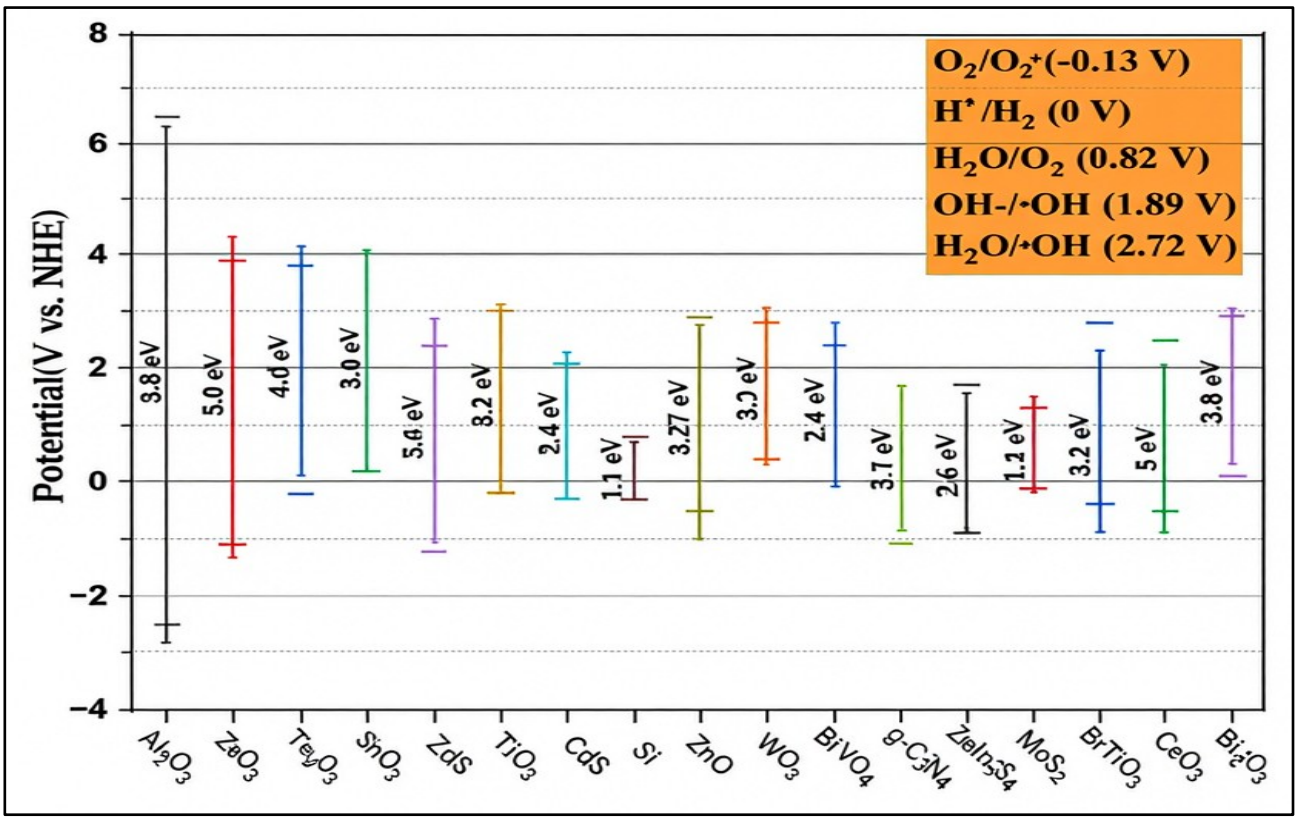


Figure I.11: Effect of band gap on photocatalytic performance [41].

C. Doping with metallic or non-metallic ions

The incorporation of metal or non-metal ions as impurities into the photocatalyst structure diminishes its energy bandgap, hence decreasing the energy necessary to excite the photocatalyst's energy bandgap [42]. In this situation, electron-hole pairs can be produced utilizing visible light. Given that a significant fraction of sunlight comprises the visible light spectrum, photocatalysts will demonstrate photocatalytic activity when exposed to sufficient and readily accessible sunlight [43]. This benefit possesses considerable economic and ecological significance. Non-metallic ions that can be incorporated into the structure of photocatalysts include sulfur, nitrogen, carbon, boron, among others. When selecting the dopant type, one must examine the crystalline structure and morphology of the photocatalyst, its energy bandgap, as well as its structural and chemical constituents. The oxidation states of dopants are crucial for the formation and separation of electron holes, hence enhancing the transfer characteristics of electrons, oxygen ions, and holes at the surface as illustrated in Figure I.12 [44].

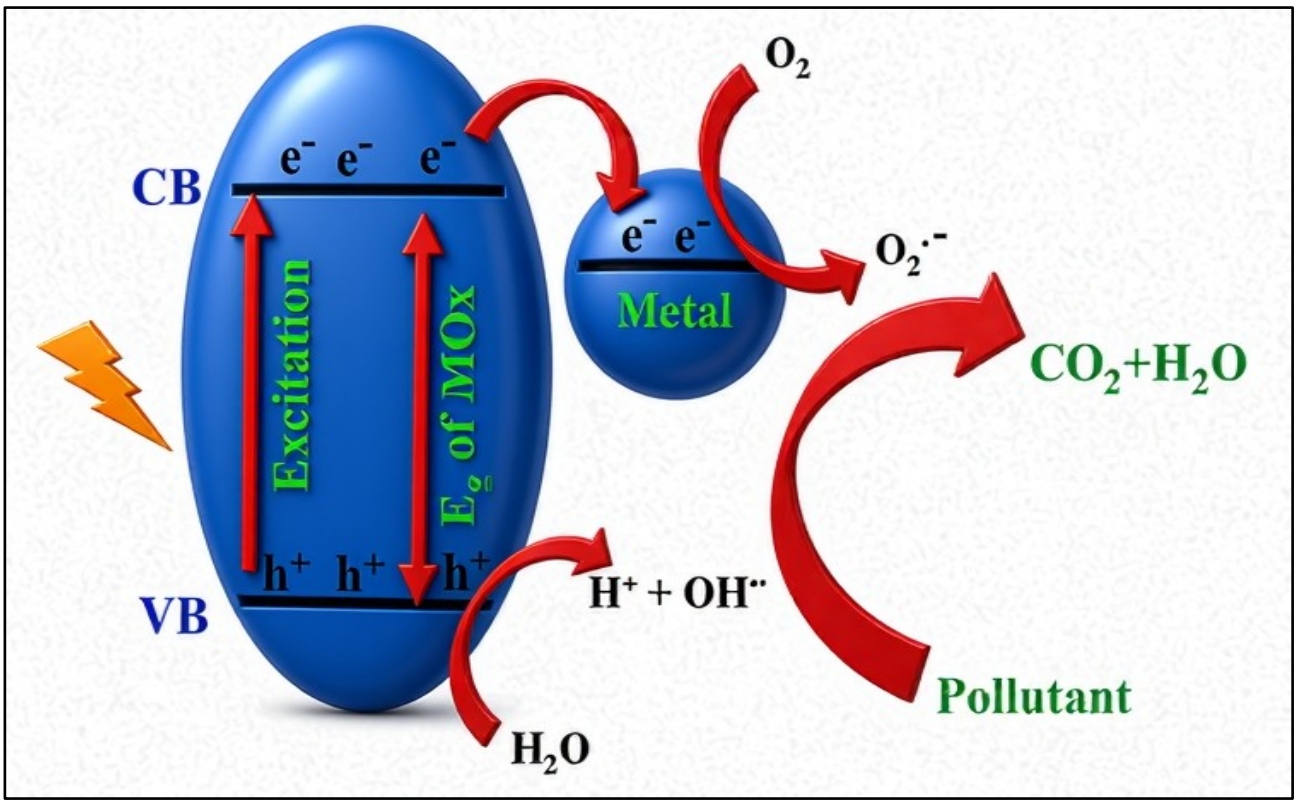


Figure I.12: The mechanism of metal doping on metal oxide semiconductor for enhanced photocatalytic activity [45].

D. Intensity of light

Light intensity represents a key external factor affecting the photocatalytic activity of metal oxides. Because photocatalysis depends on the generation of electron-hole pairs through photon absorption, higher light intensity generally increases the production of charge carriers. The increased carrier density can enhance the frequency of surface redox reactions, hence accelerate pollutant degradation or improve the efficacy of photocatalytic water splitting. The correlation between light intensity and catalytic performance is non-linear and influenced by intricate interfacial and kinetic processes that are insufficiently investigated. The intensity of light is a crucial external factor affecting the photocatalytic activity of metal oxides [46], [47]

At low light intensities, the rate of charge carrier production frequently constitutes the limiting factor, and photocatalytic efficiency escalates almost linearly with light intensity. Conversely, at elevated intensities, a saturation threshold may arise due to recombination phenomena, restricted active sites, or mass transfer constraints. Moreover, high photon intensity may induce adverse thermal effects, potentially modifying reaction pathways or damaging catalyst structures [45].

E. Scavengers agents

Scavengers are utilized as diagnostic tools in mechanistic investigations, rather than as ways to improve efficiency. These specialized compounds, added in controlled proportions, are designed to selectively capture photogenerated species such electrons (e^-), holes (h^+), hydroxyl radicals (•OH), and superoxide radicals ($O_2^{\bullet-}$). This helps to identify which reactive species are most vital in the photocatalytic process. For example, isopropanol is often used to remove hydroxyl radicals, whereas benzoquinone is used to remove superoxide radicals. In addition, EDTA or TEOA can be used to remove holes. By observing alterations in photocatalytic activity following the introduction of each scavenger, investigators can deduce the primary contributor to degradation: •OH, $O_2^{\bullet-}$, or h^+. Scavengers function as analytical tools; their purpose is not to enhance photocatalytic efficiency but to elucidate the underlying mechanism [48].

Scavengers serve two primary functions in photocatalysis. Firstly, they function as indicators in mechanistic investigations to determine the active species responsible for pollutant degradation. Secondly, and more critically for catalytic enhancement, they selectively hold either electrons or holes, thereby decreasing the recombination rate and prolonging the lifetime of charge carriers [49], [50]. For example, the usage of electron scavengers such as silver nitrate ($AgNO_3$) or potassium dichromate ($K_2Cr_2O_7$) can capture photogenerated electrons, hence facilitating the more efficient involvement of holes in oxidative reactions. Conversely, hole scavengers like methanol or EDTA can enhance reduction reactions by consuming holes and facilitating electron predominance.

Besides controlling the photocatalyst's structure and addressing issues related to the overall process, factors such as temperature and pH also affect light absorption, electron-hole recombination rates, and other photocatalytic characteristics [51].

I.5.5 Photocatalyst deactivation

The deactivation of photocatalysts is a significant concern. Extended use of photocatalysts usually ends in a decline in their activity due to many degradation mechanisms. A critical element is surface poisoning due to reaction intermediates or residual species: partially oxidized molecules and other byproducts tend to adsorb deeply onto active sites, hindering the adsorption of reactants and diminishing overall photocatalytic effectiveness [52]. Furthermore, numerous catalysts exhibit photo-corrosion or self-oxidation/reduction when exposed to light. For

example, ZnO photocatalysts easily deteriorated in water, releasing Zn^{2+} into the solution and resulting in a corresponding decline in activity [53].

I.6 UV photodetection application

A photodetector is an electric device that converts visible, infrared, or ultraviolet light into electrical signals. These devices have been widely developed recently because they are essential for a variety of applications, including astronomy, space exploration, medicine, secure communications, and environmental monitoring [54].

I.6.1 Fundamentals of photodetectors

The electrical characteristics of photodetectors, such as resistance, voltage, and current, change when exposed to light. The photodetector device consists of the two main parts are photosensor material and metal electrodes. A variety of device mechanisms, including the photoconductive effect, photovoltaic effect, bolometric effect, photo-thermoelectric effect, photogating effect, and pyro-phototronic effect, can be selected based on the junction formed between the photosensor material and metal electrode and the device's structure [55].

In general, the absorption of photons with energies higher than or equal to the photosensor's (semiconductor) bandgap excites negatively charged electrons from the valence band into the conduction band, which allows electrons to move across the crystal lattice over great distances when subjected to an internal or external electric field. Additionally, when an electric field is applied, positively charged holes in the valence band move from one atomic site to another, aiding in electrical conduction. In this way, light absorption separates electron-hole pairs, creating a photocurrent that is gathered at the semiconductor edges by the metal electrodes. The photocurrent's intensity at a particular wavelength rises as the intensity of the incident light increases. By converting the energy of the absorbed photons into a measurable form, it may also be used to determine the photon flux (also known as optical power) of a light beam. Furthermore, the following features are crucial for evaluating the performance of the photodetector device: photoresponsivity, photocurrent, specific detectivity and external quantum efficiency, all of which are covered in detail in the next section.

I.6.2 Classification of UV photodetectors

In general, there are three types of semiconductor-based photodetectors: photoconductors, photodiodes, and phototransistors.

a. Photoconductors

When exposed to light, the photoconductor's charge carrier number changes, allowing it to detect light. To collect the photoexcited electron-hole (e-h) pairs, two metal ohmic contacts are

formed on opposite ends of the photoconductor. as shown in Figure 13(a). The photogenerated e-h pairs are collected at the electrodes by an external bias. Similar to a photosensitive resistor, a photoconductor's resistance changes in response to light. Photogenerated charge carriers move by the external circuit before recombination [56].

b. Photodiodes

The components of a photodiode are a semiconductor junction (p-n, p-i-n) or a metal/semiconductor junction. The internal-electric field generated at the junction's interface causes photoexcited e-h pairs to travel in the opposite direction when a photodiode type photodetector is operated under reverse bias [56]. as shown in Figure. 13(b).

c. Phototransistors

Techniques to improve the photodetector's performance should decrease the noise in the device in addition to raising the detector's gain. In photoconductors, low-resistance or Ohmic connections produce a lot of dark current, which raises the flicker (1/f) or shot noise. On the other hand, high-quality photodiodes functioning in photovoltaic mode can achieve low noise; nevertheless, the absence of gain inhibits their reactivity. The concept of phototransistors has been developed to address the noise problem. The gate terminal of a phototransistor is electrically insulated from the channel by a dielectric layer, making it comparable to a photoconductor, as seen in Figure I.13 (a-c). The gate voltage can be used to adjust the channel's charge density and dark current. As a result, high photoconductive gain and low noise could be achieved, leading to high responsivity and a gain-bandwidth product [56].

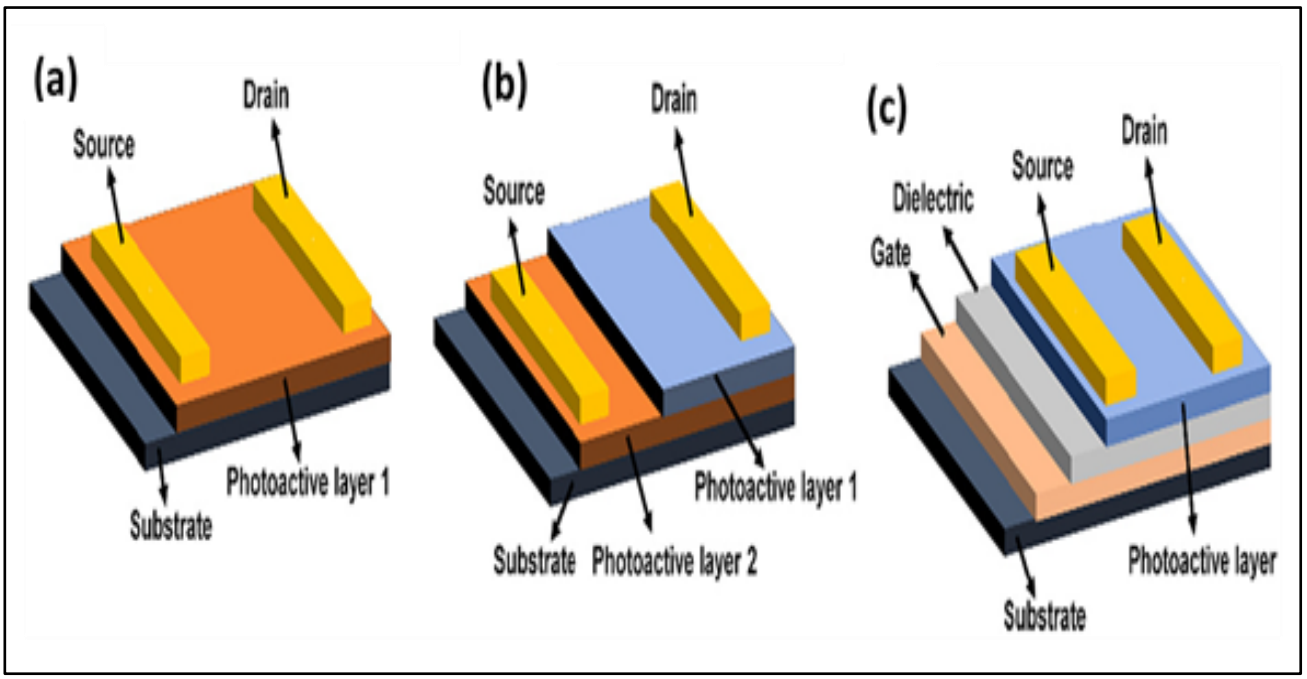


Figure I.13: Diagrammatic illustration of the different types of photodetectors a) phototransistor b) photoconductor c) photodiode [56].

I.6.3 Performance parameters of photodetectors

The performance of a photodetector must be assessed using a number of critical performance parameters. A photodetector's responsivity (R), response time, photoconductive gain (G), detectivity (D*), external quantum efficiency (EQE), noise equivalent power (NEP), signal to noise (SNR), etc. are typically measured. In this section, a brief introduction about these important performance parameters is given.

- **Responsivity**: The efficiency of a photodetector's photoelectric conversion is indicated by its responsiveness (R). The ratio of photocurrent to the power density of lit light is known as responsiveness. The equation that follows can be used to express responsiveness:

$$R = \frac{I_{ph}}{P_{inc}A_0} \quad (I.30)$$

Where, I_{light} is the output current in the presence of light, I_{dark} is the dark current, P_{in} is the power density of input light, and A is device area.

- **External quantum efficiency (EQE) :**

EQE provides the conversion efficiency of the detector and shows the number of e-h pairs produced per number of photons incident. The following equation is used to calculate EQE:

$$EQE = R\frac{hc}{q} \quad (I.31)$$

where, h, c, and q stand for Planck's constant, light speed, and electron charge respectively.

- **Internal quantum efficiency (IQE) :**

IQE and EQE are comparable, with the exception that IQE takes into account the quantity of photons absorbed. The ratio of created e-h pairs to absorbed photons is known as the IQE. The following formula provides IQE:

$$IQE = R\frac{hc}{qA_{abs}} \quad (I.32)$$

wherein A_{abs} is the ratio of the absorbed to incident light power at a specific wavelength.

- **Response speed :**

Response speed, which includes rising time (τr) and decay time or fall time (τf), indicates how quickly the photodetector reacts to input light when the laser source is turned on and off. The separation, movement, and collection of charge carriers in the channel primarily determine the photodetector's response. The time difference between 10% and 90% and 90% and 10% of the device current is used to calculate the detector's rise and fall times.

- **Photoconductive gain (G) :**

The number of charge carriers passing through the apparatus in relation to the quantity of photons incident is known as the photoconductive gain (G). It is determined using the following formula:

$$G = \frac{\tau_{life}}{\tau_{transit}} = \frac{\tau_{life}}{\tau^2/\mu V_{bias}} \quad (I.33)$$

Where τ_{life} and $\tau_{transit}$ represent the charge carriers' lifetime and transit time, respectively, V_{bias} is the applied bias, μ is the carrier's mobility, and L is the channel-length.

The lifetime of the charge carriers is the primary determinant of photoconductive gain, which rises as carrier life time (τlife) grows. On the other hand, a longer carrier lifespan causes the device's response time to drop, resulting in a trade-off between gain and response time. But in reality, it is impossible to create a photodetector with extremely high responsivity and quick response times.

- **Specific detectivity (D*) :**

The photodetector's sensitivity is indicated by its detectivity. The following is the detectivity equation:

$$D^* = \frac{R}{\sqrt{2qJ_d}} \quad (I.34)$$

Wherein Jd (I_d/A_0) represents dark current density. The unit is cm Hz1/2/W or Jones.

- **I_{on}/I_{off} ratio :**

The sensitivity is the ratio of the device current while illuminated by light to when not illuminated is known as the Ion/Ioff. superior on/off ratio photodetectors have very low dark current and superior light absorption. To detect low-intensity signals in practical applications, photodetectors with a higher on/off ratio are required.

Chapter II Deposition and Characterization Techniques of Thin Films

II.1 Introduction

This chapter provides an overview of the most commonly utilized thin film preparation methods. We ‘ll discuss in more detail the solgel dip caoting technique that we used for the preparation of S-doped ZnO and Cd-doped ZnO films. Additionally, the characterisation techniques employed to analyze the thin films in this investigation will be discussed. The techniques encompass X-ray diffraction (XRD), scanning electron microscopy (SEM), energy dispersive X-ray (EDS), atomic force microscopy (AFM), and UV-visible spectrophotometry for the analysis of structural, morphological, chemical composition, and optical properties, respectively.

II.2 Thin film deposition techniques

Physical processes like physical vapour deposition (PVD) and chemical processes like chemical vapour deposition (CVD) comprise the many thin film deposition techniques **(**Figure.II.1**)**

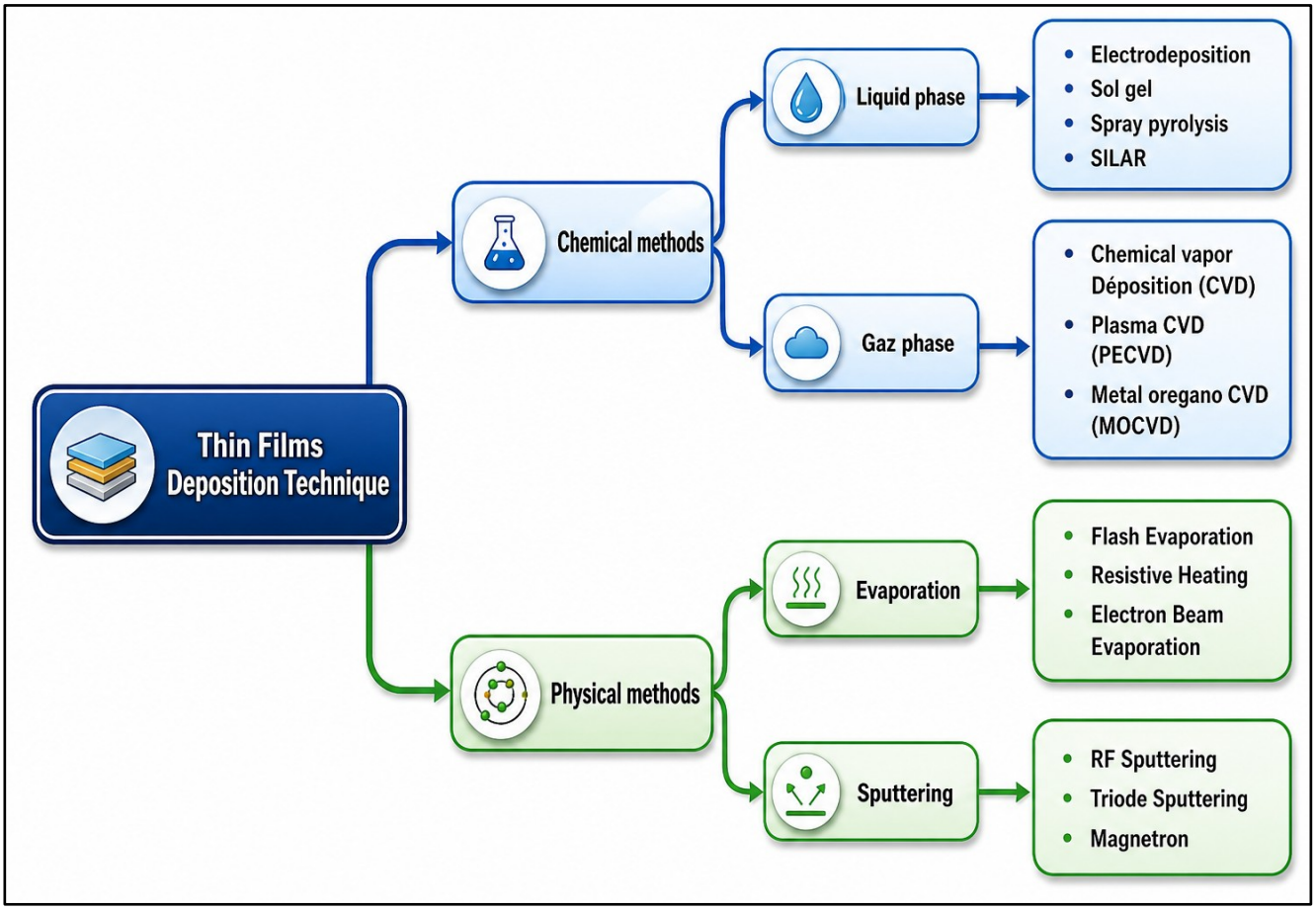


Figure II.1: Thin film deposition technique classification [57].

II.2.1 Sol-gel technique

The sol–gel deposition process encompasses synthesis methods that yield substantial amounts of nanosized materials with precisely regulated particle size, shape, orientation, and crystal structure, along with enhanced physical and chemical properties. This pertains to the production of metal oxide thin films, including chemical reactions, nucleation, growth, and ageing utilising an aqueous thin film processing technique known as aqueous chemical growth. Modulating the thermodynamics and kinetics of nucleation, growth, ageing, and precipitation conditions enables straightforward and effective regulation of particle size and distribution The necessity for minimal surface energy compels nanoparticles to adopt a spherical shape. Nonetheless, under appropriate synthesis (precursors) and dispersion circumstances, the morphology can be influenced by the crystal symmetry and the chemical milieu Numerous process parameters affect the interfacial tensions, which significantly contribute to the outcome. The regulation of the crystal structure is associated with nucleation kinetics [58].

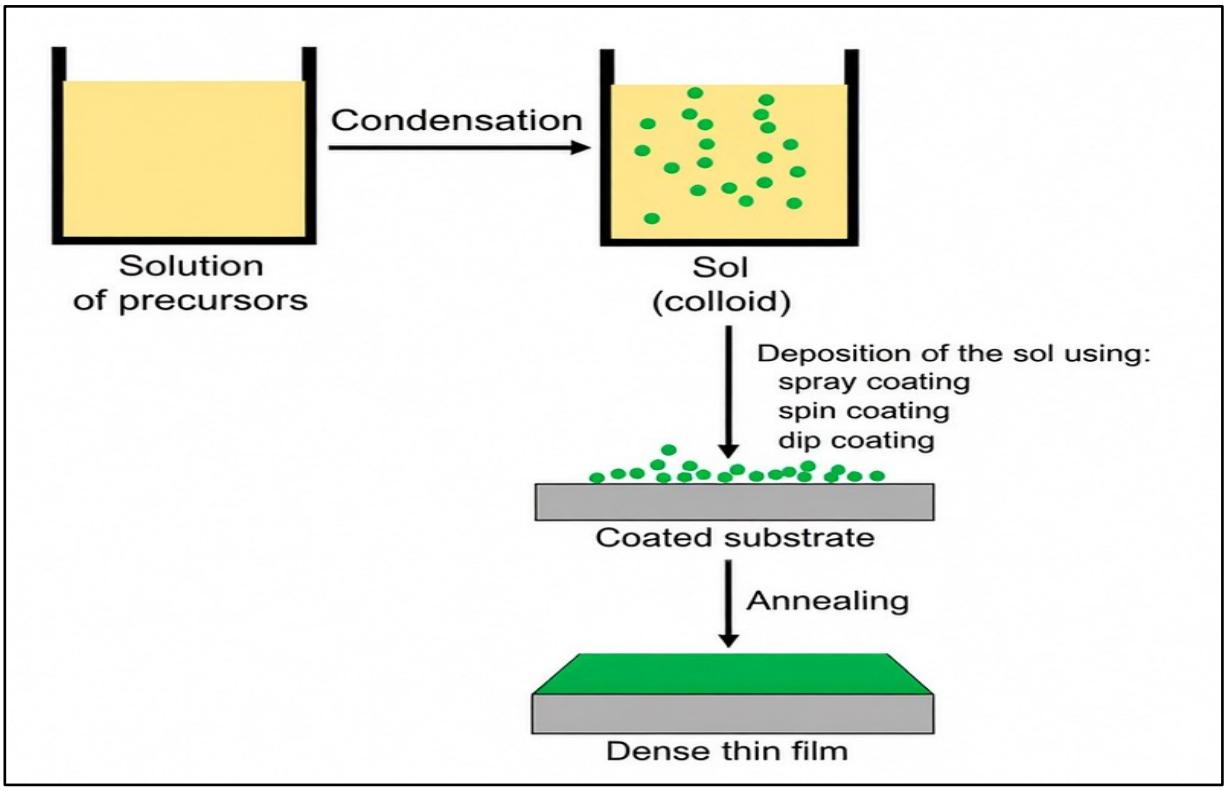


Figure II.2: Thin film deposition using the sol gel method [59].

II.2.2 Dip coating

Dip coating (DC) is a straightforward and efficient technology widely employed across numerous industries, serving as a primary way to fabricate thin films using a specialised dip coater. Under optimum conditions, dip coating may effectively produce extremely uniform films and offers advantages over other coating processes due to its design simplicity, resulting in reduced installation and maintenance costs. Under optimum conditions, dip coating may effectively produce extremely uniform films and offers advantages over other coating processes due to its design simplicity, resulting in reduced installation and maintenance costs. To achieve this, it is important to meticulously control coating parameters and additional elements, including withdrawal speed, temperature, airflow, and cleanliness, throughout the coating process, necessitating profound comprehension and proficient coating expertise [60].

II.2.2.1 Step dip coating process

The step dip coating procedure comprises three technical stages contingent upon the continuity of the operation [61].

Step 1- Substrate immersion in the solution: The substrate is gradually submerged into the solution at a steady and meticulously specified velocity.

Stage 2– dwell time: The substrate transports the precursor solution to be applied at a constant velocity, followed by a designated dwell period, facilitating adequate contact between the substrate and the precursor structures (coating solution).

Stage 3– Deposition and drainage: The substrate is elevated, entraining the precursor solution (film-deposition phase) at a constant velocity toward the deposition area. The internal layer ascends with the substrate, and the external layer descends back into the bath with the current.

Stage 4- Evaporation: The solvent evaporates from the liquid, resulting in the formation of a deposited layer. The evaporation process can be expedited by the application of external heat and the augmentation of surface area. Subsequently, the deposited film undergoes additional thermal treatment, which eliminates remaining organics and promotes the crystallization of functional oxides.

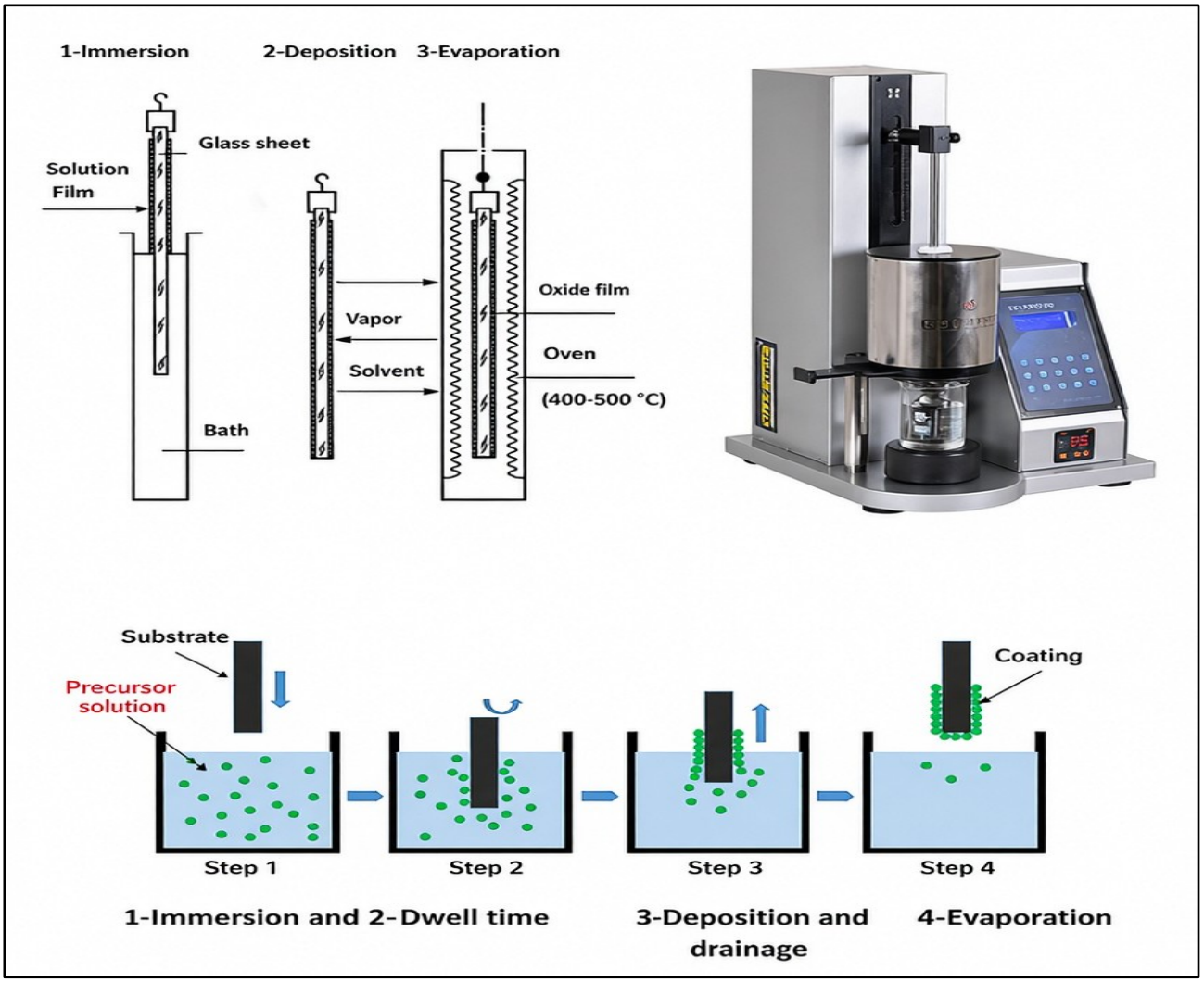


Figure II.3: Dip-coating process levels [59], [62].

II.2.2.2 Thickness of the film in the dip-coating

In the dip-coating procedure, illustrated in Figure 3, when the viscosity of the liquid (η) and the substrate speed (U) are sufficiently elevated to reduce the curvature of the meniscus, the ratio of the thickness of the viscous drag ($\alpha\eta$U/h) to the gravitational force (ρgh) is directly proportional to the thickness of the deposited film (h), as expressed in Eq. (II.1) [61].

$$h = C_1\left(\frac{\eta U}{\rho g}\right)^{\frac{1}{2}} \quad \text{(II.1)}$$

The proportionality constant, c1, is 0.8 for Newtonian fluids in the typical dip-coating method. The substrate velocity and liquid viscosity are significantly reduced in sol-gel manufacturing.

The equilibrium between substrate velocity and liquid viscosity is regulated by the ratio of viscous strain to liquid–vapor surface tension (γL, V), as delineated by the relationship established by Landau and Levich. The hydrodynamic variables of dip coating, which encompass solely pure liquids while disregarding temperature, were identified. This is articulated below in Eqs. (II.2) and (II.3):

$$h = 0.94\,(\frac{\eta U}{\gamma_{L.V}})^{\frac{1}{6}}\,(\frac{\eta U}{\rho g})^{\frac{1}{2}} \tag{II.2}$$

Upon rearranging, we obtain

$$h = 0.94\frac{(\eta U)^{\frac{2}{3}}}{(\rho g)^{\frac{1}{2}}\,(\gamma_{L.V})^{\frac{1}{6}}} \tag{II.3}$$

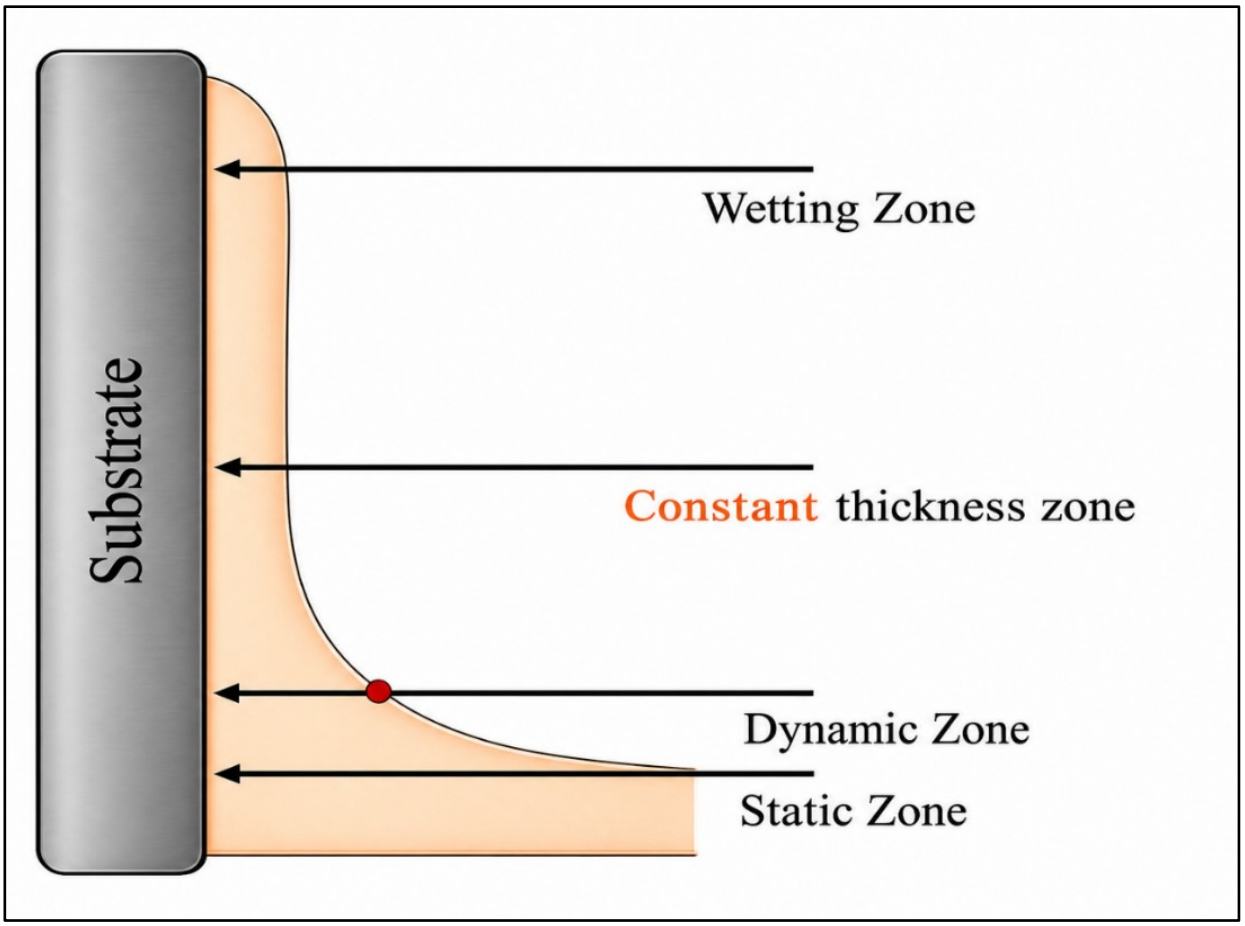


Figure II.4: Areas of dip coating film development [63].

The thickness of the films is determined by the streamline that separates the upward and downward moving layers. Six types of forces influence the film-deposition region, determining the thickness and regularity (streamline) of the deposited film:

1. Viscous drag acting upward on the sol due to the sliding substrate.
2. The gravitational attraction.
3. Inertial force of the boundary layer in the deposition region.
4. Inertial force of surface tension resulting from the concave configuration of the meniscus.
5. Surface tension gradient.
6. The separating or uniting pressure.

II.2.2.3 Control of microstructure

The film microstructure is effectively regulated by the particle size. For unaggregated, mono-sized particulate sols, pore size is inversely related to surface area, resulting in an increase in surface area as pore size diminishes. The determinants influencing the microstructures of the deposited thin films comprise the following:

1. The morphology of the inorganic precursors incorporated in the initial sol (structure, size, and fractal dimension).
2. The reactivity of precursors (condensation and aggregation rates).
3. The duration of the deposition process (evaporation rate and film thickness).
4. The magnitude of shear field applied and the capillary forces accompanying film deposition (surface tension gradients).

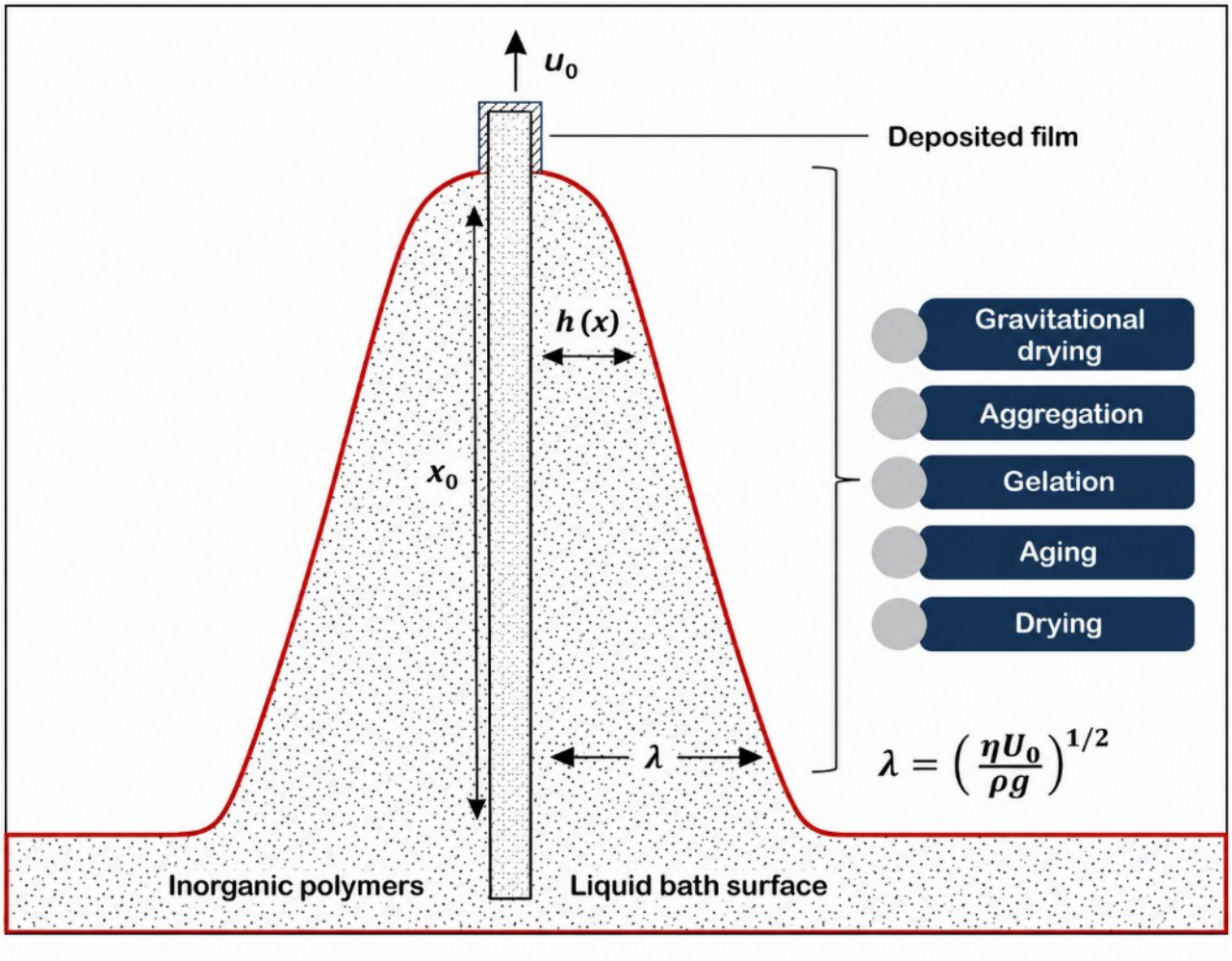


Figure II.5: Schematic depiction of the dip-coating procedure [61].

II.2.2.4 Advantages of dip coating

A. High productivity

Dip coating facilitates batch processing, enabling the simultaneous coating of several workpieces. In contrast to spray or spin coating, which applies coatings individually, it facilitates much accelerated production. Complexly formed workpieces can be efficiently coated by modifying the coating liquid and withdrawal velocity.

B. Cost efficiency

Dip coating methods are comparatively straightforward, minimising upfront capital expenditures. The procedure also reduces material waste, contributing to decreased operational expenses. Its appropriateness for mass production renders it efficient in decreasing the coating cost per unit.

C. Suitability for complex shapes

Dip coating uniformly applies a coating over the whole surface of a workpiece, rendering it effective for intricate geometries. To prevent problems like sagging or inconsistent thickness, it is essential to select the appropriate coating substance and establish a suitable withdrawal speed.

D. Efficiency of simultaneous coating on both sides

Dip coating enables the simultaneous application of a coating to both surfaces of a workpiece in a single immersion. This significantly enhances efficiency relative to techniques necessitating the coating of each side individually.

II.2.2.5 Disadvantages of dip coating

- **Risk of uneven film thickness**

The thickness of the film in dip coating is affected by withdrawal speed, liquid viscosity, and surface tension. If these elements are not adequately regulated, inconsistent coating may ensue. Exact regulation of these parameters is crucial for attaining consistent thickness.

- **Possibility of elevated initial equipment expenses**

Dip coating methods for large-scale production may necessitate substantial capital expenditure. The initial expense may provide a difficulty for small or medium-sized enterprises. Nonetheless, the enduring advantages of enhanced production may surpass the initial expenditures.

- **Significance of the cleaning procedure**

Inadequate cleaning prior to coating might diminish quality and lead to complications in future procedures. Enhancing the cleaning process is essential for attaining dependable coating efficacy.

- **Potential for drooping**

Complexly shaped workpieces are susceptible to sagging during dip coating. To avert this, it is necessary to implement steps such as modifying coating viscosity, improving withdrawal velocity, and enhancing the workpiece design.

II.2.2.6 Various factors influencing dip coating 6

✓ **Substrate surface cleaning:** Confirm the substrate surface is devoid of impurities to enhance adhesion.

✓ **The purity of the coating solution**: Impurities in the coating solution can compromise the overall performance of the coating. Utilize filtered liquids to avert infection.

✓ **Soaking time:** Soaking duration influences the coating's thickness. Adjust soaking duration according to the required coating thickness.

✓ **Withdrawal velocity:** The velocity at which the substrate is extracted from the coating solution influences the uniformity of the coating. Ensure uniform withdrawal velocities.

✓ **Coating cycles required:** Multiple coating cycles may be necessary to attain the appropriate thickness. Enhance cycle durations according to coating specifications.

✓ **Type and concentration of the solution substance:** The kind and concentration of the coating solution influence coating efficacy. Selecting the appropriate paint for your project is essential.

✓ **Environmental conditions:** Aspects including humidity, temperature, and ventilation can influence coating quality. Ensure appropriate environmental conditions for uniform outcomes.

✓ **Equipment calibration:** Consistent calibration of the dip coating apparatus guarantees precision and reproducibility of outcomes.

II.3 Characterisation techniques of thin film

Thin films are often defined by their structural, morphological, and optical characteristics. This section provides a concise discussion of the characterisation tools employed in this study.

II.3.1 X-ray diffraction analysis (XRD)

XRD analysis is a method employed for the detection and identification of crystalline phases within a material. When electromagnetic radiation of a wavelength (λ) equivalent to the atomic spacing of the crystal, specifically λ ~ 0.1 nm, interacts with the material, it experiences diffraction of the incident wave. Consequently, X-rays will undergo diffraction when interacting with crystalline substances (Figure II.6). Diffraction can be mathematically articulated by Bragg's equation of diffraction (II.4).

$$2d\sin\theta = n\lambda \qquad \text{(II.4)}$$

d represents the interplanar spacing of a certain set of planes, θ denotes the angle between the incident (or diffracted) ray and the corresponding crystal planes, and n is an integer known as the order of diffraction, often equal to one **(1).**

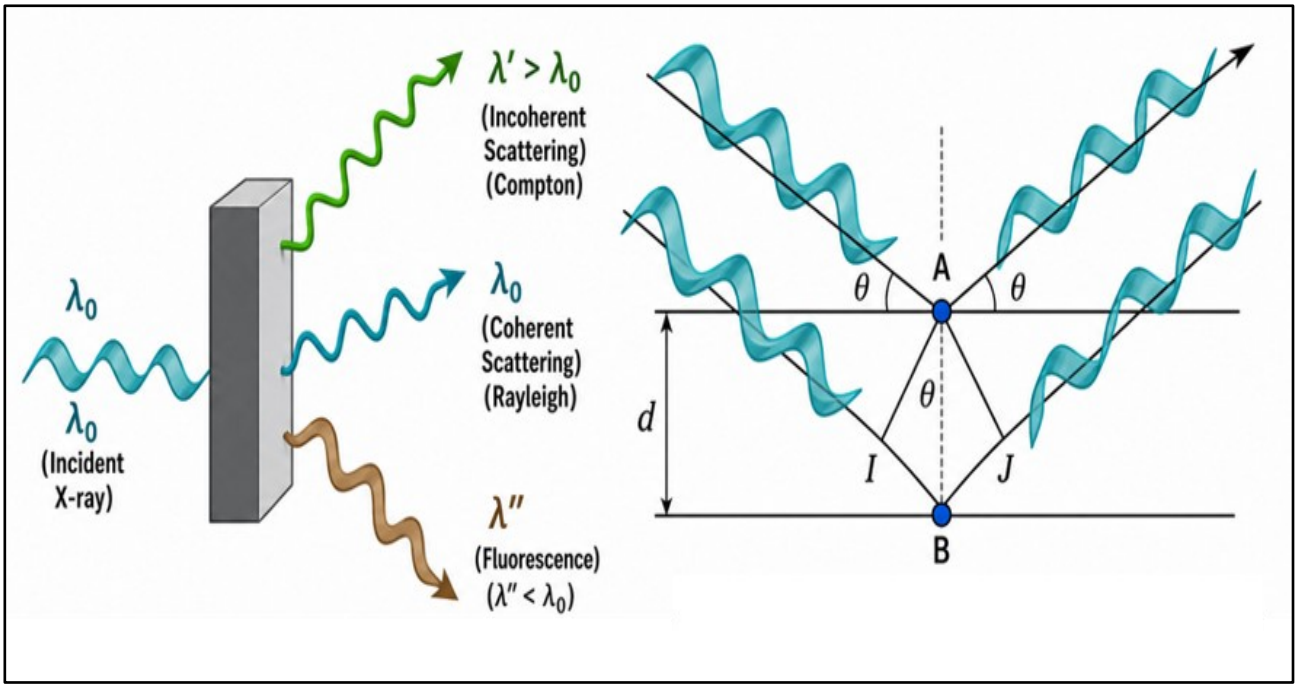


Figure II.6: A graphic depiction of the interaction between X-rays and matter, along with the condition for reflection as defined by Bragg's law [64].

A Bruker D8 Discovery diffractometer (Figure II.7) with a 20°–80° range and Cu Kα radiation (λ = 1.54184 Å) was used to perform the DRX analysis.

Based on the distinctive D8 XRD family platform, Bruker's D8 ADVANCE is ideal for all X-ray powder diffraction and scattering applications, such as: Conventional powder diffraction for X-rays (XRD), Analysis of Pair Distribution Functions (PDF), and X-ray scattering at small and wide angles [SAXS (Small-Angle X-ray Scattering), WAXS (Wide-Angle X-ray Scattering)]. The D8 ADVANCE's exceptional versatility allows it to measure any kind of sample on a single device, including liquids, loose powders, thin films, and solid blocks [65].



Figure II.7: Brucker D8 ADVANCE diffractometer [65]

The goal of the diffraction experiment, as it is now understood, is to give quantitative data on the shape characteristics (SC, BCC, FCC, Wurtzie, mix) and volume unit cell (the lattice parameters). The phase correlations between the radiation scattered by each atom in the unit cell determine the intensity of diffraction peaks. Generally speaking, the qualitative phase analysis of the diffraction pattern of XRD analysis will be compared with the International Center for Diffraction Data (ICDD) and other standard crystallographic databases to expedite the phase identification of a material in a range of crystalline specimens [66].

Microstructural parameters such crystallite size (D, Debye-Scherrer equation), dislocation density (d), micro-strain, and X-ray density were also measured using an X-ray diffractometer (XRD). [31], [67].

$$D_{(hkl)} = \frac{K\lambda}{\beta \cos\theta} \qquad \text{(II.5)}$$

Where D (002) is crystallite size based on plan (002), β is the full width at half maximum (FWHM), θ is the Bragg's angle, k is the correction constant (0.94), λ is the X-ray wavelength (1.54 Å) [68], [69].

$$\delta_{(hkl)} = \frac{1}{D_{(hkl)}^{\ 2}} \qquad \text{(II.6)}$$

$$\varepsilon_{(hkl)} = \frac{\beta}{4\tan\theta} \quad \text{(II.7)}$$

The lattice parameters (a=b and c), interplanar spacing (d), and volume of the unit cell (V_{cell}) of the hexagonal ZnO structure were calculated using the following equations [70]:

$$d_{hkl} = \frac{1}{\sqrt{\frac{4}{3a^2}(h^2+k^2+hk)+(\frac{l}{c})^2}} \quad \text{(II.8)}$$

$$d_{hkl} = \frac{\lambda}{2\sin\theta} \quad \text{(II.9)}$$

$$V_{cell} = \frac{\sqrt{3}}{2} a^2 c \quad \text{(II.10)}$$

The following equations were utilized to determine Atomic Packing Factor, and degree of crystal lattice distortion for the samples hexagonal structure [71], [72].

$$APF = \frac{2\pi a}{3c\sqrt{3}} \quad \text{(II.11)}$$

$$R_{(hkl)} = \frac{2a}{c}\sqrt{\frac{2}{3}} \quad \text{(II.12)}$$

For the hexagonal structure of ZnO, the Zn–O bond length, L, and positional parameter (u) are calculated using the following relations [31], [73].

$$l = \sqrt{\frac{a^2}{3} + (\frac{1}{2} - u)^2 c^2} \quad \text{(II.13)}$$

$$u = \frac{a^2}{3c^2} + 0.25 \quad \text{(II.14)}$$

The positional parameter (u) in the wurtzite structure represents the displacement of an atom in relation to the next atom along the c-axis. It quantifies the extent of this displacement.

The bond angles, α and β, (in radians) are ascertained using the subsequent equations [71]:

$$\alpha = \frac{\pi}{2} + arc\cos[1 + (3\left(\frac{c}{a}\right)^2\left(\frac{1}{2} - u\right)^2)]^{-\frac{1}{2}} \quad \text{(II.15)}$$

$$\beta = 2arc\sin[\frac{4}{3} + (4\left(\frac{c}{a}\right)^2\left(\frac{1}{2} - u\right)^2)]^{-\frac{1}{2}} \quad \text{(II.16)}$$

X-ray density ($\rho_{X\text{-}ray}$) and specific surface area (S^*) were obtained from the following equations [74], [75]:

$$\rho_{x-ray} = \frac{ZM}{V_{cell} N_a} \quad \text{(II.17)}$$

$$S^* = \frac{6000}{\rho_{x-ray}\, D} \quad \text{(II.18)}$$

where a, b, and c are the lattice parameters, Z is the coordination number of the unit cell (i.e., the number of atoms per unit cell), M is the molecular weight of the sample, and Na is Avogadro's number.

II.3.2 Morphological analysis

The sophisticated form of microscopy known as Field Emission Scanning Electron Microscopy (FE-SEM) generates electrons from a field emission cannon. As a result, FE-SEM achieves a high level of spatial resolution by using a smaller beam size than traditional scanning electron microscopy (SEM). Consequently, FE-SEM achieves a high level of spatial resolution by using a smaller beam size than traditional scanning electron microscopy (SEM). Furthermore, this microscopy modality is especially sensitive to the most electron beam-sensitive samples because it permits the use of extremely low voltages, which reduces the charging impact. For an assessment of extremely fine cell surface characteristics, FE-SEM is a crucial tool in this regard [76].

The most adaptable high-resolution low-vacuum FEG SEM with extended low-vacuum capabilities for extremely difficult samples and dynamic experiments is the Quattro S FESEM, a field emission scanning electron microscope that can generate and collect all available information from any type of sample material. By freely and easily switching between three vacuum modes, the Quattro S can be used to investigate materials that are conductive, non-conductive, and incompatible with high vacuum (Figure II.8) [77].

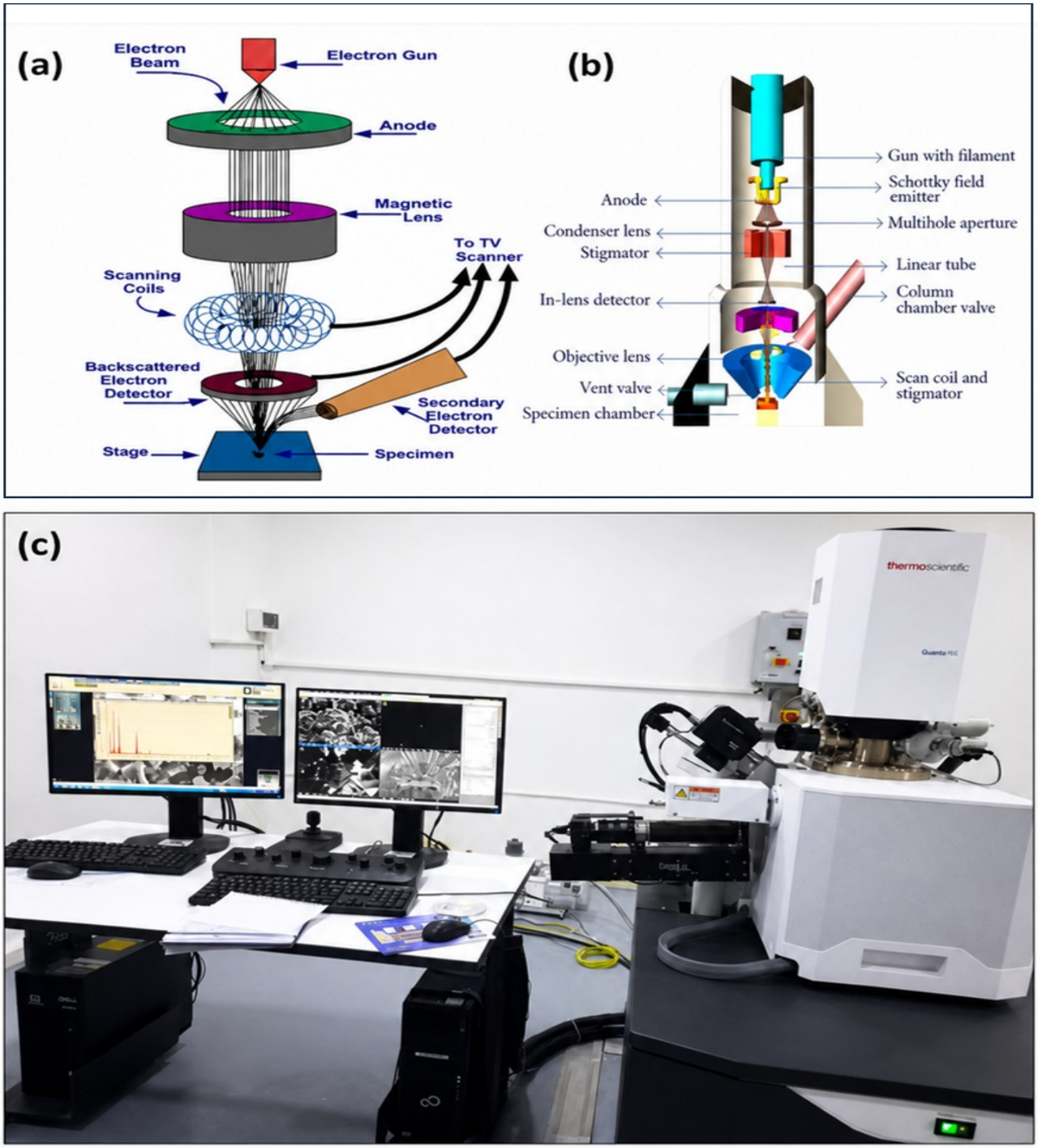


Figure II.8: Schematic diagram of FESEM (**a**) and its operating principle (**b**) [78], and The Thermo Scientific Quattro S, FESEM equipment (**c**).

II.3.3 Energy Dispersive X-ray Spectroscopy (EDX or EDS)

Energy-dispersive diffraction spectroscopy (EDX, sometimes also called EDS or EDXS) is a robust and frequently used method for physical and chemical characterisation as well as imaging.[79].

Energy-dispersive X-ray spectroscopy (EDS) is frequently employed to analyse elemental composition and distribution (mapping) in nanomaterials. The EDS detector is integrated into both SEM and TEM systems, with measurements conducted at elevated energy levels. The material surface is subjected to high-energy electron bombardment, resulting in the ejection of an electron from the inner shell and the creation of a vacancy. An X-ray photon is emitted when high energy levels transition to lower levels, as seen in Figure II .9 (a), and is subsequently detected by the EDS detector. The emitted X-rays can be assigned to each element in the sample and depicted as a spectrum or mapping [80]. Production of X-rays in the electron microscope. Primary beam electrons (energy E_0) interact with sample atoms in various manners: non-interaction, elastic interaction, or inelastic interaction involving energy transfer to the sample (Figure II.9 (b)). The former can result in the production of secondary electrons ($E < 50$ eV) or Auger electrons (50 eV $< E <$ 3 keV), the emission of radiation as visible light (cathodoluminescence), characteristic X-rays, or bremsstrahlung X-rays, the excitation of plasmons (5 eV $< E < 30$ eV), or the heating of the sample through phonon excitation ($E \sim$ meV) [79].

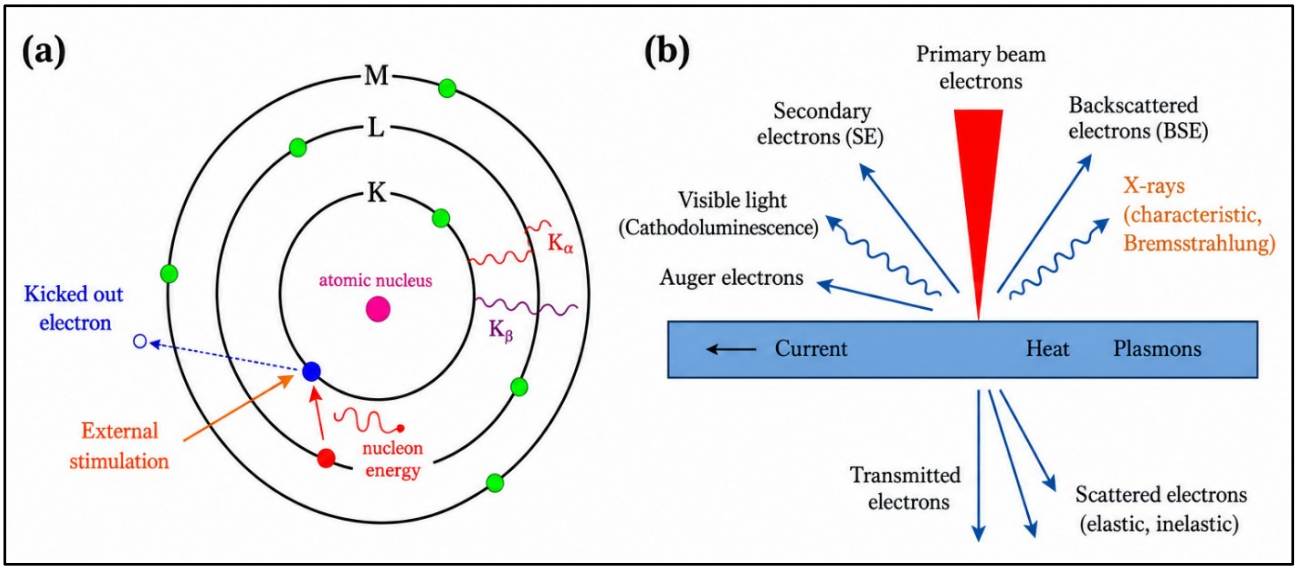


Figure II.9: (**a**) Graphical representation of X-ray emission during electron-atom interaction [80], and (**b**) Conventional interactions between electrons and specimens in the electron microscope [79].

II.3.4 Atomic force microscope (AFM)

Among scanning probe microscopy techniques (Figure II.10), atomic force microscopy (AFM) is the most widely utilized analytical tool due to its versatility in examining both conductive and nonconductive materials, and its capability to function in various environments, including ambient, liquid, and vacuum conditions (including ultra-high vacuum (UHV)) [80], [81]. The scanning probe microscope (SPM) has emerged as a crucial tool for the characterisation of nanomaterials due to its diverse uses. SPM facilitates the examination of surface characteristics, including friction, thermal conductivity, mechanical properties, magnetism, electrical properties, and adhesion, with nanoscale precision. The analysis can be conducted by two probe-sample interactions, wherein the probe scans the sample and the sample scans the probe at a 100 nm configuration. The initial scanning probe microscopy (SPM) was the scanning tunnelling microscope, and technological advancements have facilitated the development of specialized SPMs, like the atomic force microscope (AFM), magnetic force microscope, and electric force microscope, which can operate in various environments, such as ambient conditions and ultrahigh vacuum. Moreover, a recent study employed STEM for the first time to investigate the surface during a catalytic process [81], [82].

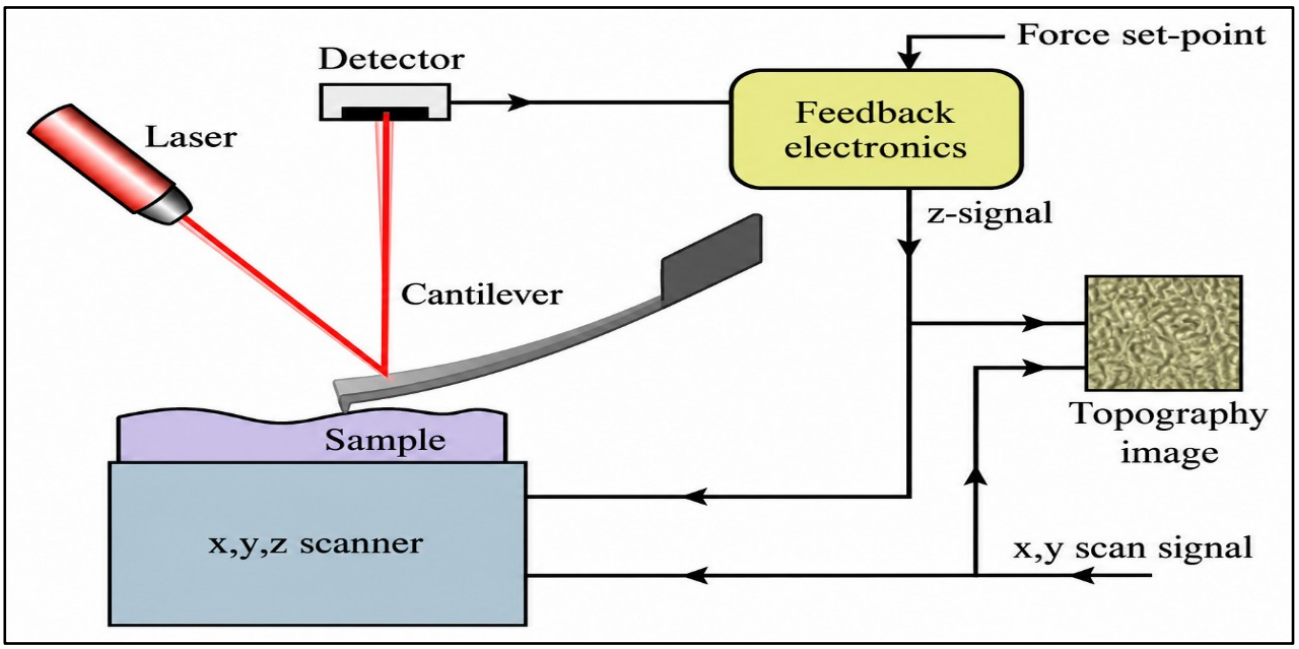


Figure II.10: Schematics of atomic force microscopy operation (static mode) [82].

II.3.5 Optical properties (UV-VIS Spectroscopie)

In a UV-Vis (ultraviolet-visible) spectroscopic test, light absorption as a function of wavelength reveals information regarding the electronic transitions occurring within the substance. The fraction of transmitted light is governed by the Beer-Lambert law, which posits that the ratio of light intensity after interacting with the sample (I, typically quantified as transmittance or reflectance) to the incident intensity (I0) is contingent upon the path length of light through the sample (l), the absorption cross section (r) of the transition, and the disparity in population between the initial state (N1) and final state (N2) of the electronic energy levels (E1 and E2) (Figure.11(a,b)) [83].

$$\frac{I}{I_0} = e^{-\sigma(N_1 - N_2)l} \qquad \text{(II.19)}$$

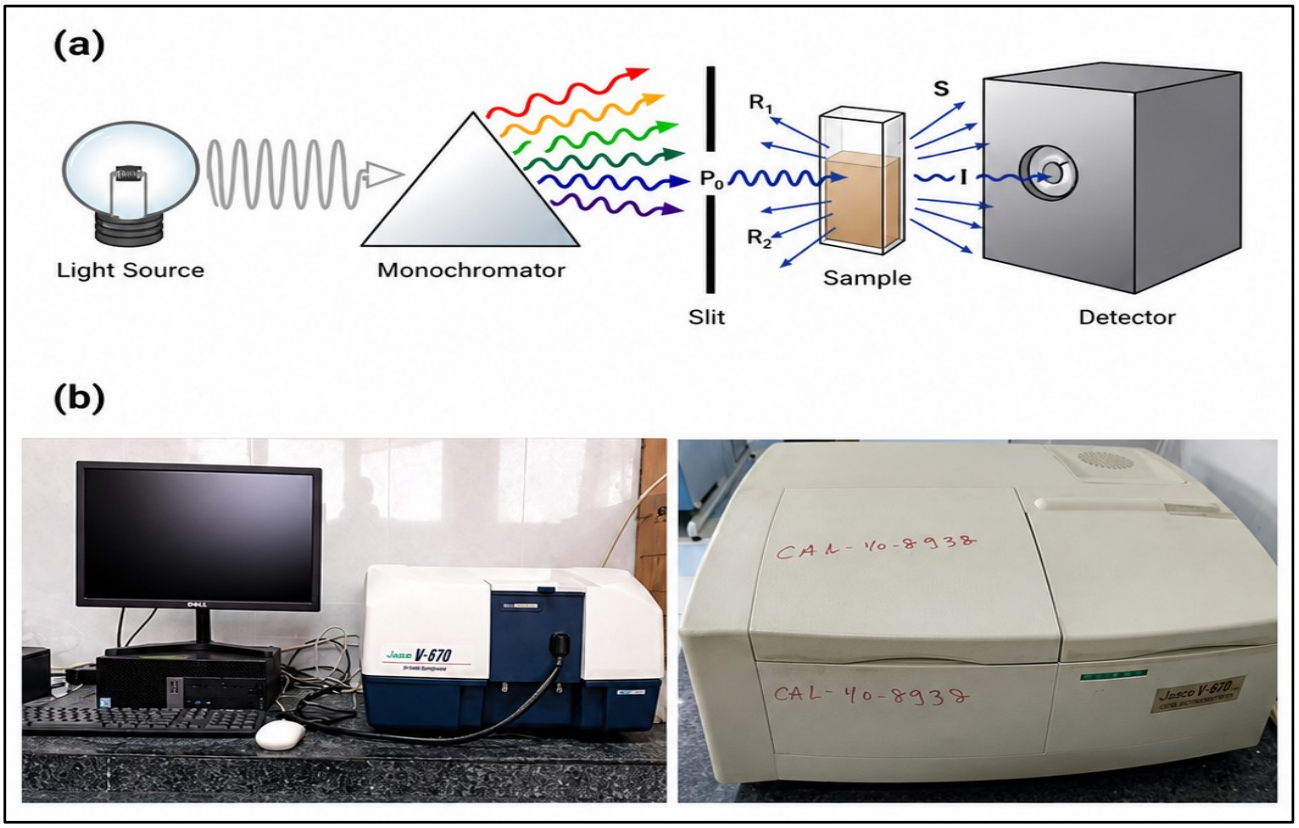


Figure II.11: (**a**) Single beam UV-Vis transmission setup with the monochromator positioned before to the sample [83], and (**b**) the SpectroScan 80D device with V-770 spectrophotometer.

This is sometimes expressed in a format known as Beer's Law [83]:

$$A = \varepsilon lc = -\log_{10}\left(\frac{I}{I_0}\right) \qquad \text{(II.20)}$$

$$A = \varepsilon lc = -log_{10}(\frac{I}{I_0}) \quad \text{(II.21)}$$

A represents absorbance, c denotes the concentration of the absorbing species, l signifies the path length of light traversing the sample, and ε indicates the molar absorptivity coefficient of the material. Be aware that the observed intensity of a genuine system may be complicated by transitions involving several initial and end states. The absorbance A can be standardized to the path length l of the light traversing the material (e.g., the thickness of a film), resulting in the absorption coefficient α [83].

$$\alpha(cm^{-1}) = \frac{\ln(10)A}{e(cm)} \quad \text{(II.22)}$$

UV-Vis spectroscopy provides an efficient means of estimating the optical band gap in semiconductors by examining electronic transitions between the valence and conduction bands. The optical band gap does not inherently equate to the electronic band gap, defined as the energy differential between the valence band maximum (VBM) and the conduction band minimum (CBM). However, it is frequently approximated as such due to the scarcity of practical methods for measuring the electronic band gap [83].

The optical band gap of studied films was calculated using the Tauc equation, as shown below [32]:

$$(\alpha hv) = A\left(hv - E_g\right)^n \quad \text{(II.23)}$$

In the aforementioned equation, α signifies the absorption constant, hv indicates photon energy, A is a constant, Eg represents the optical band gap, and the exponent n is contingent upon the transition nature of the material. The current study indicates that the value of n is 1/2, signifying a permitted straight transition.

The refractive index curve (n) of samples was ascertained by theoretical computations. The refractive index (n) and the extinction coefficient (k) were derived using equations (12), (13), (14) and (15) [32], [84] :

$$n = \left(\frac{1+R}{1-R}\right) + \sqrt{\frac{4R}{(1-R)^2} - k^2} \quad \text{(II.24)}$$

$$k = \frac{\alpha\lambda}{4\pi} \quad \text{(II.25)}$$

$$R = 1 - \sqrt{Texp(A)} \quad \text{(II.26)}$$

where R denotes reflectivity, α represents the absorption coefficient, k signifies the extinction coefficient, e indicates the sample thickness, and **λ** staV nds for the wavelength.

The refractive index can also be computed using the Hervé and Van Damme formula presented in equation (22)[85].

$$n = \sqrt{1 + (\frac{13.6}{E_g + 3.47})^2} \quad \text{(II.27)}$$

A straightforward method can be utilized to ascertain the band edge potential of the conduction band (CB) and valence band (VB) . The Butler and Ginley equations [86], [87] facilitate the calculation of the EVB and ECB of a semiconductor at its zero-charge state[88].

$$E_{CB} = \chi - E_e - 0.5\, E_g \quad \text{(II.28)}$$

$$E_{CB} = E_{VB} - E_g \quad \text{(II.29)}$$

Where χ denotes the absolute electronegativity of ZnO (5.9 eV), and Ee signifies the energy of free electrons on the hydrogen scale (about 4.5 eV).

Chapter III Synthesis and Characterisations of pure ZnO and sulfur-modified Zinc oxide thin layers for optoelectronic and environmental applications

III.1 Introduction

In this part, pure ZnO and sulfur-doped ZnO thin films were developed onto a glass substrate using the gel-sol technique and dip coating process. Additionally, we looked at the effects of sulfur doping on the ZnO films' structural, surface morphological and topographical, and optical properties, as well as their possible uses in photocatalysis and UV light detection.

III.2 Thin film manufacturing

III.2.1 Preparing the substrate

The films were made using low-cost, practical, typical glass slides that were 25.0 × 37.6 mm² in size and 1-2 mm thick. The glass substrates were ultrasonically cleaned with acetone, methanol, and distilled water for 15 minutes each, then stored in ethanol and dried just before use.

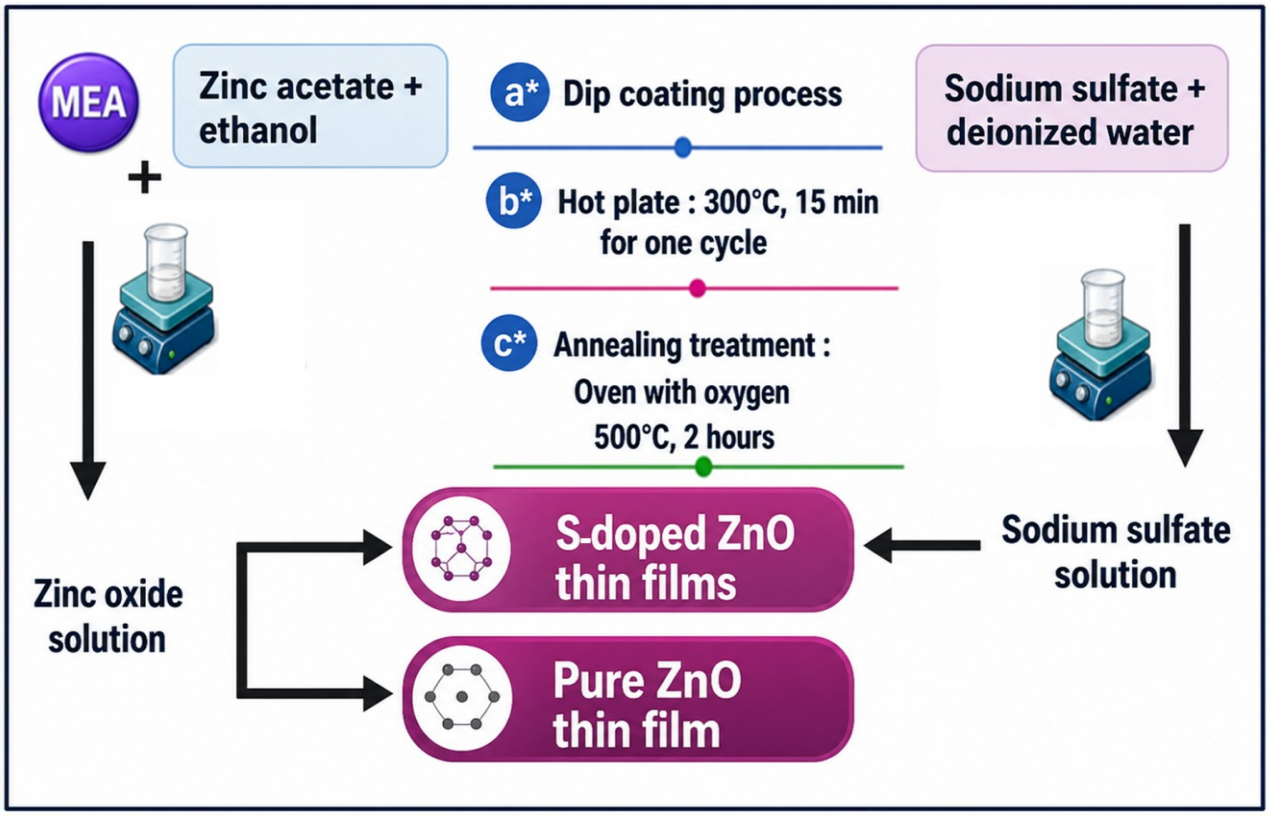


Figure. III.1: Demonstrates the procedure for preparing thin film samples via dip coating methodology.

III.2.2 Chemical and materials

The study utilised multiple chemicals, including zinc acetate dihydrate [Zn $(CH_3OO)_2$, $2H_2O$, 99 % purity, MERCK], ethanol [C_2H_6O, 99.8 % purity, VWR], sodium sulfate anhydrous [Na_2SO_4, ≥ 98 % purity, Sigma-Aldrich], monoethanolamine (MEA) [C_2H_7NO, 99 % purity, Sigma-Aldrich], ethanol [C_2H_6O, 99.8 % purity, VWR], methylene blue dihydrate (MB) [C16H18ClN3S, $2H_2O$,99 % purity, Sigma-Aldrich]. Thin films were fabricated at room temperature using a dip coating device (HOL-MARC HO-TH-02B).

III.6 Synthesis of thin films

The procedural steps for sample preparation using the sol-gel and dip-coating methods. Both undoped and S-doped ZnO thin films were deposited onto glass substrates, Initially, a 0.4 M solution of zinc acetate was prepared in a mixture of ethanol and MEA (30 mL and 0.4 mL respectively). This solution was stirred for thirty minutes at room temperature and then heated to 50 ◦C for two hours until it became transparent. Deionised water served as the solvent for preparing a sodium sulfate solution of 10 mL for each model at two different weight percentages, based on mass concentration (5 % and 2 %). This solution was stirred for one hour at 80 ◦C. The resulting solutions were then combined with the previously prepared pure zinc oxide and stirred for two hours at 50 ◦C. The prepared solutions were kept at room temperature for 48 h before being applied via dip coating. Each layer was dip coated onto glass substrates, and all thin films were dried for 15 min at 300 ◦C. The process was completed by annealing in an oven set at 500 ◦C for two hours after the deposition of twenty layers.

IV.3 Results and discussion

IV.3.1 Structural investigation

Figure III.1 illustrates the X-ray diffraction examination of S-doped ZnO thin films, as well as pure ZnO thin films at varying dopant concentrations Fig. 2. Seven different peaks are observed within the diffraction angle range of 30° to 70°, corresponding to the (100), (002), (101), (102), (110), (103), and (112) planes. The peaks align with the ZnO reference pattern, as shown by the standard ICDD card number 00–036-1451. The XRD results showed no evidence of secondary phases or impurities, such as peaks related to ZnS or sulfur, likely due to the low S concentration (below 5 %), highlighting the success of the doping method. The graphical data shows that all samples have hexagonal wurtzite crystal structures, which match the space group P63mc [89], [90]. The hexagonal wurtzite phase of ZnO is acknowledged as the most

thermodynamically stable among the many ZnO phases [67] . The crystalline quality is assessed by the intensity and full width at half maximum (FWHM), as shown in prior research. Each sample displays a distinct and acute peak associated with the (002) plane, and no displacement in the XRD peaks was seen upon the introduction of the S dopant. This indicates that ZnO crystals preferentially align perpendicularly to the substrate surface along the c-axis [30]. The (002) plane, being the predominant peak, is selected for additional investigation and computations. In the diffractogram for pure ZnO, the (103) peak exhibits the highest relative intensity. This is attributed to the structure factor Fhkl, where the arrangement of Zn and O atoms within the unit cell results in maximum constructive interference for the (103) plane compared to other reflections. As sulfur is incorporated into the lattice at 2% and 5% concentrations, a systematic decrease in diffraction intensity is observed, particularly for the (103) peak. This reduction suggests: lattice Distortion, defect-induced disorder, microstrain
The microstructural parameters, including crystallite size (D), dislocation density (δ), and micro-strain (ε), determined using XRD, are illustrated in Figure III. 1(a), while x-ray density, specific surface area, and bond length are depicted in Figure III. 1(b).

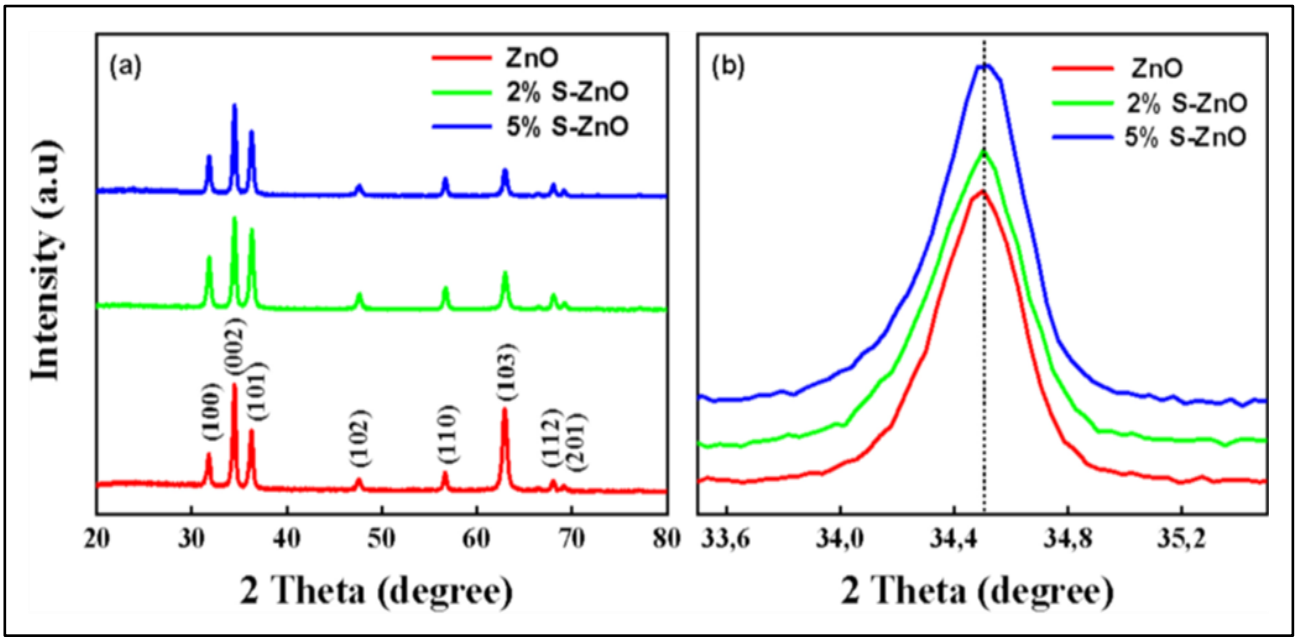


Figure. III.2: (**a**) XRD patterns of pure and sulfur-doped ZnO nanostructured thin films at varying sulfur doping concentrations; (**b**) strong diffraction peaks (002) in the XRD of the samples.

Microstructural characteristics such crystallite size (D), dislocation density (d), micro-strain, and X-ray density were also measured using an X-ray diffractometer (XRD) and are shown in

Table III.1.

The crystallite size of the 2% S-doped ZnO film diminished from 26.71 nm in pure ZnO to 24.59 nm, as illustrated in Figure III. 2(a). Notably, the crystallite size of the 5% S-doped ZnO film was marginally greater than that of the 2% S-doped ZnO film. Research indicates that doping ZnO with sulfur alters crystallite size, resulting in a reduction upon sulfur incorporation [91], [92]. This discovery indicates that the ZnO lattice was doped with low-valent sulfur, implying that the dopants impede crystallite formation. Additionally, the research demonstrates that dopants induce lattice distortions and defects, resulting in heightened internal stresses, as indicated by the increase in micros trains with doping. The positive micro strain values depicted in Figure III. 2(a) signify tensile strain ε, which correlates with the existence of impurities or defects, ion exchanges involving atoms of varying ionic radii, and discrepancies in the lattice constant [93]. The introduction of sulfur into the ZnO crystal lattice likely accounts for the tensile strain seen in this study, as it reduces crystallite size and enhances lattice characteristics. Our results correspond with the current literature, which has documented analogous phenomena for S-doped ZnO [91], [92]. Figure III. 2(b) depicts the established Zn-O bond length measurements. According to the ionic radii of O^{2-} (1.40 Å) and Zn^{2+} (0.74 Å), the anticipated Zn-O bond length is 1.9525 Å; yet, the measured values in all films exceed 1.9725 Å. It is generally accepted that dopants are often inserted or substituted according to the size of the doping ions and the electronegativity of the participating atoms [94]. Sulfur (S^{2-}), the dopant, possesses a greater ionic radius (1.84 Å) compared to oxygen (O^{2-}), which measures 1.40 Å. With a Pauling electronegativity of 2.58, sulfur exhibits lower electronegativity than oxygen, which is valued at 3.44. The disparity in electronegativity is especially pronounced when contrasting ZnO and ZnS, with values of (Zn, O) (1.65, 3.44) for ZnO and (Zn, S) (1.65, 2.58) for ZnS. Thus, Zn^{2+} ions demonstrate a greater affinity for O^{2-} ions compared to S^{2-} ions [95], [96]. Shorter bond lengths generally arise from a greater divergence in electronegativity between elements [96]. Consequently, the S-Zn bond length exceeds the O-Zn bond length between sulfur and zinc (as illustrated in Figure III. 2(b)). The finding shows that there are structural problems, particularly oxygen vacancies [97], when sulfur is added to the ZnO lattice. The specific surface area (S*) rose from 41.574 to 43.92 m^2/g, although the X-ray density marginally declined from 5.722 to 5.718 g/cm^3 (as illustrated in Figure III. 2(a)).

Table III. 1: Structural properties obtained from XRD data for all thin films produced via the dip coating process.

Samples	(hkl)	d_{hkl} (A°)	lattice parameters (A°)		Volume V_{celle} $(A°)^3$
			a=b	c	
ZnO	(100)	2.8093	3.2414	5.1924	47,246
	(002)	2.5974			
2% S-ZnO	(100)	2.8072	3.2418	5.1939	47,271
	(002)	2.5964			
5% S-ZnO	(100)	2.8082	3.2421	5.1952	47,292
	(002)	2.5959			

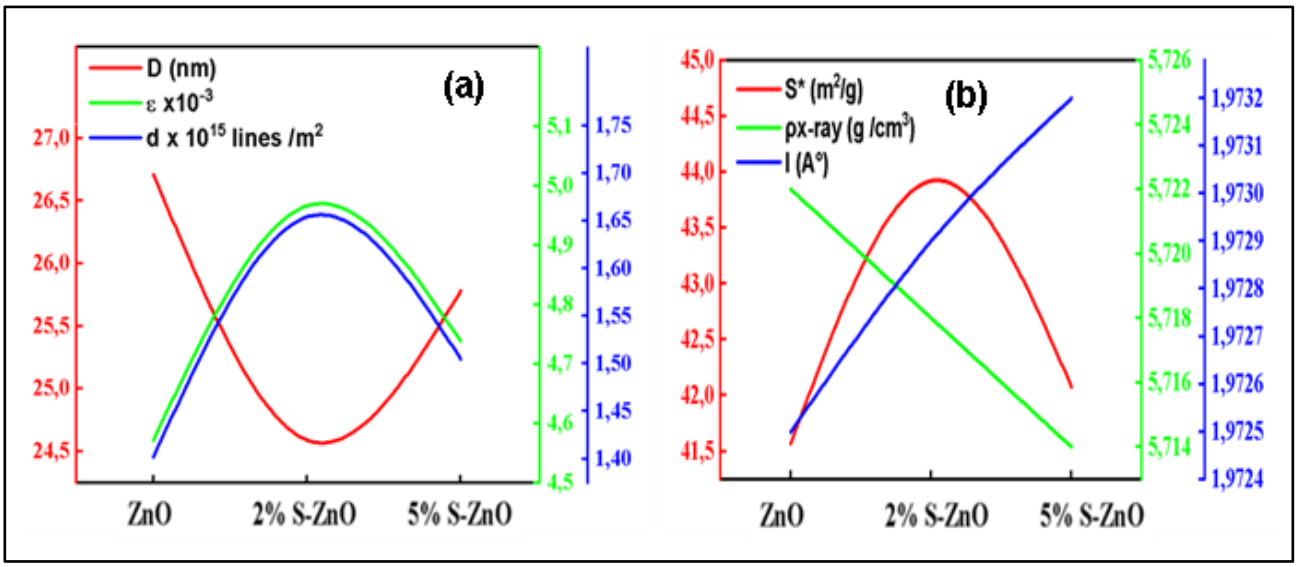


Figure. III.3: Structural parameters: (**a**) crystallite size, micro-strain, and dislocation density; (**b**) bond length, X-ray density, and specific surface area.

III.3.2 Morphological investigation

Scanning Electron Microscopy (SEM) was employed to evaluate the surface morphologies of both undoped and sulfur-doped ZnO thin films, as depicted in Figures III. 3(a-c). Grain size and porosity were assessed utilizing ImageJ software. The data acquired via ImageJ analyses enabled us to generate histograms of grain size distribution and ascertain the average grain size. The outcomes are presented in Figure III. 4(a–d). In ImageJ, film porosity is quantified as a percentage of area (% area). The SEM pictures demonstrated significant alterations in surface morphology according to the doping levels. Figure III. 3(a) displays the SEM image of undoped ZnO, revealing a uniform, homogenous, and smooth surface characterized by equally distributed spherical particles, with an average grain size of 268.304 nm and a porosity of 23.216% (Figure III 3(a, d)). Conversely, the 2-wt% sulfur-doped thin film (Figure III. 3(b, d))

exhibits wrinkles and diminutive spherical particles, characterized by an average grain size of 174.225 nm and a porosity of 15.162 %; these wrinkles are interconnected. The irregularities augmented the film's surface area beyond initial projections, potentially improving catalytic activity. Upon elevating the sulfur concentration to 5 wt%, the wrinkles diminished, and their density reduced, yielding an average grain size of 185.535 nm and a porosity of 21.606% (Figure III. 4(c, d)). The incorporation of S atoms into the ZnO lattice chiefly accounts for the noted decrease in grain size of S-ZnO films, relative to pure ZnO, along with the morphological alterations [98]. The X-ray analysis section indicates that the microstress values grow and become positive, signifying tensile stress. This is attributable to the greater ionic radius of sulfur in comparison to oxygen (S^{2-}/O^{2}-: 1.84 Å / 1.40 Å). This favorable reading indicates the existence of impurities or defects, ion exchanges with atoms of differing ionic radii, and discrepancies in the lattice constant. Doping typically causes modest distortions in the crystal structure, as seen by the subtle alterations noted in the doped samples [93]. Notably, the grain size measurements surpass the crystallite size established via SEM and XRD analytical methods. Scanning Electron Microscopy (SEM) displays spherical morphologies with diminutive grain sizes, resulting in multiple grain boundaries and an ensuing scattering effect. XRD examination, conversely, verifies that the grains consist of several distinct crystals. This discovery aligns with the findings of Aradhana and Goktasa [99], [100], in addition to the theoretical contributions of Straumal [101]. The specific grain boundary area (area-to-volume ratio) is determined by the equation SGB = 1.65/GS, where GS denotes the mean grain size. [99], [100]. The computed SGB values for both pristine and S-doped ZnO thin films are around 61.5×10^5, 94.71×10^5, and 88.93×10^5 m^2/m^3 for ZnO, 2% S-ZnO, and 5% S-ZnO thin films, respectively.

Figure III. 5(a-c) presents the EDS spectra along with the composition tables for both undoped and S-doped ZnO samples applied to glass substrates. The study verifies the existence of elemental peaks associated with Zn, S, and O. The atomic percentages of sulfur prior to activation do not align with the elemental composition seen after activation, as demonstrated in Figure III. 5 and discussed in the XRD section. This contradiction can be ascribed to sulfur's reduced Pauling electronegativity (2.58) relative to oxygen (3.44), alongside its greater ionic radius, with ionic radii of O^{2-} and S^{2-} measuring 1.40 Å and 1.84 Å, respectively.

[95], [96], [102]. In the pure ZnO thin film, the atomic percentages of oxygen and zinc are 63.81% and 9.77%, respectively (Figure III. 5(a)). The atomic percentages of oxygen, zinc, and sulfur in the 2% S–ZnO thin film are 53.69%, 21.98%, and 0.46%, respectively (Figure III. 5(b)). In the 5% S–ZnO films, the atomic percentages of oxygen, zinc, and sulfur are 53.08%, 24.69%, and 0.99%, respectively (Figure III.5(c)). As the dopant concentration rises, the atomic proportion of oxygen diminishes owing to sulfur's incorporation into the ZnO lattice. In contrast, the atomic percentage of zinc increases with elevated sulfur doping, an essential modification to preserve charge neutrality between the negative charges from sulfur (S^{2-} and O^{2-}) and the positive charges from zinc (Zn^{2+}) within the lattice [103]. Moreover, the EDS spectrum reveals supplementary elements, including silicon (Si) and calcium (Ca), presumably derived from the glass substrates [104].

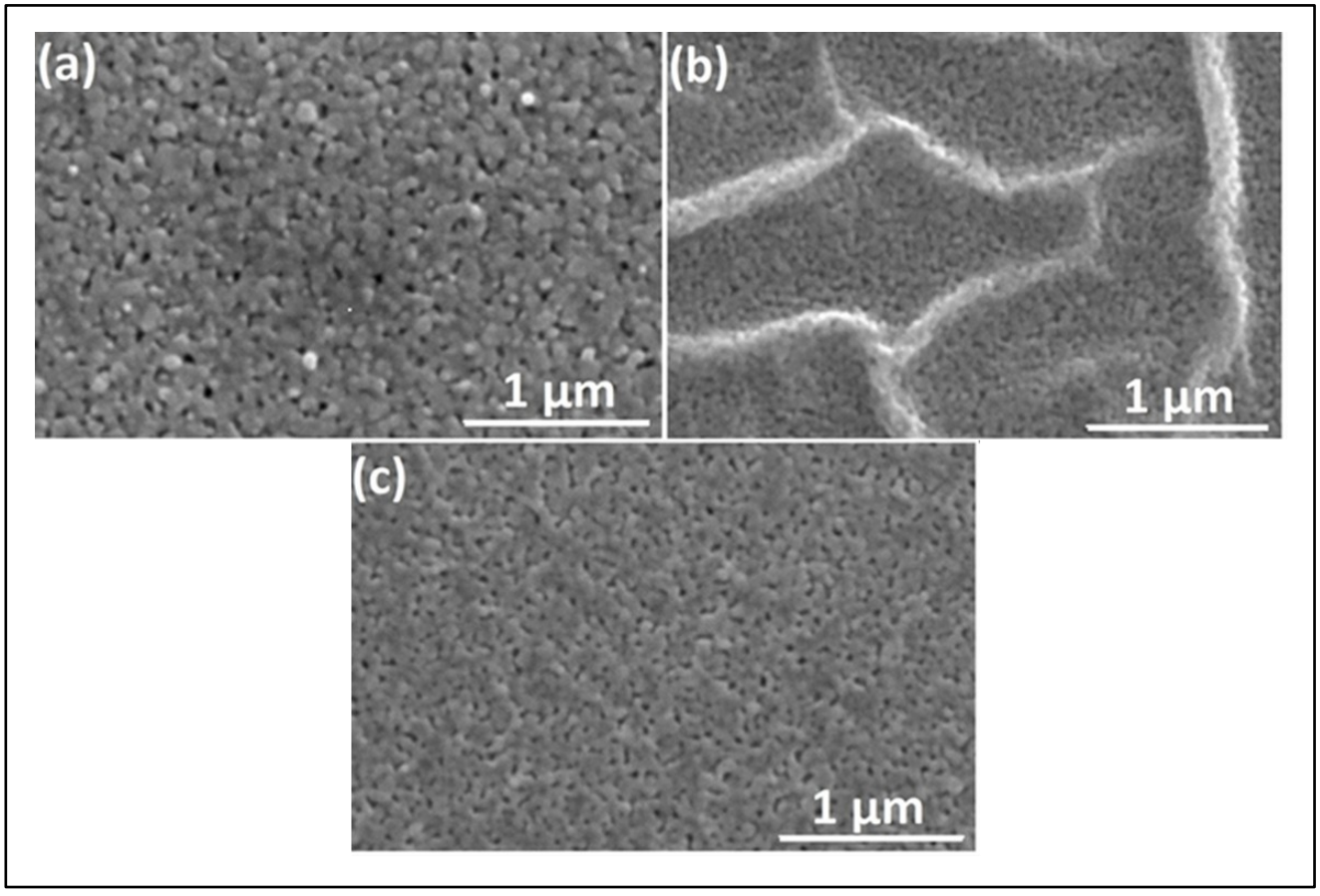


Figure III.4: SEM images of (**a**) ZnO, (**b**) 2% S-ZnO, (**c**) 5% S-ZnO thin films.

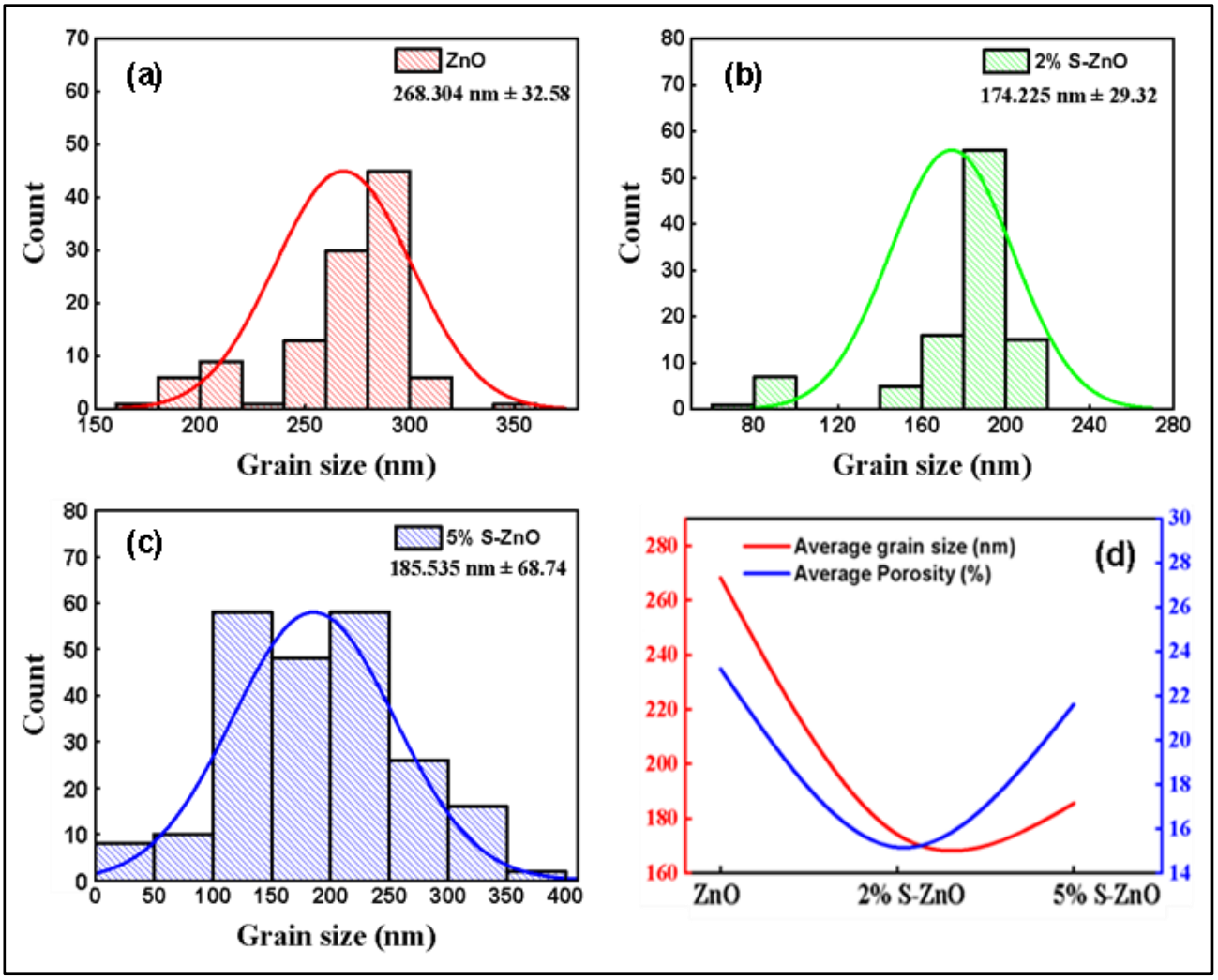


Figure III.5: Histograms distribution of grain size for samples (**a**) ZnO, (b) 2% S, and (**c**) 5% S-ZnO, to gether with (**d**) porosity and average grain size.

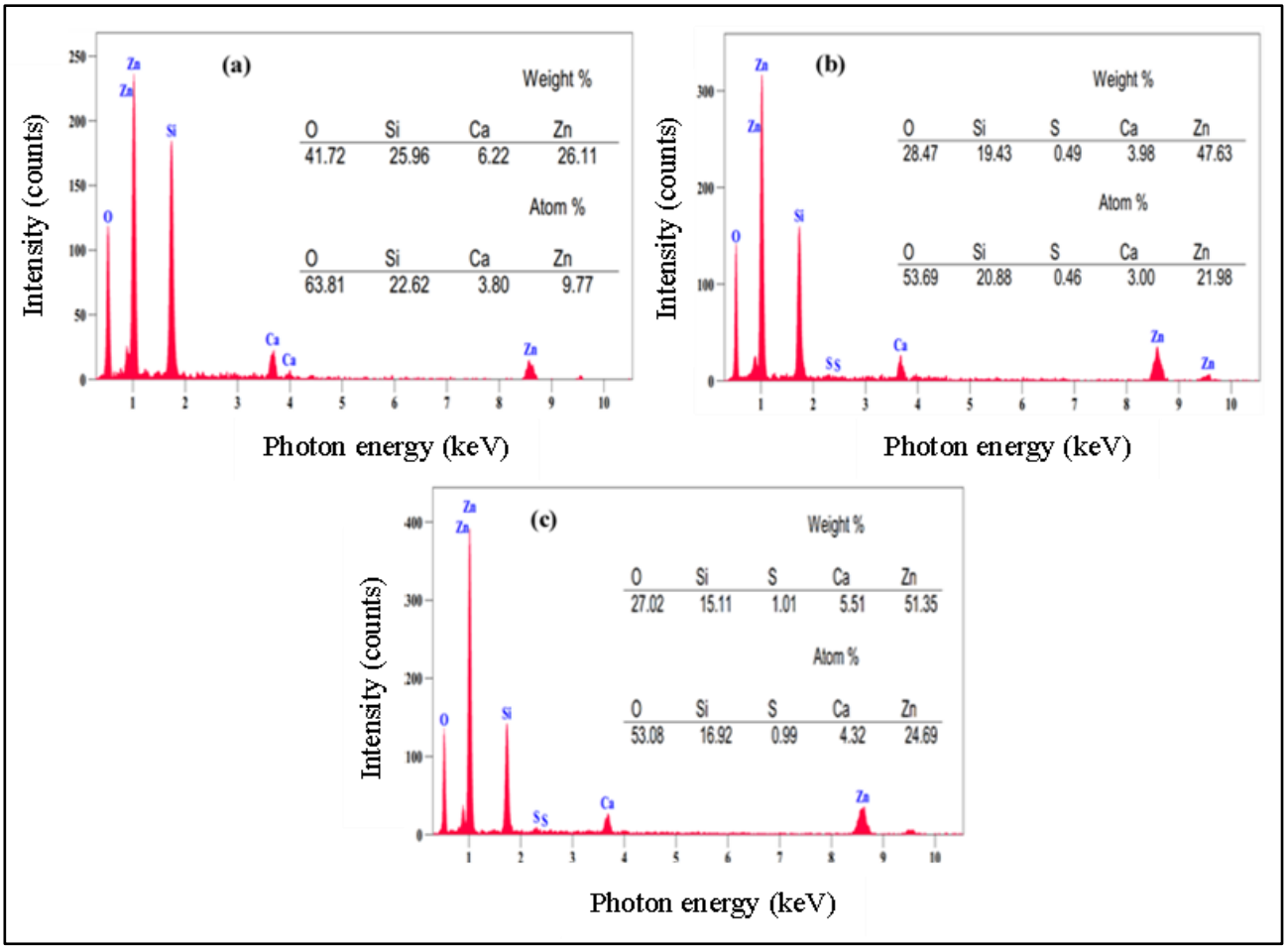


Figure III. 6: The EDS pictures of the as-deposited films: (**a**) ZnO, (**b**) 2% S-ZnO, and (**c**) 5% S-ZnO.

III.3.3 Topographical investigation (AFM)

Atomic force microscopy (AFM) is an essential method for assessing surface morphology quality, determining surface area, lateral particle size, and surface roughness. Figure III. 6(a-c) presents the two-dimensional (2D) and three-dimensional (3D) AFM images, accompanied by an enlarged view of pure and sulfur-doped ZnO films. The materials were analyzed utilizing high-resolution AFM pictures in contact mode, covering a scanning area of 5.0 × 5.0 μm². The surfaces of the films in Figure III. 6(a) and (c) are defined by uniformly structured, homogenous, dense, and coarse. In contrast, Figure III. 6(b) displays an inhomogeneous, uneven film that is less dense than those shown in Figure III. 6(a, c) and exhibits wrinkles. Table III. 2 encapsulates the findings of Gwyddion's computations regarding surface area, mean roughness (Sa), and root-mean-square (RMS) roughness derived from these pictures. The RMS

roughness (sq) values for the pure (a) and S-doped films (b-c) are 3.321, 3.879, and 3.690 nm, respectively. The mean roughness values of samples (a), (b), and (c) are 2.646, 3.185, and 2.980 nm, respectively.

Thus, the topography of Figure III. 6(b) exhibits greater density than that of Figure III. 6(a, c), resulting in surface area values of (a) 28.66, (b) 29.82, and (c) 29.55 µm². The 2% S-doped ZnO exhibits inhomogeneity, the smallest grain size, and a densely packed surface, while the undoped and 5% S-doped ZnO films demonstrate greater grain sizes and less dense surfaces relative to the 2% S-doped ZnO. The entire substrate surface is evidently coated with small grains, with certain areas exhibiting irregularly dispersed agglomerations of grains that are abundant in wrinkles. A coarse surface facilitates the adsorption of organic compounds, making it ideal for photoelectrocatalytic applications [32], [105]. These findings correspond with our scanning electron microscopy analysis, which demonstrated a 2% increase in RMS roughness for the S-ZnO thin film.

Table III.2: The mean roughness, root mean square roughness, and surface area of the samples were determined using Gwyddion software based on AFM images.

Samples	**ZnO**	**2% S-ZnO**	**5% S-ZnO**
root mean square roughness (nm)	3.321	3.879	3.690
Mean roughness (nm)	2.646	3.185	2.980
Surface area (µm²)	28.66	29.82	29.55

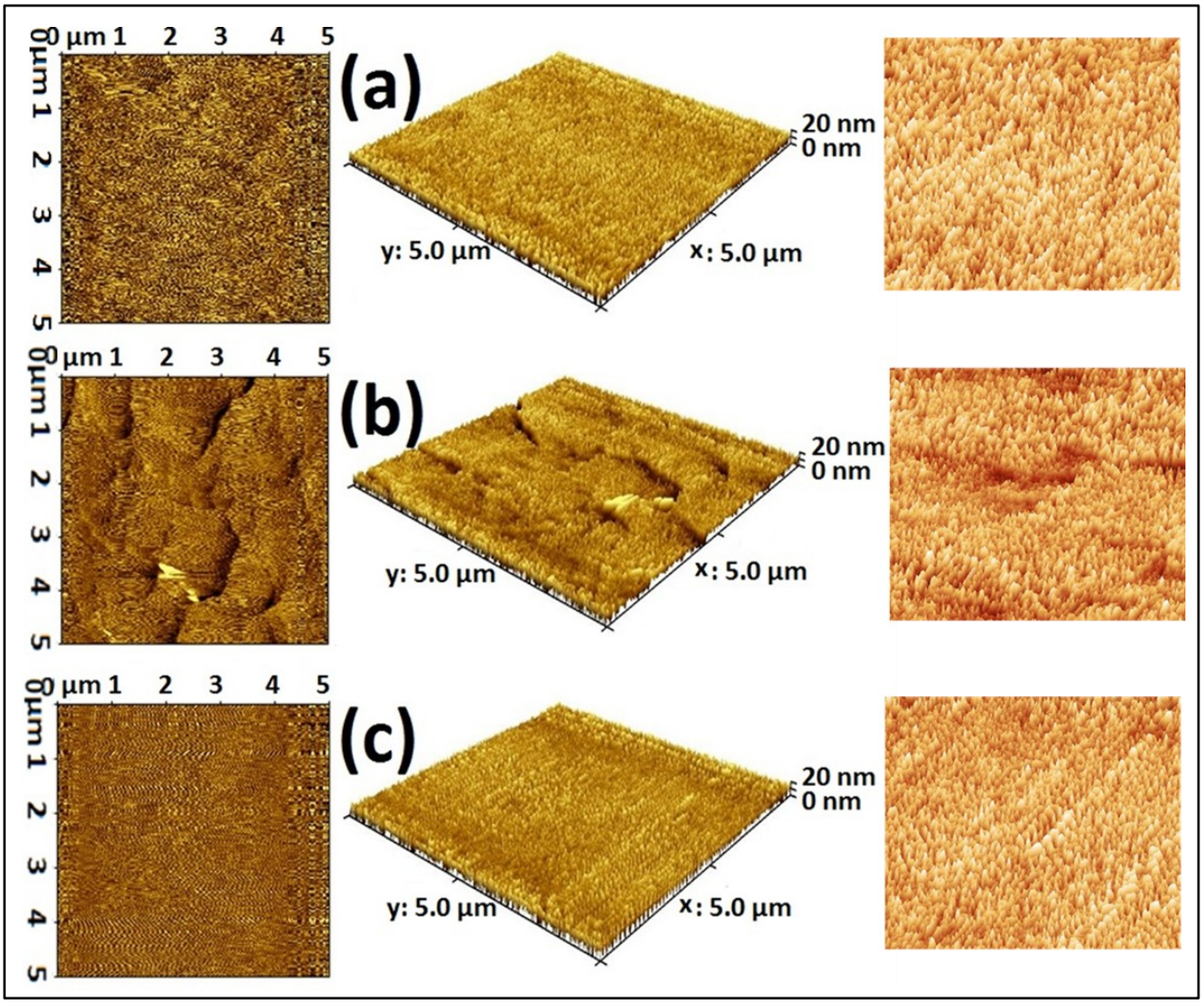


Figure III.7: 2D and 3D AFM images, along with a zoomed-in view of (**a**) ZnO, (**b**) 2% S-ZnO, and (**c**) 5% S-ZnO thin films.

III.3.4 Optical investigation

The optical features were examined by assessing the transmittance and refractive index spectra of both undoped ZnO and S-doped ZnO thin films throughout wavelengths ranging from 190 to 1100 nm, as depicted in Figure III. 7, along with the calculations presented in Table III. 3. The undoped ZnO sample exhibits a high transmittance within the visible spectrum, ranging from roughly 75% to 85% ((Figure III. 7(a)). It is apparent that the transmittance of S-doped ZnO thin films decreases with the addition of sulfur. The reduction in transmittance may result from i) lattice distortion, ii) defect formation, and iii) an increase in scattering centres due to the incorporation of S in ZnO thin films.

Moreover, the existence of interference fringes in the undoped ZnO thin film indicates the superior surface quality and optical uniformity of the final product. Figure III. 7(b) illustrates the refractive index (n) spectra of zinc oxide thin films comprising both zinc oxide and sulfur.

The sample thickness is denoted as e, the extinction coefficient a, k, the absorption coefficient as α, the reflectivity as R, and the wavelength as λ. The S-introduced samples demonstrated elevated refractive index values compared to ZnO thin films within the visible spectrum. The elevation of the n value may be associated with the alteration of the band gap and the concentration of charge carriers in the ZnO thin film. S doping lowers the optical band gap of ZnO. Furthermore, when utilised as a dopant, S may alter the concentration of free charge carriers, thus augmenting the refractive index of ZnO. Elevated refractive index values in the lower wavelength or higher energy spectrum result from the synchronisation of light photon frequencies with the plasma frequency [106]. This alignment results in resonance between the incident photon and electronic polarisation [107], facilitating electron interaction with an oscillating electric field [108], [109].

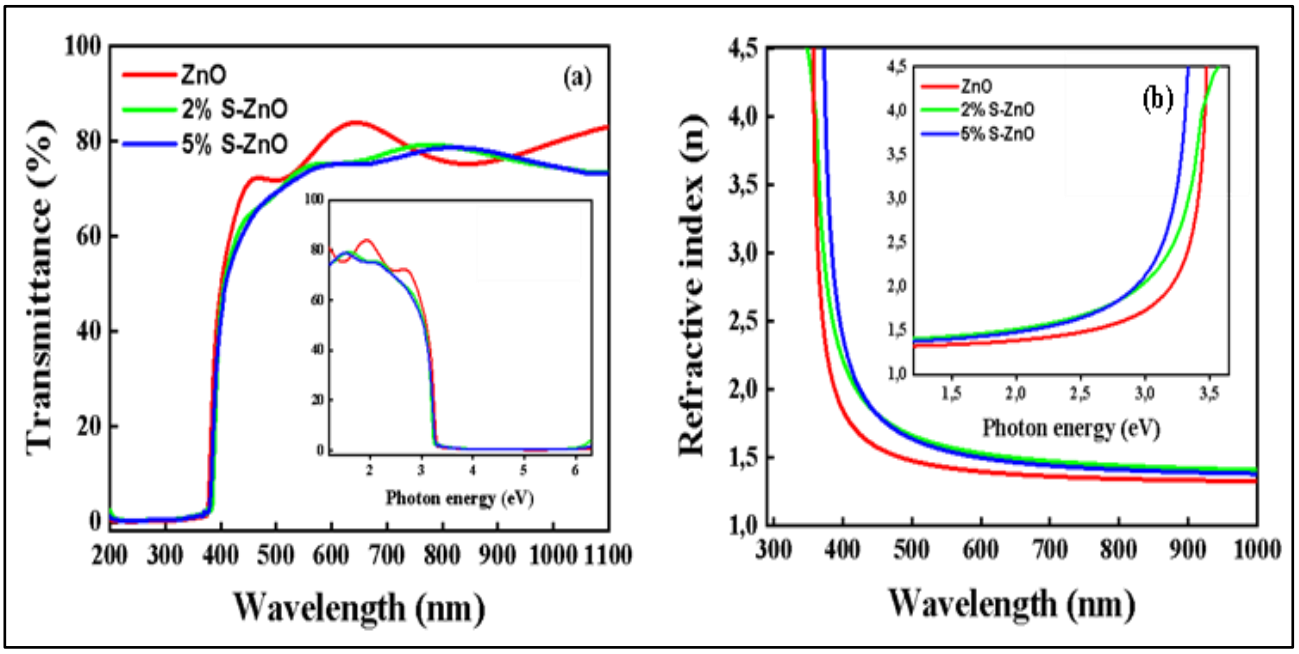


Figure III. 8: (**a**) Transmission and (**b**) refractive index curves as a function of wavelength for deposited layers.

Figure III. 8 depicts the fluctuation in Eg values for each sample. The bandgap energy (Eg) for undoped ZnO thin films is 3.27 eV; however, for samples with 2% and 5% sulfur doping, the Eg values are reduced to 3.23 eV and 3.25 eV, respectively. The decrease in the band gap may be attributed to alterations in crystal structures, atomic separations, grain dimensions, and the

morphology of applied coatings [110]. Rini and Rati synthesised S-ZnO nanorods by a seed-mediated hydrothermal process and noted a corresponding trend in band gap energy with elevated sulfur doping [111]. Dutta et al. [112] showed that the reduction in Eg is attributable to heightened tensile stress resulting from the introduction of contaminants. The coating's low band gap renders it a good choice for photocatalytic applications [26]. Nonetheless, additional experimental investigations are required to validate its complete appropriateness.

Table III.3: The gap energy, thickness, average refractive index (obtained from the curve), and refractive index measured via the Hervé-Vandamme model were examined using UV-visible spectroscopy measurements.

Samples	**ZnO**	**2% S-ZnO**	**5% S-ZnO**
Gap energy (eV)	3.27	3.23	3.25
Thickness (nm)	162	185	143
Mean refractive index (curve)	1.52	1.63	1.62
Refractive index (Herve-Vandamme)	2.255	2.263	2.257
Thickness (nm)	162	185	143

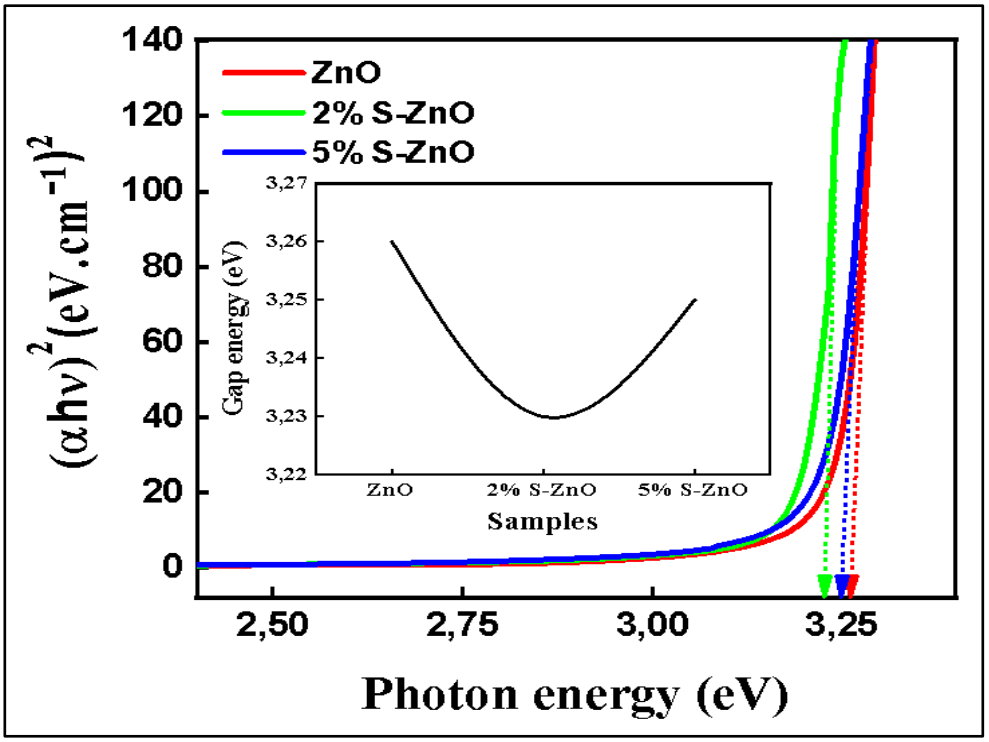


Figure III. 9: Energy gap measurements of the synthesized specimens.

III.4 Photocatalytic investigation

III.4.1 Experimental protocol

The photocatalytic efficacy of the produced thin films, specifically pure ZnO and S-doped ZnO, was evaluated using two distinct irradiation sources. The studies were performed under sunlight on a clear day in October 2024 in Khenchela, Algeria, from 11 am to 3 pm, with an average flux of around 480 mW/cm², and under UV light using a Philips G15T8 (15 W, λ = 251 nm) lamp placed 10 cm away. An aqueous solution of MB dye was employed to assess the photocatalytic responses of the samples under UV and solar light exposureThe methods utilized in every test, suitable for thin film samples, entailed positioning a 2 cm × 2 cm thin film in 10 ml of a pH~7.5, 2.5×10^{-5} $molL^{-1}$ MB solution. To achieve an adsorption-desorption equilibrium between the catalysts and the dye components, researchers stirred the catalyst-laden solutions in the dark for 30 minutes before exposing them to light. Thereafter, the glass beakers were subjected to direct sunshine and UV radiation. Every thirty minutes, 3 ml of the pollutant was extracted for solar exposure. The concentration of MB in the 500–750 nm wavelength range was quantified using a SpectroScan 80D UV–vis spectrophotometer. Following up to the

immediate measurement of absorbance A, the employed fluid (3 ml) was reintroduced to the original solution to maintain a uniform concentration of MB. The protocol for UV exposure at varying durations was comparable.

III.4.2 Photodegradation of MB

Following the analysis of After examining the structural, optical, and morphological properties of both undoped and doped ZnO films, we now focus on their photocatalytic activities under UV and natural sunlight illumination. Figure III. 9(a-f) illustrates the optical absorption spectra of the MB solution in the presence of photocatalysts for each light source. The principal absorption peak was seen at $\lambda max = 664$ nm, indicative of MB molecules.

- The spectra were taken at 15-minute intervals under UV illumination. Figure III. 9(a-c) depicts the reduction in intensity of the absorption peaks with time and under dark conditions, in the presence of thin coatings. Figure III. 10(a) illustrates the findings of MB photodegradation efficiency assessments relative to UV irradiation duration, indicating that S-doped ZnO thin films exhibited enhanced MB degradation efficiency in comparison to pure ZnO. The 2% S-doped ZnO thin film demonstrated excellent performance following 50 minutes. Table 3 presents the effectiveness values, demonstrating that dye degradation with the different photocatalysts is practically complete after 50 minutes of UV light exposure. ZnO doped with 2% sulfur attained the highest degrading efficiency among the photocatalysts, achieving 94.69% within 50 minutes.
  - Spectra were obtained at 30-minute intervals under sunshine. Figure III. 9(d-f) illustrates the diminution of absorption peak intensity with time and under dark conditions in the presence of thin coatings. The initial blue hue of the solution progressively diminishes until it turns colourless, signifying the degradation of the chromophoric structure of MB following sunlight exposure. Figure III. 10(b) presents the results of MB photodegradation effectiveness assessments as a function of sunlight exposure duration, indicating that S-doped ZnO thin films displayed a superior MB degradation rate compared to pristine ZnO. Table III.4 presents the efficacy values, demonstrating that dye degradation using the different photocatalysts is practically complete following 90 minutes of direct solar light exposure. ZnO doped with 2% sulfur exhibited a superior degradation rate of 96.71%, in contrast to 5% sulfur-doped ZnO at 89.58% and pristine ZnO at 76.32% after 90 minutes. Additionally, a reduced

- concentration of sulfur ions in the ZnO matrix markedly improved the breakdown efficiency of methylene blue. According to our findings, the optimal outcomes for MB degradation during UV and sunlight exposure were obtained utilising S-doped ZnO thin films fabricated by the sol-gel dip-coating technique. From the aforementioned statistics, we can deduce that the subsequent parameters enhance the distinctive photocatalytic effectiveness of S-doped ZnO:
- - XRD examination indicates that a decrease in crystallite size may augment the specific surface area of the film, hence improving catalytic activity, as previously reported. [113].
- SEM and AFM investigations demonstrate that increased surface areas enhance photocatalytic activity [114]. The specimen's heightened light absorption is chiefly attributable to its textured surface, characterised by numerous wrinkles that augment light dispersion, thus enhancing the efficacy of the photocatalytic process under UV and solar irradiation [115].
- From an optical standpoint, the reduced band gap energy from 3.26 eV to 3.23 eV facilitates the excitation of valence electrons by a larger quantity of lower-energy photons, whereas defect states induced by dopants impede electron and hole recombination, hence expediting the degradation process [116].
- The capacity of sulfur doping ions to capture electrons and/or holes on the surface, thereby inhibiting the recombination of the (e^-/h^+) pair, is an additional factor that enhances photocatalytic efficiency [117]. Table III. 5 displays the most recent findings on metal- and non-metal-doped ZnO nanoparticles employed in the photocatalytic destruction of organic contaminants.

Table III.4: Kinetic characteristics for each catalyst, including sulfur-doped ZnO.

Samples	Under UV light		Under sunlight	
	k (min^{-1})	D (%)	k (min^{-1})	D (%)
Pristine ZnO	0.0253	83.99	0.0136	76.32
2%S-ZnO	0.0476	94.69	0.0237	96.71
5%S-ZnO	0.0313	93.05	0.0220	89.58

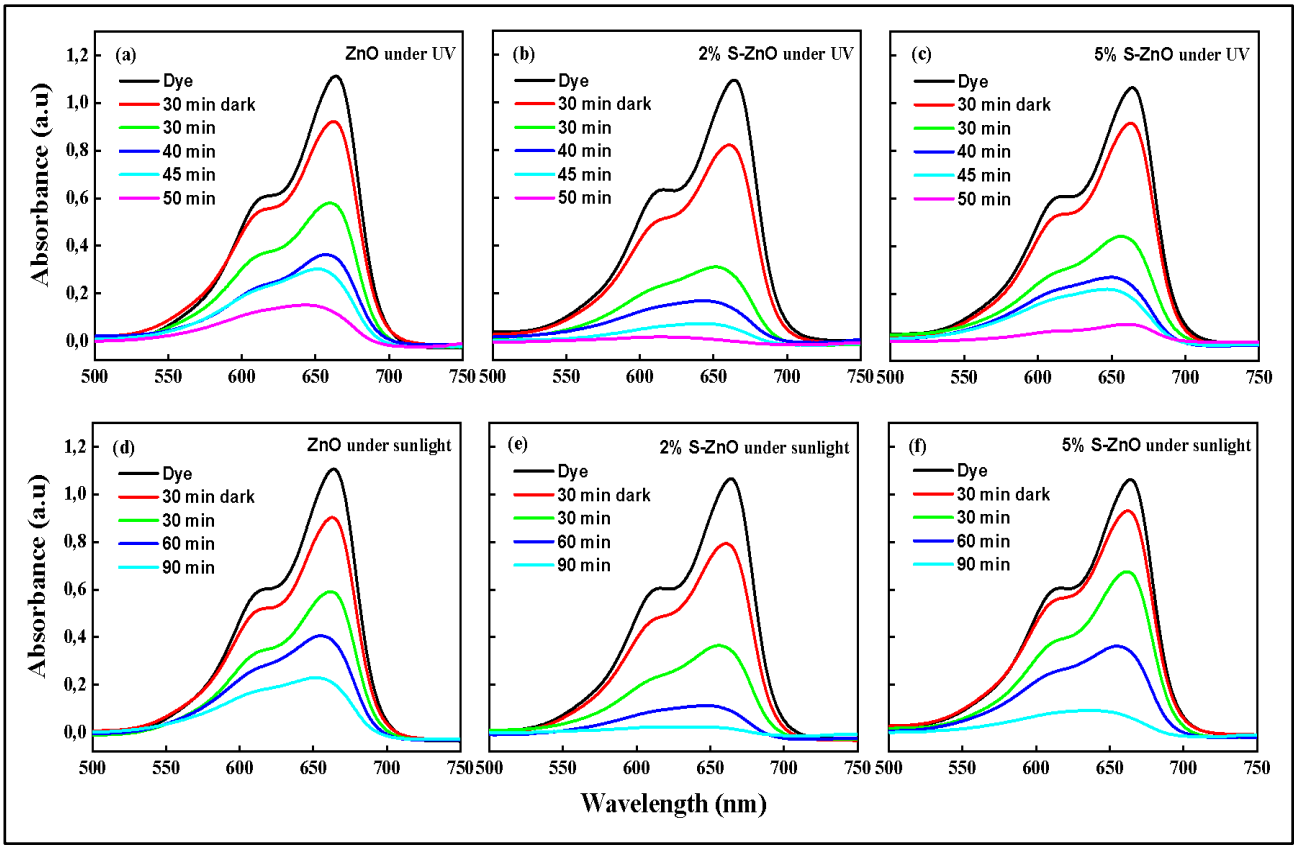


Figure III. 10: MB absorbance at various time intervals with pure ZnO and S-doped ZnO catalysts under UV and solar exposure.

Table III. 5: Recently published studies on metal and non-metal doped ZnO nanomaterials for the photocatalytic destruction of organic contaminants.

	Type of dopant	Element in %	Synthesis process	Pollutant/ Light source	Exposure time (min)	Dye degradation %	Ref.
5	**Alkaline earth metals**	Mg (2.5 wt %)	Sol–gel spin coating (thin film)	MB/ UV	150	72.15	[118]
		Mg	Lupinus albus Leaf Extract (NPs)	MB/ Sunlight	120	99.6	[119]
		Ba (5 wt %)	SILAR (thin film)	MB/ Sunlight	300	95.78	[120]
		Sr (5 wt %)	SILAR (thin film)	MB/ Sunlight	240	94.82	[121]
5	**Transition metals**	Cu (1 wt %)	ALD (thin film)	MB/ Sunlight	420	90	[122]
		Mn (5 wt %)	Sol–gel dip coating (thin film)	MB/ visible	120	33	[123]
		Cd (5 wt %)	SILAR (thin film)	MB/ UV	150	82.5	[124]
		V (10 wt %)	Spray pyrolysis (thin film)	MB/UV	150	68	[125]
5	**Noble metals**	Ag (5 wt %)	SILAR (thin film)	MB/ UV	180	75	[126]
		Ag (6 wt %)	Pulsed fs-LA (NPs)	MB/ visible	90	99.5	[127]
		Au (3 wt %)	Wet chemical (NPs)	RhB/ UV	10	100	[128]
		Pd (3 wt %)	Wet chemical (NPs)	MB/ Sunlight	150	48.5	[129]
5	**Rare Earth metals**	La (5 wt %)	Spray- pyrolysis (thin film)	MB/ UV	180	95	[130]
		Sm (5 wt %)	Sol–gel (NPs)	MB/ Sunlight	60	7.83	
		Nd (0.1 wt %)	Electrospinning–calcination (NPs)	MB/ Halogen lamp	120	100	[131]
		Gd (0.1 wt %)	Calcination (NPs)	AR18/ UV	40	98.28	[132]
5	**Non-metals**	C	Thermo-evolution (NPs)	MB/ UV–visible	150	67.2	[133]
		N	Thermo-evolution (NPs)	MB/ UV–visible	150	78.5	[133]
		S	Thermo-evolution (NPs)	MB/ UV–visible	150	81.4	[133]
		S (5 wt %)	Hydrothermal (thin film)	RhB/ Visible	150	92	[92]
		S (2 wt %)	Sol–gel dip coating (thin film)	MB/ UV	50	94.69	**This study**
		S (2 wt %)	Sol–gel dip coating (thin film)	MB/ Sunlight	90	96.71	**This study**

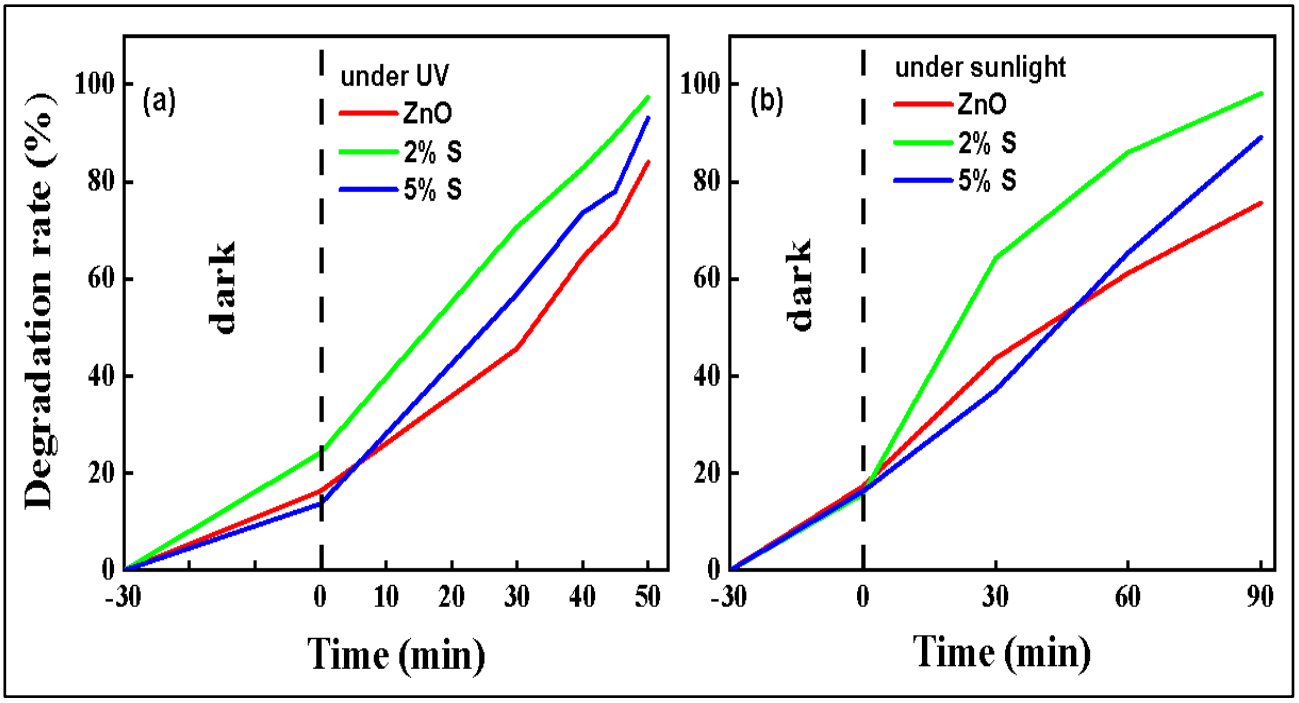


Figure III. 11: Degradation rate of MB over time for pure and S-doped ZnO under (**a**) UV radiation and (**b**) sunlight presence.

III.4.3 Photodegradation kinetic study

The rates of methylene blue degradation under light exposure were analysed using the Langmuir-Hinshelwood kinetic model, with samples serving as catalysts. Table 3 encapsulates the experimental data analysed with different catalysts, whereas Figure III. 11(a, b) depicts the outcomes derived from this equation. The results validate that MB photodegradation adheres to first-order kinetics, with S-doped ZnO films exhibiting superior photocatalytic activity relative to undoped ZnO. The 2% S-doped ZnO thin film exhibited the best photocatalytic efficiency, with rate constants of 0.0476 min^{-1} and 0.0237 min^{-1} under UV and sunlight, respectively, roughly twice that of undoped ZnO (0.0253 min^{-1} for UV and 0.0136 min^{-1} for sunlight).

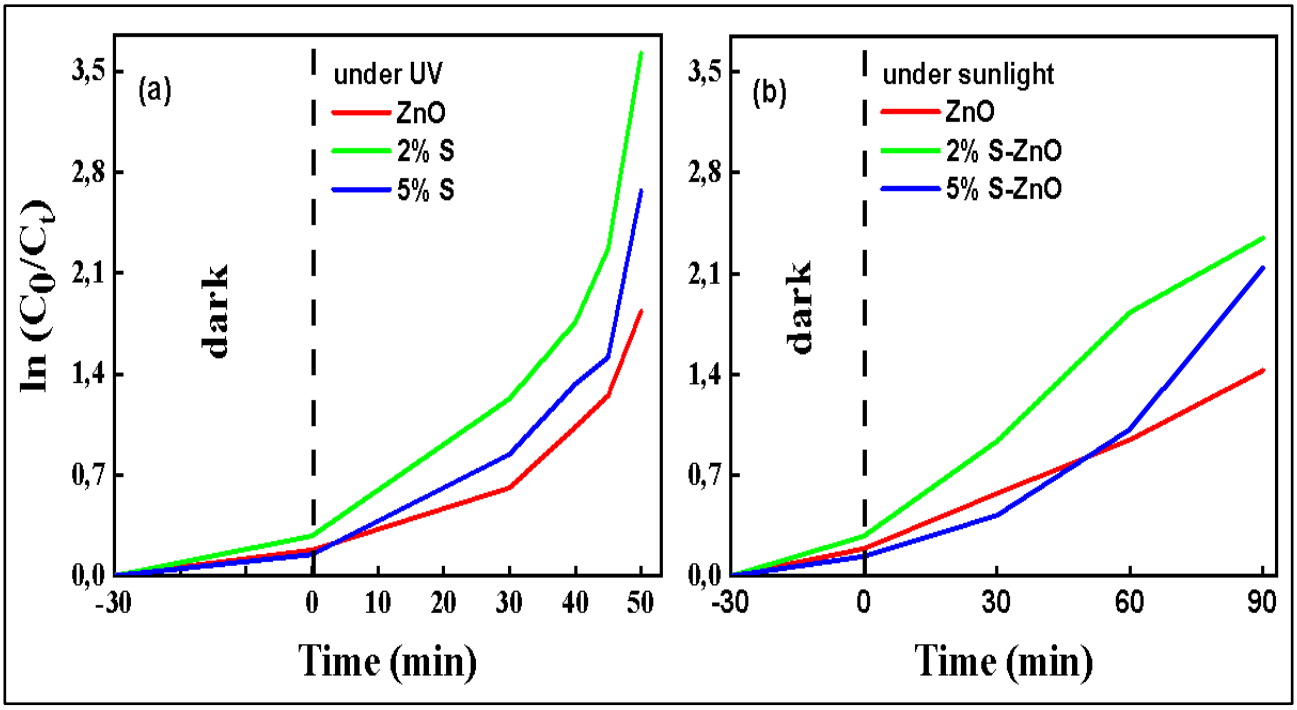


Figure III. 12: The reaction kinetics of methylene blue dye degradation for pure ZnO and sulfur-doped ZnO thin films under (a) ultraviolet and (b) solar light.

III.4.4 Mechanism of photodegradation behavior

The band edge potentials of the valence band (VB) and conduction band (CB) for ZnO and S-doped ZnO can be ascertained using a simple method. The band gap energies (Eg) of ZnO, 2% S-doped ZnO, and 5% S-doped ZnO films are 3.26 eV, 3.23 eV, and 3.25 eV, respectively. The conduction band (CB) and the valence band (VB) for ZnO and sulfur-doped ZnO can be determined using the Butler and Ginley equations, which are employed to ascertain the EVB and ECB of a semiconductor in its zero-charge state. The EVB and ECB values for the 2% S-doped ZnO thin film are 3.015 eV and -0.215 eV, respectively, whereas for pristine ZnO, they are 3.03 eV and -0.23 eV. The 5% S-doped ZnO thin film exhibits EVB and ECB values of 3.025 eV and -0.225 eV, respectively. The 2% S-doped ZnO demonstrates an elevated conduction band and valence band potential compared to pure ZnO, promoting the fast interaction of O_2 molecules with excited electrons to generate $\bullet O_2$ radicals. Thus, the S dopant efficiently captures excited electrons, diminishing charge carrier recombination. Figure III. 12 illustrates the photodegradation pathway of the S-doped ZnO thin film. In pure ZnO, the valence and conduction bands are delineated by the Fermi level. The introduction of sulfur impurities

results in the emergence of a new band beneath the Fermi level, ascribed to the production of free electrons. The impurity effect induces a shift in the Fermi level, thereby altering the band gap. Upon the impact of a sufficiently energetic photon on the photocatalytic material, a photoexcited electron (e^-) ascends from the valence band (VB) to the conduction band (CB), resulting in the formation of a hole (h^+) in the VB, so promoting the redox process. Hydroxyl radicals (•OH) are generated when this void interacts with H_2O molecules. In the S-doped ZnO photocatalyst, the impurity level is situated beneath the conduction band, potentially augmenting the separation rate of photogenerated charge carriers (e^-/h^+) by capturing the excited electron. The confined electron can then interact with an oxygen (O_2) molecule to generate superoxide anions ($•O_2^-$) radicals. These radicals are crucial to the breakdown of MB dyes, leading to the production of CO_2, H_2O, and other vital minerals [26].

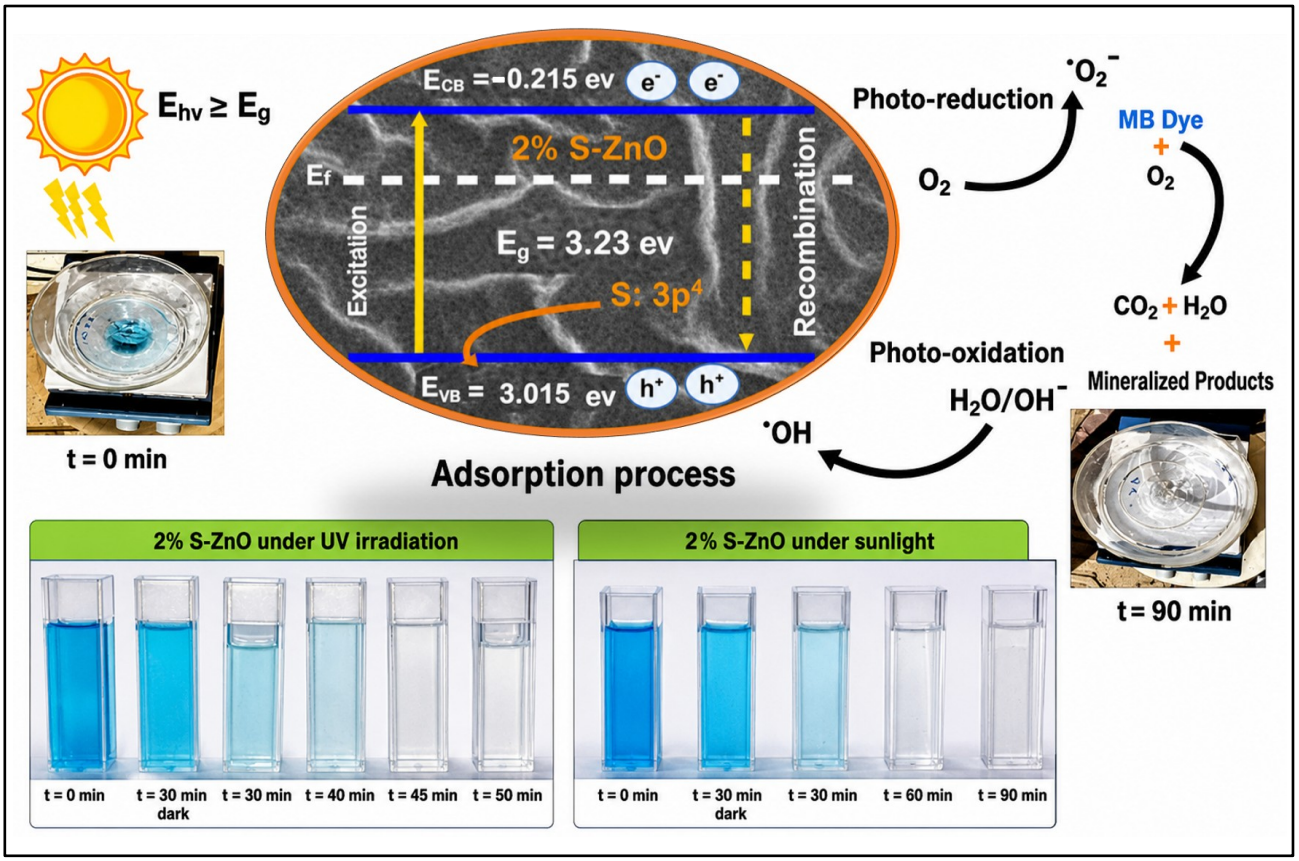


Figure III. 13: Mechanism of photocatalytic MB degradation in S-doped ZnO films.

III.4.5 Trapping test

Diverse scavengers, including ethylenediamine, tetraacetic acid, disodium salt (EDTA), L-ascorbic acid (AscA), isopropyl alcohol (IPA), and cupric nitrate (CN), were used in the trapping investigations of the primary reactive species. These scavengers were employed to capture holes (h^+), superoxide ($\bullet O_2^-$), hydroxyl radicals (•OH), and electrons (e), respectively. A 10 mL solution of MB was individually combined with 10^-3 M of each of the four specified scavengers. The principal active species in the photocatalytic process was identified by evaluating photocatalytic efficiency under similar conditions through studies conducted without scavengers. Figure III. 13(a, b) illustrates the photodegradation efficiency of MB solutions utilising 2% S-doped ZnO under UV and solar light, both with and without the presence of different scavengers. Figure III. 13(a) suggests that •OH and h^+ are the primary active species responsible for the degradation of MB dye under UV light, with the introduction of IPA and EDTA markedly diminishing the photocatalytic degradation efficiency of 2% S-doped ZnO. In contrast, •OH significantly contributes to the degradation of MB dye under sunlight exposure (Figure III. 13(b)).

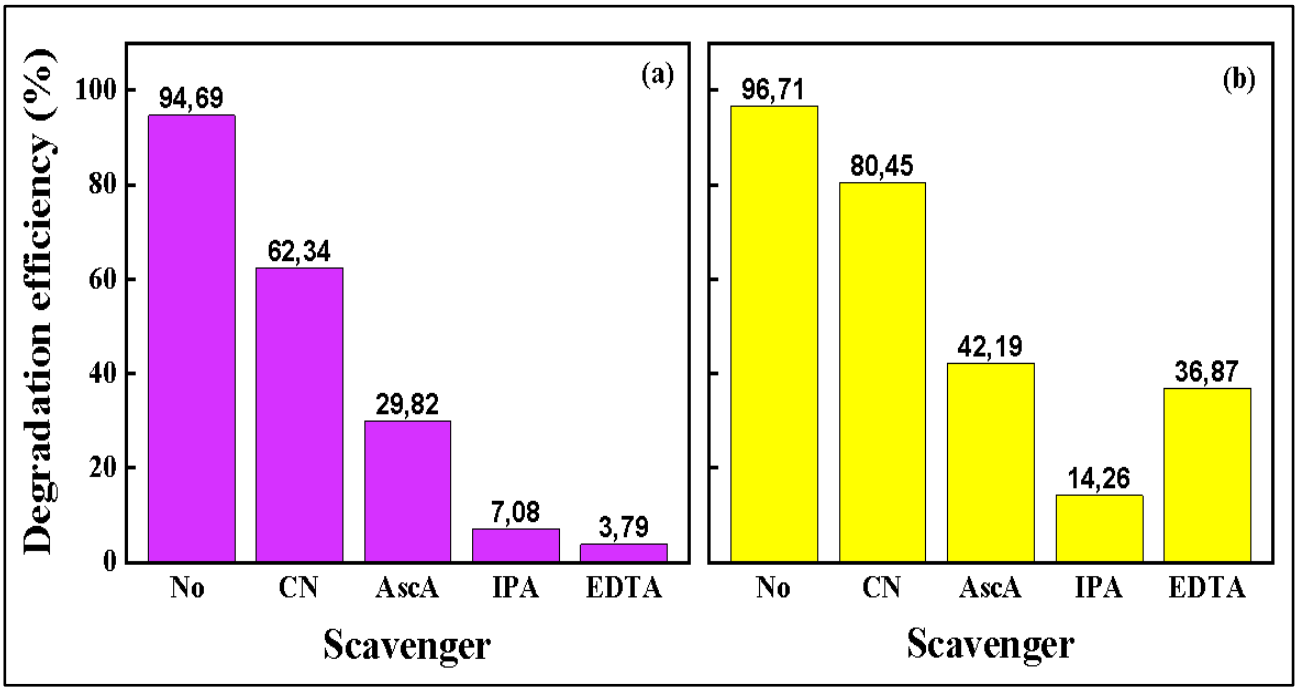


Figure III. 14: Effectiveness of MB degradation over the 2% S-ZnO catalyst in the absence and presence of various scavengers under (**a**) UV irradiation, and (**b**) sunlight illumination.

III.4.6 Reusability test

In photodegradation research, the stability and reusability of catalysts are crucial, since they enhance the cost-effectiveness of the process through catalyst recycling. This study examined the reusability of 2% S-doped ZnO, recognised as the most effective catalyst for MB degradation. Following initial use, the catalyst was subjected to a cleaning procedure with distilled water and subsequently dried prior to reuse. This protocol was uniformly implemented following each cycle. The degradation process was reevaluated in a new MB solution at a concentration of 2.5×10^{-5} M. The experiment was performed six times, using a 2% S-doped ZnO catalyst under both UV and solar illumination. The results, depicted in Figure III. 14(a-c) and Table III. 6, yield several significant insights.

i. A significant rise in degradation percentages was noted between the second and third cycles in comparison to the first cycle under UV light radiation. This is probable because, at the initial measurement, MB adsorption had not yet attained equilibrium and continued during irradiation.

ii. Figure III. 14(a) demonstrates that the degradation percentages of MB dye after four successive cycles of UV exposure exhibited a significant increase within a brief irradiation duration. This phenomenon can be ascribed to the augmented production of electron-hole pairs at elevated light intensity, hence improving photocatalytic activity and dye degradation efficacy.

iii. The degradation efficiency of MB dye after six consecutive cycles of sunshine exposure exhibited a minor decline from 96.71% to 96.04% (Figure III. 14(b)), demonstrating the effective recycling capability of 2% S-doped ZnO under sunshine.

iv. The XRD patterns of the 2% S-doped ZnO film, prior to and following the sixth cycle of exposure to both UV and direct sunlight, as illustrated in Figure III. 14(c), exhibited no substantial variations, other than a decrease in peak intensity. This indicates a reduction in crystallinity and a drop in film thickness, presumably resulting from photo-corrosion, wherein ZnO at the interface dissociates into Zn^{2+} and O^{2-} ions. The ions dissolve in the solution upon exiting the film, leading to diminished layer thickness and lower photoactivity degradation [134], [135].

In conclusion, these results emphasise the catalyst's strong reactivity, exceptional stability, and reproducibility, showcasing its significant potential for environmental remediation, especially under solar irradiation.

Table III.6: Recycling of the catalyst, reaction duration, and degradation effectiveness (D) of methylene blue for 2% S-doped ZnO.

No. of cycles	Under UV light		Under sunlight	
	D (%)	Time (min)	D (%)	Time (min)
1	94.69	50	96.71	90
2	97.64	30	96.79	90
3	96.21	30	96.50	90
4	89.98	30	96.63	90
5	74.52	50	96.25	90
6	58.46	50	96.04	90

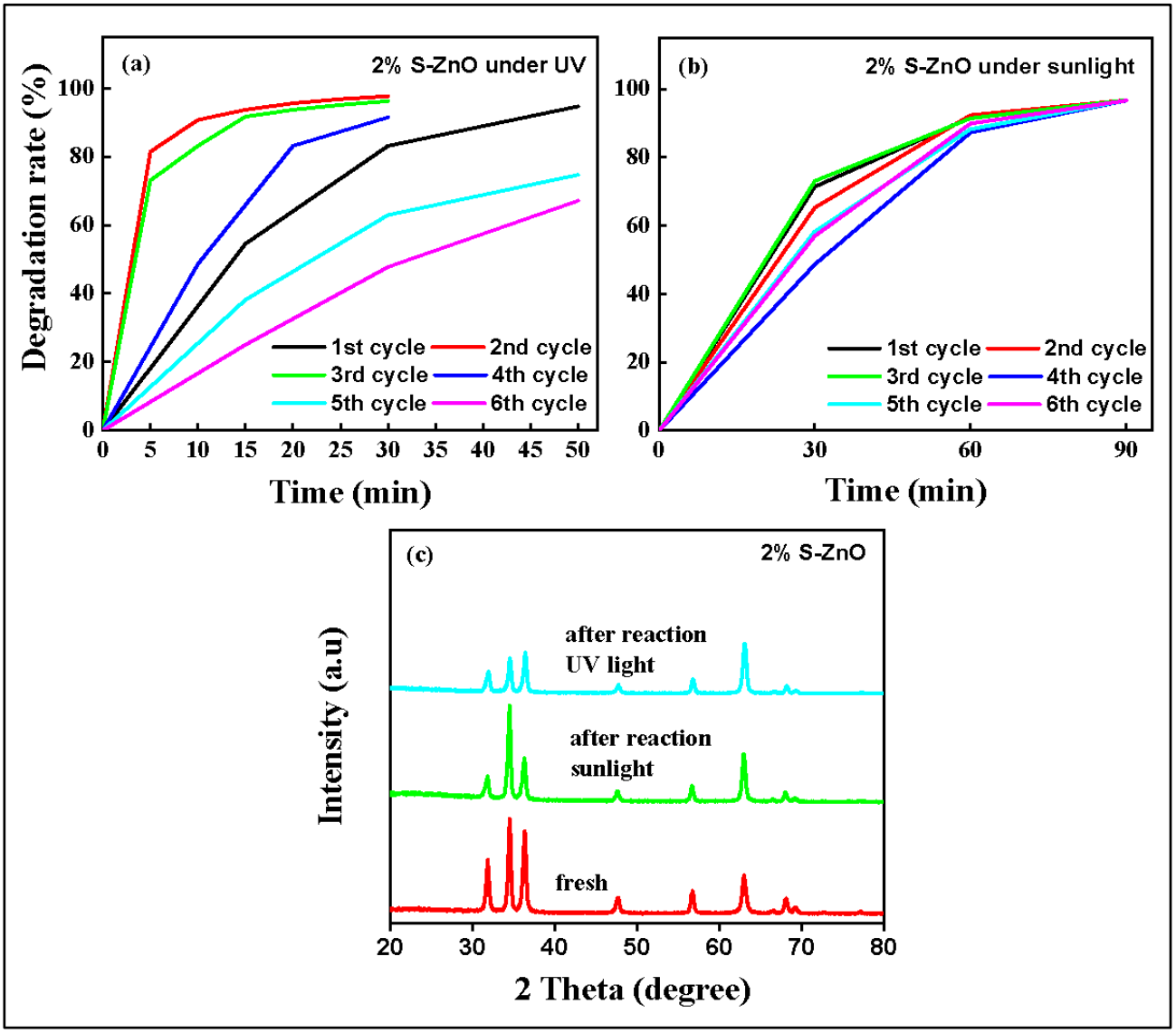


Figure III. 15: Evaluation of the reusability of the 2% S-ZnO thin film for MB dye through photocatalytic testing under (**a**) UV rays, (**b**) sunlight exposure, and (**c**) XRD analysis following the sixth cycle of photocatalytic studies.

III.5 Photodetection investigation

The pure and cadmium-doped ZnO thin film samples were analysed for photocurrent under dark conditions and UV illumination with a power intensity of 90 mW/cm² at a wavelength of 365 nm. The sample had an area of 1.5 x 2 cm², and the corresponding photocurrent was documented using a source meter connected via copper electrodes, as shown in the schematic design Figure III. 15, and the related data were illustrated in an I-V graph, as depicted in Figure III. 16. The degree to which a photodetector's electrical output fluctuates in response to light exposure is a measure of its sensitivity. The dark current of the 5 V photodetector device with

pure ZnO was 5.82 nA, 6.38 nA for 2% S-ZnO, and 6.02 nA for 5% S-ZnO at room temperature. Under UV light, this improved to 6.73 nA, 8.46 nA, and 7.93 nA, respectively. The main photodetection characteristics of the produced S-doped ZnO photodetector, including sensitivity (S), responsivity (R), and detectivity (D), were evaluated based on the observed I-V curve. Table III. 7 displays the result values for each sample.

The measurement results indicate that ZnO devices doped with 0%, 2% and 5% sulfur have respective sensitivities of 1.16, 1.33 and 1.32. The responsivity of a photodetector is a key parameter defining its ability to convert an incident optical signal into an electrical response. The measured responsivity value for pure ZnO is 27.11 nA/W; it increases to 31.32 nA/W for a 2% sulfur doping before decreasing to 29.39 nA/W for a 5% doping. Detectivity, which reflects the photodetector's ability to detect low-intensity optical signals. The measured values are 10.88×10^5, 12.01×10^5 and 11.6×10^5 Jones for pure ZnO, ZnO doped with 2% sulfur and ZnO doped with 5% sulfur, respectively (Table III. 7).

The sample doped with 2% sulfur-doped ZnO exhibits maximum detectivity, reactivity, and sensitivity. This improvement is attributed to more efficient generation and collection of charge carriers under UV illumination. This parameter increases with increased free electron concentration, which is associated with a greater presence of ionised oxygen vacancies. Sulfur doping improves device performance by reducing resistivity and increasing charge carrier density. However, excessive doping introduces more recombination centers, which promote electron-hole recombination and lead to the degradation of the device's optoelectronic performance [70], [136], [137], [138], [139].

Table III.7: Photocurrent performance of pure and sulfur-doped ZnO thin films measured at 5 volts.

Samples S (%)	**S**	**R (nA /W)**	**D^*10^5 (Jones)**
0%	1.16	27.11	10.88
2%	1.33	31.32	12.01
5%	1.32	29.39	11.6

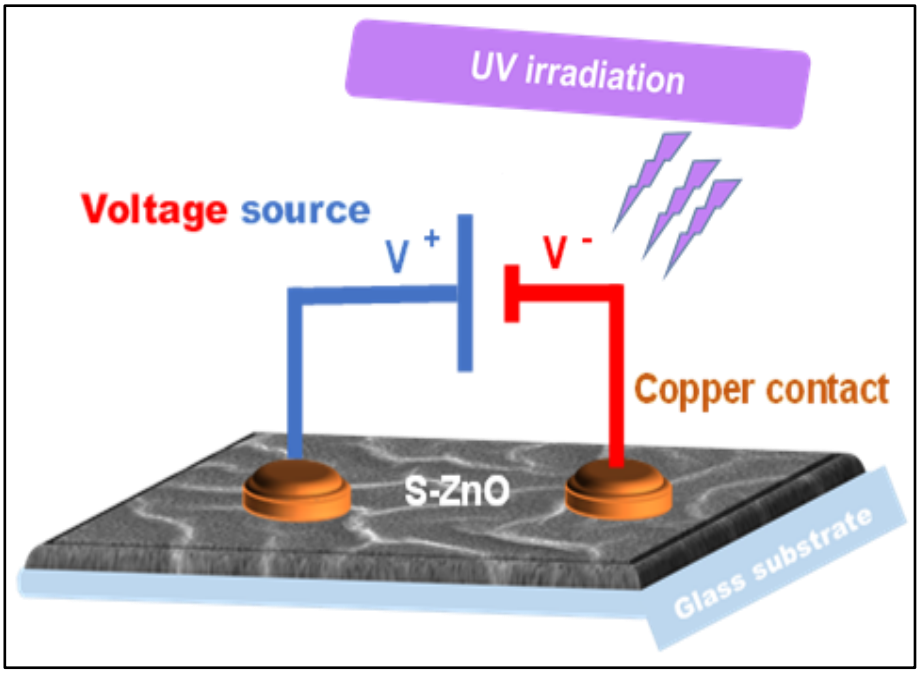


Figure III. 16: Schematic for a fabricated photodetector device.

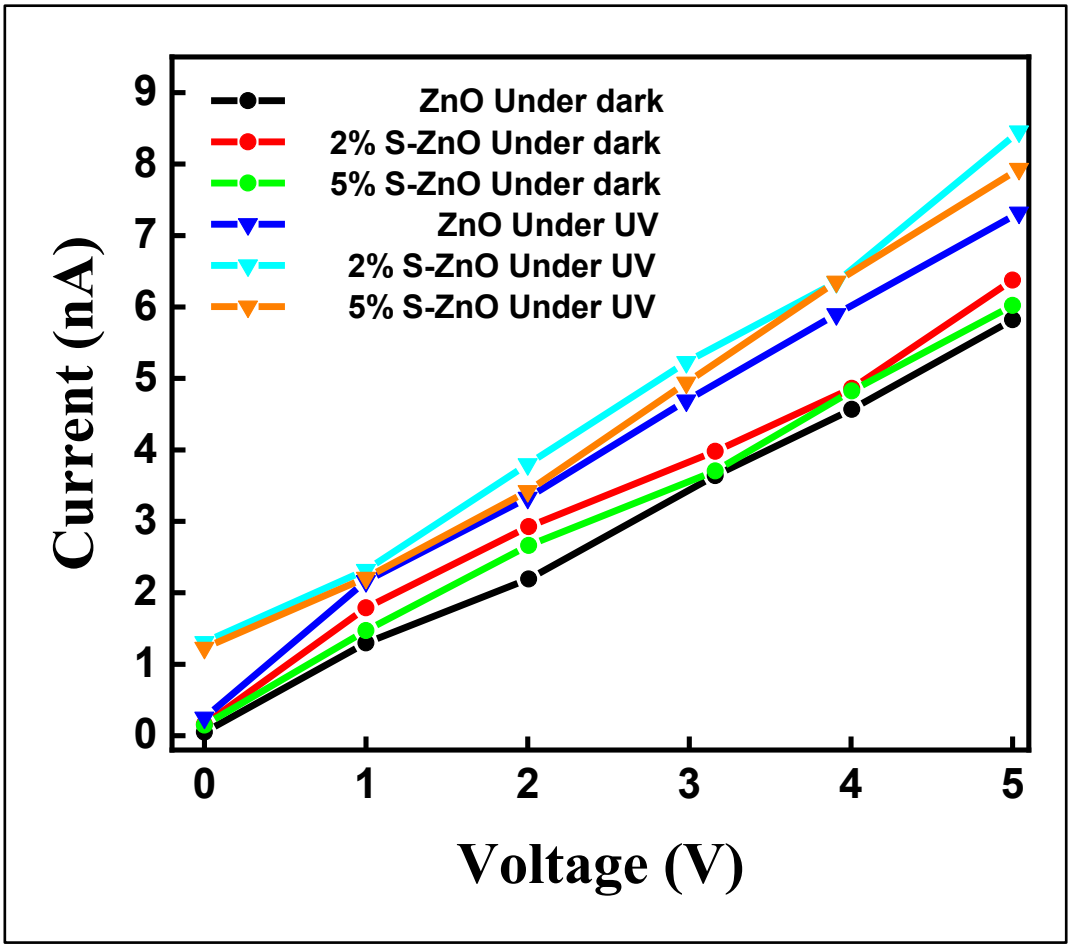


Figure III.17: Current measured as a function of voltage in darkness mode and under UV light for pure ZnO, 2% S-doped ZnO, and 5% S-doped ZnO thin films.

III. 6 Conclusion

This study involved the deposition of pure and sulfur-doped ZnO thin films onto glass substrates utilising the dip-coating process. The synthesised materials were characterised using multiple techniques, including X-ray diffraction (XRD), energy-dispersive spectroscopy (EDS), scanning electron microscopy (SEM), atomic force microscopy (AFM), and ultraviolet-visible spectroscopy (UV-VIS). The implanted thin films were used as photocatalysts for the decomposition of methylene blue under ultraviolet light and sunlight. S-doped ZnO films demonstrated enhanced photocatalytic activity relative to virgin ZnO. The 2% S-doped ZnO sample exhibited the best photocatalytic performance under UV and sunlight exposure, achieving efficiencies of 94.69% after 50 minutes and 96.71% after 90 minutes, respectively. The studies on trapping active species confirmed that H^+ and •OH are crucial for the photocatalytic breakdown of MB. Furthermore, reusability assessments confirmed the stability and reliability of the film following six successive cycles. Additional examination of this thin

film is necessary, as it possesses potential as an environmentally benign photocatalyst for a wider array of pollutants; consequently, we propose that sulfur doping is a viable technique to augment the photocatalytic efficacy of ZnO thin films for environmental applications. The UV photodetection performance of ZnO thin films was also enhanced by S doping, and the optimal device with 2 wt% of S-doping, achieved remarkable sensitivity, responsivity, and detectivity values of 1.33, 31.32 nAW^{-1}, and 12.01×10^{5} Jones, respectively.

Chapter IV Synthesis and Characterisations of pristine ZnO and cadmium-modified Zinc oxide thin layers for optoelectronic and environmental applications

IV.1 Introduction

In this part, pure ZnO and cadmium-doped ZnO thin films were developed onto a glass substrate using the gel-sol technique and dip coating process. Additionally, we looked at the effects of cadmium doping on the ZnO films' structural, surface morphological, topographical, and optical properties, as well as their possible uses in photocatalysis under sunlight light irradiation and UV light detection.

IV.2 Thin film manufacturing

IV.2.1 Preparing the substrate

The films were placed on common, cost-effective, and manageable glass slides (25.0 × 37.6 mm^2) and 1–2 mm in thickness. Prior to deposition, the glass substrates underwent ultrasonic cleaning in acetone, distilled water, methanol, distilled water, and ethanol for 15 minutes in each solvent. Substrates were kept in ethanol post-cleaning and subsequently dried immediately prior to use.

IV.2.2 Chemical and materials

The study utilised multiple chemicals, including zinc acetate dihydrate [Zn $(CH3OO)_2$, $2H_2O$, 99 % purity, MERCK], ethanol [C_2H_6O, 99.8 % purity, VWR], methanol [CH_4O, ≥ 98 % purity, VWR], acetone [C_3H_6O, ≥ 99.5 % purity, Sigma-Aldrich], Cadmium chloride hemi(pentahydrate) [$CdCl_2$, $2.5H_2O$, ≥ 98 % purity, MERCK], monoethanolamine (MEA) [C2H7NO, 99 % purity, Sigma-Aldrich], methylene blue dihydrate (MB) [$C_{16}H_{18}ClN3S$, $2H_2O$, 99 % purity, Sigma-Aldrich]. The compounds employed in radical scavenger research, such as isopropanol (IPA) [C_3H_8O, ≥ 99.5 % purity, Sigma-Aldrich], ethylenediaminetetraacetic acid dihydrate (EDTA) [$C_{10}H_{16}N_2O8$, $2H_2O$ ≥ 98 % purity, Biochem], copper (II) nitrate trihydrate (CN) [Cu $(NO_3)_2$,$3H_2O$, > 99 % purity, MERCK], L-ascorbic acid (AscA) [$C_6H_8O_6$), ≥ 99.7 % purity, MERCK]. Thin films were fabricated at room temperature using a dip coating device (HOL-MARC HO-TH-02B).

IV.2.3 Synthesis of thin films

The procedures for sample preparation use dip-coating and sol-gel methodologies. Glass substrates were coated with both undoped and Cd-doped ZnO thin films. Initially, 40 mL of ethanol was mixed with 0.4 mL of MEA to formulate a 0.4 M solution of zinc acetate. Subsequent to 30 minutes of agitation at room temperature, the solution was elevated to 50 °C

for two hours till achieving transparency. To produce the doped films, 3wt%, 7wt%, and 10wt% of cadmium chloride were incorporated into the prepared precursor solutions as the cadmium source. Secondly, prior to applying the prepared solutions for dip coating, we allow them to rest at room temperature for 72 hours. The aged solution was applied to cleaned glass substrates at a dip speed of 80 mm/min to attain the necessary thickness. The samples were subsequently warmed at 400°C for 10 minutes to eliminate any solvents. This procedure was executed fifteen times. The technique concluded after the deposition of 15 layers, followed by a two-hour annealing at 500 °C.

IV.3 Results and discussion

IV.3.1 Structural investigation

The crystalline characteristics of the produced samples were examined by XRD analysis. Figure IV.1 illustrates the XRD patterns of both pure and cadmium-doped ZnO thin films. Within the diffraction angle range of 20° to 80°. All diffraction peaks of both undoped and doped ZnO samples are attributed to the wurtzite hexagonal structure (standard ICDD card: 00-036-1451, space group P63mc, a = b ≠ c) [32]. The diffractions from the (002) planes are highly intense, indicating that the growth direction of all samples of thin films is orientated along the c-axis [140]. The diffraction intensities of the doped sample are weaker compared to the undoped ZnO, indicating that Cd doping can somewhat hinder the crystallinity of ZnO [141]. Further the positions of XRD peaks in the Cd-doped ZnO films exhibit a small shift towards lower diffraction angles compared to pure ZnO. This may result from the introduction of dopants into the ZnO lattice, as the ionic radius of Cd^{2+} (95 pm) differs from that of Zn^{2+} (74 pm) [71]. Consequently, the diffraction patterns indicate that Cd^{2+} ions methodically replace Zn^{2+} ions or insert into the ZnO nanocrystal while maintaining the wurtzite structure. The insertion condition at Lattice Wurtzite is $r^{+}/R^{-} \geq \sqrt{\frac{3}{2}} - 1$ [(r_{Cd2+}/RO^{2-} = 0.679 and r_{Zn2+}/RO^{2-} = 0.529), r_{Zn2+}(74 pm), r_{Cd2+}(95 pm), and RO^{2-}(140 Pm)], then the Pauling electronegativity of cadmium bigger than zinc (X_{Cd} = 1.69, and X_{Zn} = 1.65). Furthermore, the absence of secondary phase peaks in the diffraction patterns indicates that the synthesized samples are of high purity and consist of a single phase. The (002) plane, being the most significant peak, is selected for additional investigation and computations. Microstructural characteristics, including, lattice parameters (a = b and c), volume of the unit cell (V_{cell}), Atomic Packing Factor (APF), and crystal lattice distortion degree (R) are presented in Table IV. 1(a), and crystallite size (D), dislocation density

(δ), micro-strain (ε), bond length (l), Bond angles α and β are presented in in Table IV. 1(b). The crystal lattice distortion degree (R) increases with variations in cadmium doping, as illustrated in Table IV. 1(b). The increase in (R) can be attributed either to the substitution of Zn^{2+} ions by Cd^{2+} ions or to the incorporation of cadmium into the tetrahedral or octahedral sites of the crystal lattice. The hexagonal structure has 12 tetrahedral sites and 6 octahedral sites. In the wurtzite structure, which is initially hexagonal, oxygen ions occupy fifty percent of the tetrahedral sites, while zinc ions occupy the hexagonal sites. The Atomic Packing Factor (APF) is a crucial metric for measuring the density of atomic packing in a crystal lattice. It is defined as the ratio of the entire atomic volume within a unit cell to the overall volume of the unit cell. The APF offers significant information into the material's density and structure [142]. Atomic Packing Factor (APF) value after mixing ZnO with cadmium increased to around 0.15% compared to pure ZnO due to the incorporation of cadmium ions into the crystal structure, evidenced by the expansion of the unit cell volume. In the ideal wurtzite configuration, the Atomic Packing Factor (APF) for a hexagonal close-packed (HCP) structure is 0.74. This signifies that atom occupy 74% of the volume within a hexagonal close-packed (HCP) unit cell, leaving 26% of the volume vacant of particles [143]. The Atomic Packing Factor (APF) of 3% Cd-doped ZnO is 75.578%. This signifies that atoms occupy 75.578% of the volume within a unit cell, whereas 24.422% of the volume is unoccupied (devoid of particles). Figure IV. 1.(b) demonstrates that the integration of Cd into ZnO thin films results in a decrease followed by an increase in the crystallite size of the produced thin films. Table IV. 1(b) illustrates the variation in crystallite size of the synthesised nanostructured thin films based on the computed data. The measured reduction in crystallite size of the synthesised nanostructured ZnO thin films upon the incorporation of 3 wt % Cd, from approximately 42.23 nm to 37.32 nm, was followed by a rise with the addition of 7 wt % and 10 wt % Cd, resulting in sizes of around 39.12 nm and 42.076 nm, respectively. Studies indicate that doping ZnO with Cd alters crystallite size, exhibiting both a decrease and an increase following the injection of cadmium [144], [145]. The ZnO lattice was doped with low-valent cadmium, indicating that the dopants impede crystallite formation. The research demonstrates that dopants induce lattice distortions and defects, resulting in heightened internal stresses, as indicated by the increase in microstrains with doping. The decrease in strain caused the increase in crystallite size of thin films [31], [95]. The positive micro strain values depicted in Table IV. 1(a) signify tensile strain ε, which correlates with the existence of impurities or defects, ion exchanges involving atoms of varying ionic radii, and discrepancies in the lattice parameters, and volume of the unit cell [31], [93].

Table IV.1(b) presents the established Zn–O bond length measurements. The reduction in the Zn–O bond length in Cd-doped ZnO is attributed to the ionic radii of O^{2-} (140 pm) and Zn^{2+} (74 pm), influenced by the electronegativity of the constituent atoms [31]. Cadmium (Cd^{2+}), the dopant, possesses a greater ionic radius (95 pm) compared to zinc ($Zn^{2+),}$ which measures 74 pm. Zinc, with a Pauling electronegativity of 1.69, is more electronegative than Zinc, which has a value of 1.65. The disparity in electronegativity is especially noticeable when contrasting ZnO with CdO. Consequently, Cd^{2+} ions demonstrate a greater affinity for O^{2-} ions compared to Zn^{2+} ions. Longer bond lengths generally result from a smaller difference in electronegativity between elements and a larger ionic radius; therefore, the Cd–Zn bond length is greater than the O–Zn bond length because the ionic radius of Zn^{2+} (74 pm) is less than that of Cd^{2+} (95 pm). [31], [95], [96]. Table IV. 1(b) presents the values of angles α and β for the Cd-doped ZnO thin films, which remain largely consistent, exhibiting only minor fluctuations attributable to the greater size of the cadmium ion relative to the zinc ion [71], [146].

Finally, these results confirm that the changes in structural properties definitively demonstrate the integration of the additive into the crystal lattice of zinc oxide.

Table IV. 1(a): Structural parameters derived from XRD data for all thin films Cd-ZnO deposited using the dip coating technique.

samples	**B_{002} (rad)**	**d_{100} (nm)**	**d_{002} (nm)**	**$2\theta_{100}$ (°)**	**$2\theta_{002}$ (°)**	**a=b, c (A°)**	**V_{celle} $(A°)^3$**
Pure ZnO	0.206	0.2815	0.2604	31.75	34.40	a=3.250 c=5.208	47.65
3% Cd-ZnO	0.233	0.2825	0.2609	31.64	34.33	a= 3.262 c=5.218	48.071
7% Cd-ZnO	0.222	0.2824	0.261	31.65	34.32	a=3.260 c= 5.22	48.052
10% Cd-ZnO	0.189	0.2823	0.2611	31.66	34.31	a=3.259 c= 5.221	48.035

Table IV. 1(b): Structural parameters derived from Cd-ZnO XRD data for all thin films deposited using the dip coating technique.

Samples	APF (%)	R	D (nm)	ε×10⁻³	d×10⁻⁴ lins /nm⁻²	l (nm)	α, β (°)
Pure ZnO	75.471	1.0192	42.23	2. 898	5. 61	1. 9782	α= 108.44 β =110.48
3% Cd-ZnO	75.578	1.0207	37.32	3. 287	7. 184	1. 9841	α= 108.36 β =110.56
7% Cd-ZnO	75.532	1.02	39.12	3. 135	6. 534	1. 9838	α= 108.40 β =110.52
10% Cd-ZnO	75.489	1.0195	42.076	2. 916	5. 65	1. 9835	α= 108.43 β =110.49

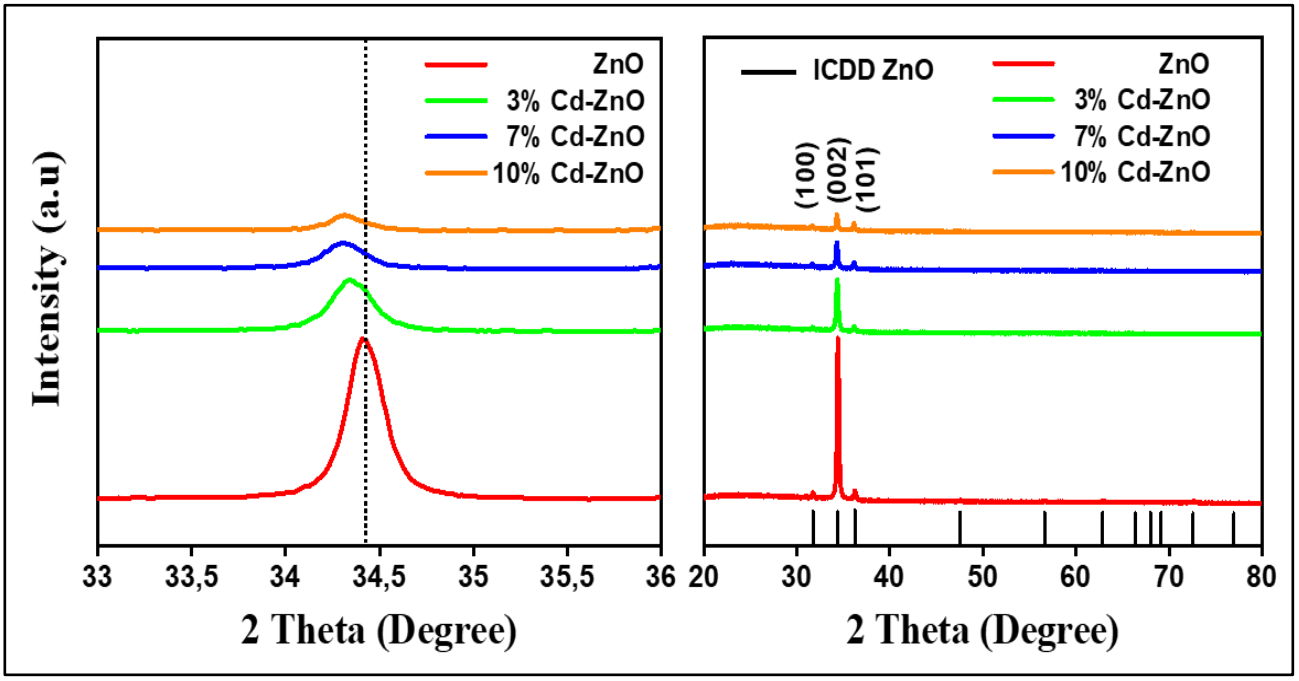


Figure IV.1: (**a**) XRD intense diffraction peaks (002), and (**b**) XRD patterns Cd-ZnO thin films of samples.

IV.3.2 Morphological analysis FESEM

Environmental scanning electron microscopy (ESEM) investigation was employed to evaluate the surface morphologies of each of the pure and cadmium-modified ZnO thin films, as depicted in Figure IV. 2(a-d). All the thin films exhibited a structure devoid of cracks. Grain size and

porosity were calculated using ImageJ software (Table IV.2). FESEM images highlighted significant changes in the surface morphology of sample Figure IV. 2(b), while samples Figure IV. 2(a,c,d) retained a similar external appearance, with differences in porosity and particle size**.** Figure IV. 2(a, c,d) shows SEM-FEG images of pure ZnO, 7 wt% ZnO-Cd and 10 wt% ZnO-Cd, respectively, which show an irregular and heterogeneous surface with unevenly distributed spherical particles, with average grain sizes of 74.618, 43.531 and 55.42 nm and porosity of 26.178%, 15.113% and 18.364%, respectively. In contrast, the thin zinc oxide film doped with 3 wt% cadmium (Figure IV. 2(b)) exhibits a granular structure characterised by micropores. These films have smooth, uniform shapes and sizes, with small spherical particles and high density, resulting in an average particle size of 32.005 nm and a porosity of 8.116%. In materials science, low porosity is a critical attribute signifying the existence of voids or microscopic cavities within a material. It is crucial in numerous scientific and technological domains, since it affects the characteristics and behavior of materials [147]. A high atomic packing factor signifies that atom in the crystal structure are closely packed, resulting in increased overall material density. Crystals possessing elevated APF values typically demonstrate improved mechanical strength and less porosity [142]. A decrease in porosity indicates a reduction in void volume and an increase in density; therefore, the atomic packing factor (APF) has an inverse effect on porosity. The X-ray analysis indicates that the APF values are elevated in Cd-doped ZnO films compared to pure ZnO, while the FESEM reveals a decrease in porosity in Cd-doped ZnO films relative to pure ZnO. This is attributed to a reduction in grain size, as observed through FESEM, and crystallite size, as determined by XRD analysis, resulting from the incorporation of Cd atoms into the ZnO lattice [126].

Table IV.2: The Grain size, and porosity of the samples were calculated using ImageJ software based on FESEM images.

Samples	**ZnO**	**3% Cd-ZnO**	**7% Cd-ZnO**	**10% Cd-ZnO**
Grain size (nm)	74.618	32.005	43.531	55.420
Porosity (%)	26.178	8.116	15.113	18.364

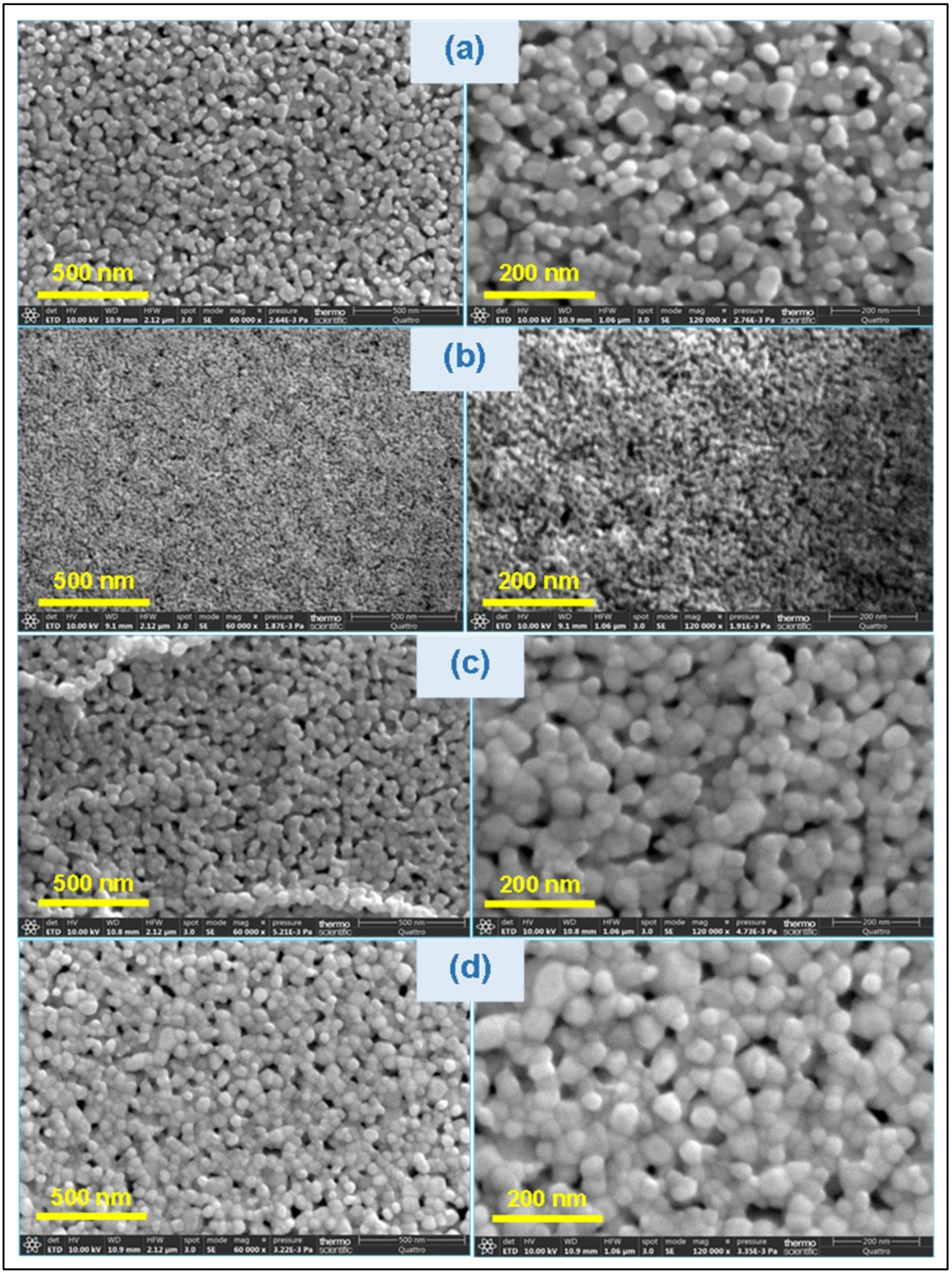


Figure IV.2: SEM images of (**a**) ZnO, (**b**) 3% Cd-ZnO, (**c**) 7% Cd-ZnO, (**d**), 10% Cd-ZnO thin films.

Figure IV. 3 shows EDAX spectra of samples at the following concentrations: (a) 0 wt.% Cd, (b) 3 wt.% Cd, (c) 7 wt.% Cd, and (d) 10 wt.% Cd-doped ZnO thin films at ambient temperature. EDAX patterns in Figure IV.3 (a-d) for pure and Cd-doped ZnO revealed the exclusive presence of Zn, O, and Cd in the film, hence confirming the purity of the dip-coating-deposited film; these results illustrate the integration of Cd into the ZnO wurtzite structure. The atomic percentages of cadmium before activation do not align with the elemental composition seen after activation, as demonstrated in Figure IV. 3, this inconsistency may be attributed to cadmium's larger ionic radius (95 pm) compared to zinc (74 pm) [148]. The pure ZnO sample, seen in Figure IV. 3(a), consists predominantly of zinc (70.54% wt) and oxygen (29.46% wt). The Cd–ZnO 3% sample, as illustrated in Figure IV. 3(b), consists principally of zinc (43.05% wt), oxygen (55.77% wt), and cadmium (1.18% wt). For Cd–ZnO 7%: Figure IV. 3(c) indicates that the sample primarily consists of zinc (44.61% wt), oxygen (53.75% wt), and cadmium (1.64% wt). For Cd–ZnO 10%: Figure IV. 3(d) indicates that the sample basically consists of zinc (45.86% wt), oxygen (52.18% wt), and cadmium (1.97% wt).

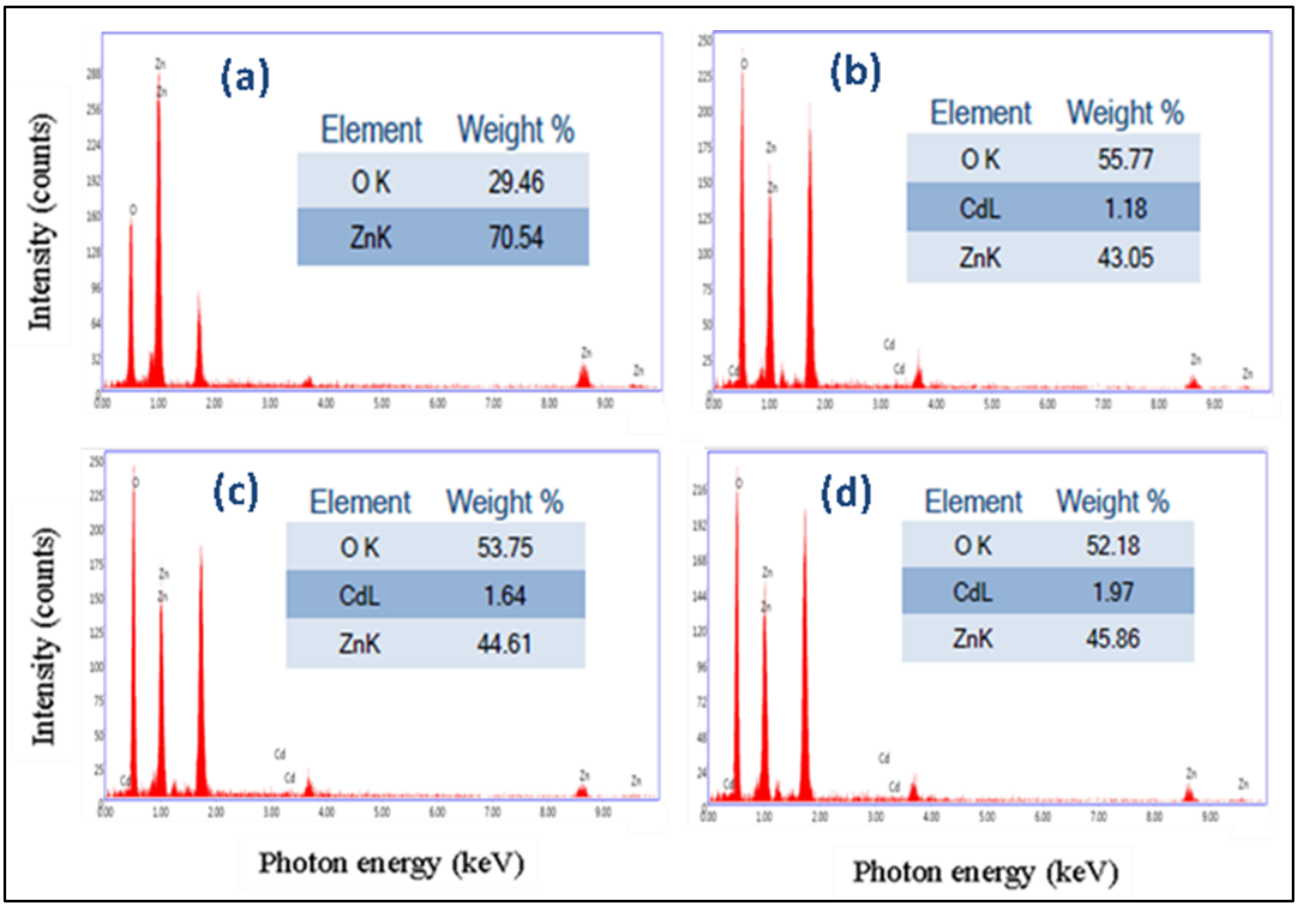


Figure IV.3: The EDS images of as-deposited layers (**a**) ZnO, (**b**) 3% Cd-ZnO, (**c**) 7% Cd-ZnO, and (**d**) 10% Cd-ZnO.

IV.3.3 Topographical analysis (AFM)

The topographical images of pure and Cd-doped ZnO thin films, obtained across an area of 1 x 1 µm² via AFM, are displayed in Figure IV.4(a–d) for 2D and in Figure IV. 5(a–d) for 3D representations. The root mean square (RMS) roughness values for the pure ZnO and Cd-doped ZnO films (3% wt, 7% wt, and 10% wt) are 143.72 nm, 125.9 nm, 194 nm, and 160.6 nm, respectively. The surface roughness (RMS) varied among the films with and without cadmium incorporation, with the 3% Cd-ZnO sample demonstrating the lowest RMS. In addition, the picture of 3% Cd-doped ZnO illustrates that the topological surface parameters derived from AFM correspond with those obtained from FESEM [149]. The RMS value signifies that the sample surface possesses a higher quantity of spaces capable of housing atoms, nuclei, or particles, thereby underscoring the significance of porosity (demonstrated in FESEM) and low APF (evidenced in XRD) [150]. The topography in Figure IV. 4(b) exhibits greater density compared to Figure IV. 4(a, c, d), resulting in elevated surface area values of 14.31 µm² (b), 8.352 µm² (a), 6.565 µm² (c) and 5.242 µm² (d). The 3% Cd-doped ZnO shows uniformity, minimal grain size, and a tightly packed surface, while the undoped ZnO, along with the 7% and 10% wt Cd-doped ZnO films, demonstrates greater grain sizes and less dense surfaces. 3% Cadmium-doped ZnO demonstrated a more uniform surface with a root mean square roughness of 125.9 nm. A smooth surface facilitates the adsorption of organic compounds, thus enhancing photocatalytic uses [149].

Table IV.3: Root mean square roughness, mean roughness, and surface area of the samples were calculated using Gwyddion software based on AFM images.

Samples	**ZnO**	**3% Cd-ZnO**	**7% Cd-ZnO**	**10% Cd-ZnO**
root mean square roughness (nm)	143.72	125.9	194	160.6
Mean roughness (nm)	114.6	98.6	159.3	124.1
Surface area (µm²)	8.352	14.31	6.565	5.242

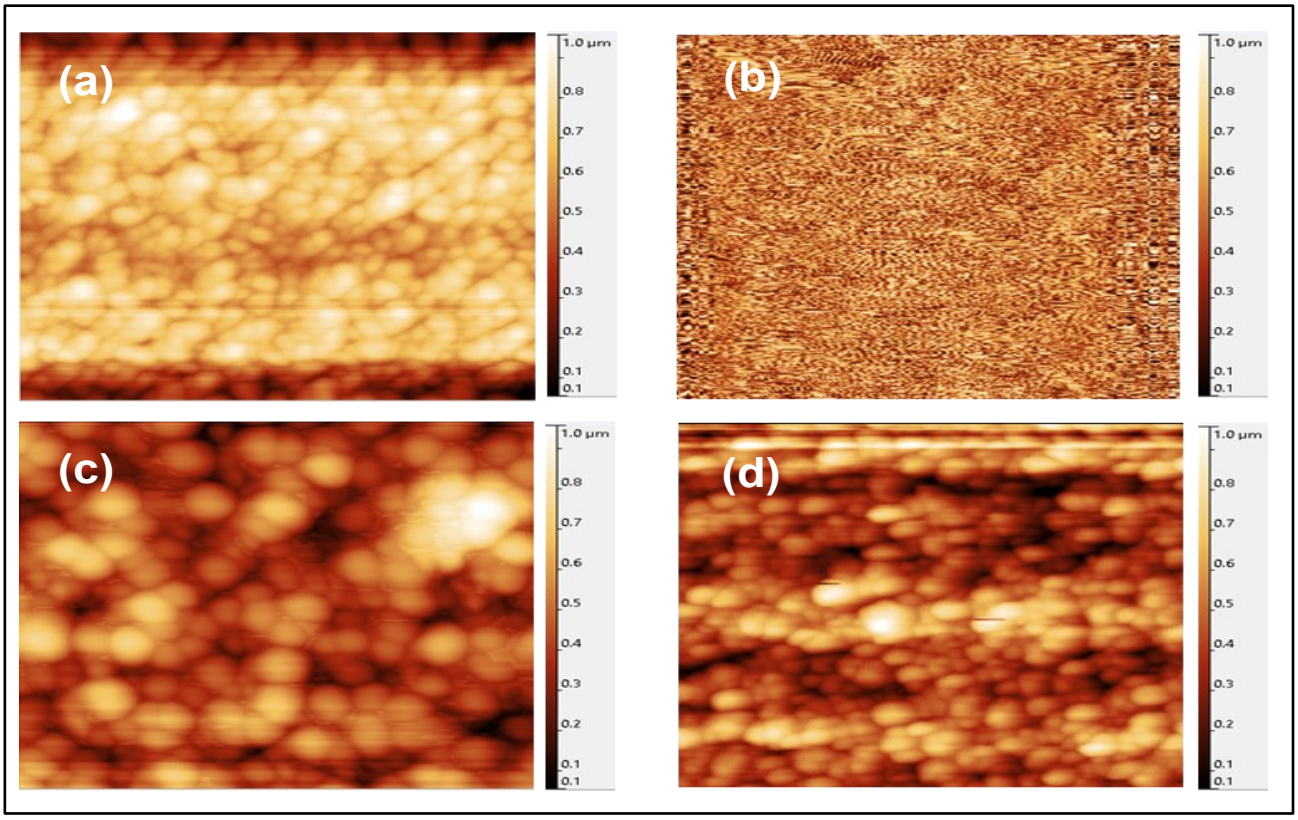


Figure IV.4: 2D AFM images of (**a**) ZnO, (**b**) 3% Cd-ZnO, (**c**) 7% Cd-ZnO, and (**d**) 10% Cd-ZnO thin films.

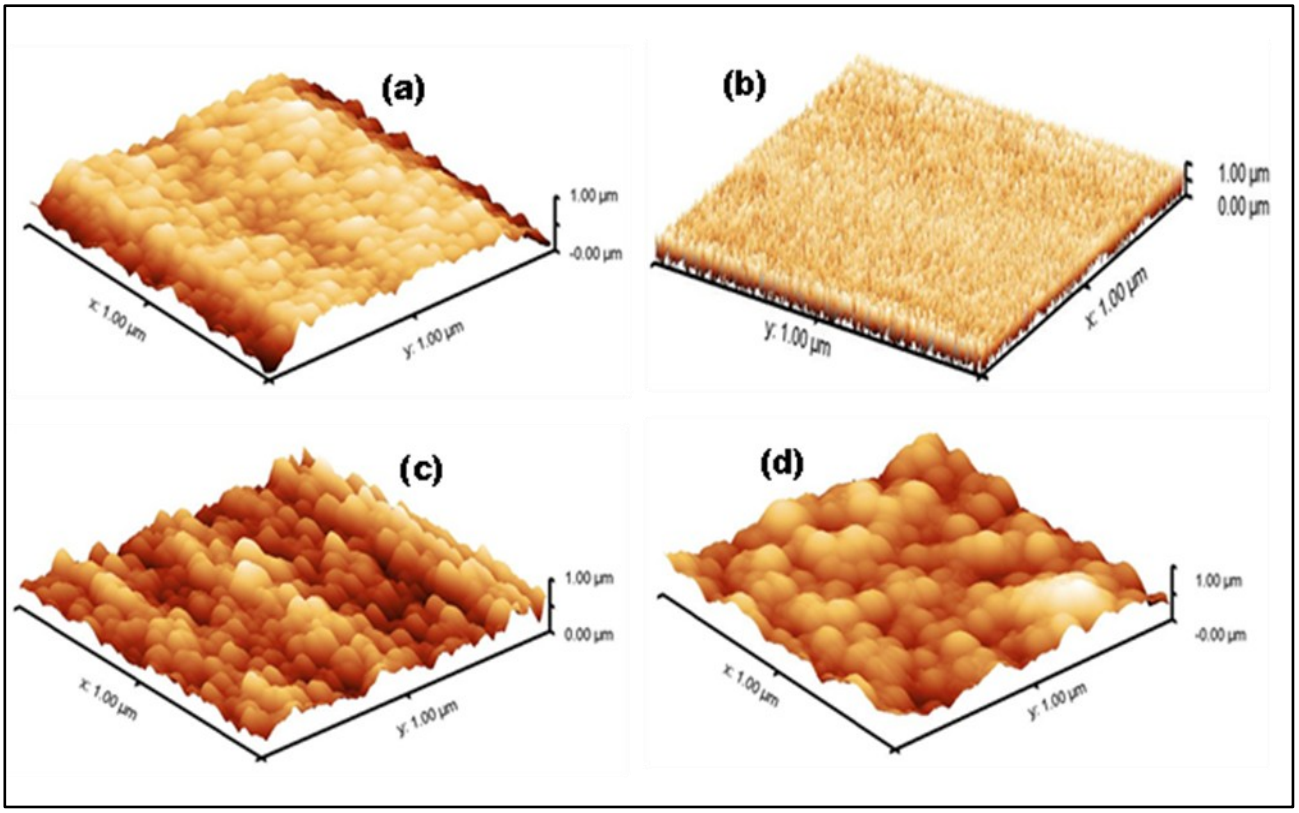


Figure IV.5: 3D AFM images of (**a**) ZnO, (**b**) 3% Cd-ZnO, (**c**) 7% Cd-ZnO, and (**d**) 10% Cd-ZnO thin films.

IV.3.4 Optical analysis

The optical properties, including transmittance, refractive index, extinction coefficient, and band gap energy spectra of ZnO and Cd-ZnO thin films within the wavelength range of 200–3200 nm, are given in Figures IV. 6,7, 8 and Table IV.4. The transmittance of the films increases with the incorporation of cadmium (Figures IV. 6). Compared to the pure zinc oxide film, the transmittance of Cd-doped zinc oxide was seen to rise within the ranges of 200 to 760 nm and 1050 to 3200 nm, whereas it decreased between 760 and 1050 nm for samples containing 3% and 7% wt. The mean optical transmittance of undoped ZnO is approximately 66.55%, but for Cd-doped ZnO at 3% wt, 7% wt, and 10% wt, the values are 73.02%, 73.75%, and 74.92%, respectively. As previously mentioned, Cd doping may introduce structural defects in the films and lead to the formation of smoother and denser grain boundaries, hence diminishing surface roughness, which can influence an increase of light scattering on the surface [71] .

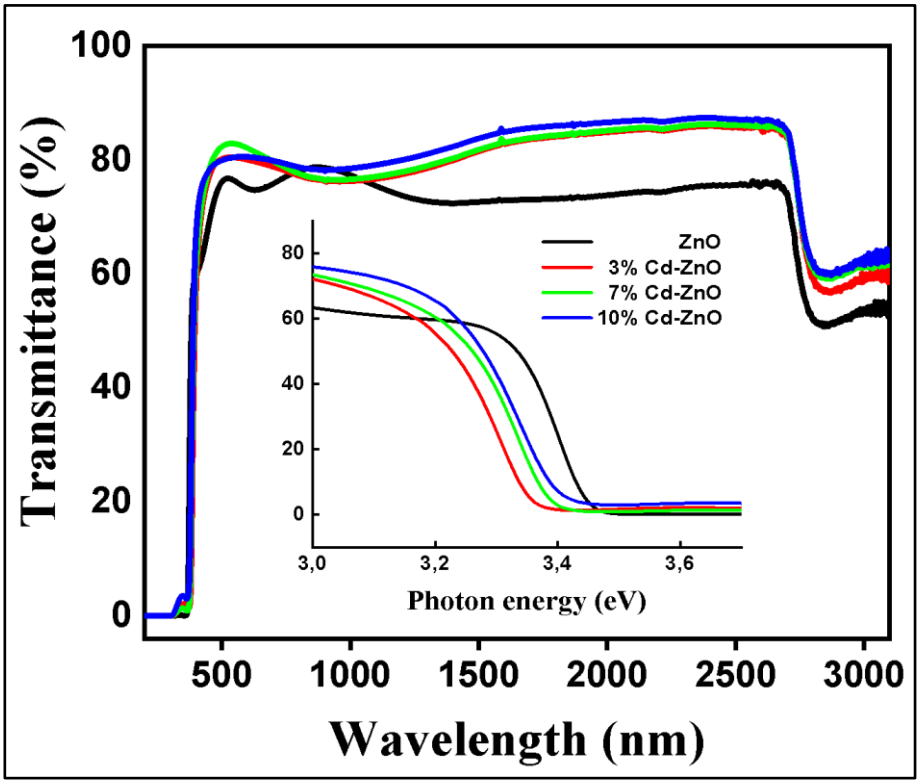


Figure IV. 6: Transmission spectra as a function of the wavelength and photon energy for all deposited films.

Figure IV. 7 shows the fluctuation of refractive index with wavelength for pure and Cd-doped zinc oxide thin films at different Cd^{2+} concentrations (x = 0.0, 0.03, 0.07, and 0.1). Our results

demonstrate that an increase in the percentage of Cd doping correlates with a decrease in refractive index values and an increase in transmittance values, with averages of 2.239 (66.55%), 2.263 (73.02%), 2.257 (73.75%), and 2.249 (74.92%) for pure zinc oxide, zinc oxide doped with 3%, zinc oxide doped with 7%, and zinc oxide doped with 10%, respectively (Table IV.4). Low refractive index values signify less crystallinity and hence heightened density, the transmittance rises, but the refractive index diminishes due to the integration of Cd^{2+} ions into the ZnO lattice, and vice versa [151], [152].

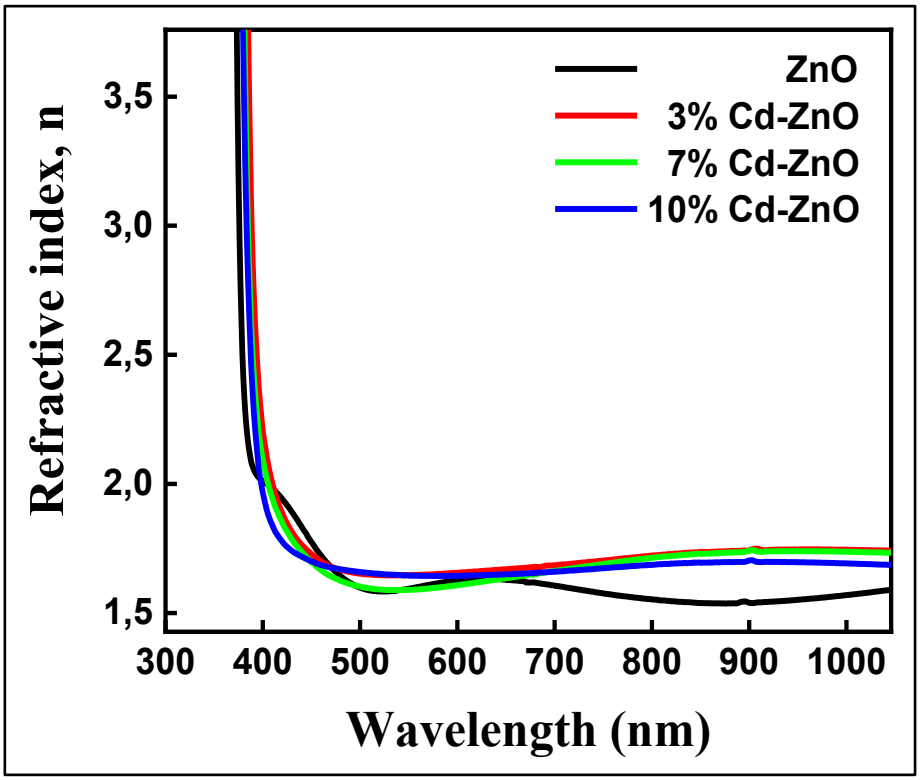


Figure IV. 7: Refractive index spectra as a function of the wavelength for all deposited films.

Eg denotes the optical band gap, and the exponent m typically varies according to the type of transition, with m being 2 for an indirect band gap material like ZnO, as stipulated by Tauc's model [153]. Figure IV.8 (a, b) and Table IV.4 depicts the fluctuation in Eg values for each sample. The bandgap energy (Eg) for undoped ZnO thin films is 3.32 eV; however, for samples with 3%, 7%, and 10% Cd-doping, the Eg values are reduced to 3.21 eV, 3.23 eV, and 3.24 eV, respectively. The reduction of the band gap may result from changes in the crystal lattice, ionic distances, particle sizes, and the morphology of deposited coatings, which can be ascribed to increased tensile stress due to the incorporation of impurities [31], [112]. Additionally, these values indicate that the wavelengths required to move electrons from the valence band to the

conduction band are in the ultraviolet range [22], [154], furthermore, a smaller crystallite size correlates with a reduced bandgap, indicating that doping with Cd necessitates less energy to excite the electrons [First IE: ionization energy (Ips: Ionization potentials) IE_{Cd} / IE_{ZnO} about 9.081eV/9.31 eV] [22], [155] .

Table IV.4: The gap energy, average refractive index (derived from the curve), refractive index computed via the Hervé-Vandamme model, and sample thickness were assessed using UV-visible spectroscopy measurements.

Samples	ZnO	3% Cd-ZnO	7% Cd-ZnO	10% Cd-ZnO
Gap energy (eV)	3.32	3.21	3.23	3.24
Mean refractive index (curve)	1.648	1.701	1.665	1.675
Refractive index (Herve-Vandamme)	2.239	2.263	2.257	2.249
Thickness (nm)	167	114	220	235

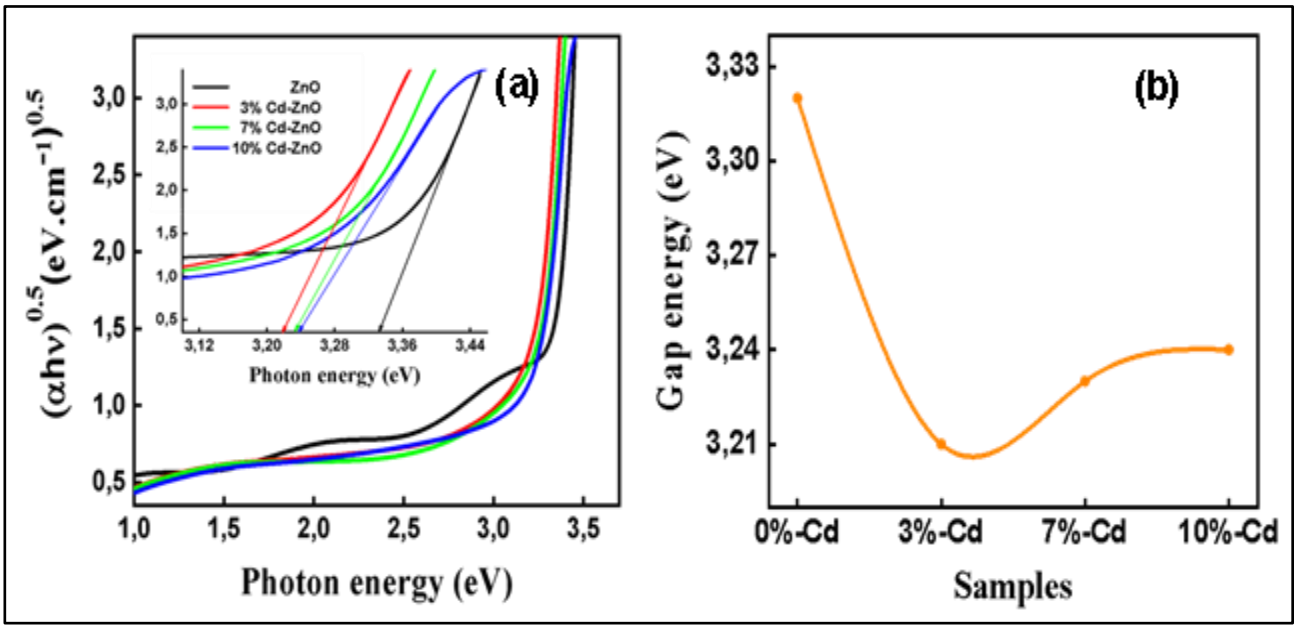


Figure IV. 8: (**a**), and (**b**) Energy gap values of the prepared samples Cd-ZnO.

IV.4 Photocatalytic activity study

After the examination of the structural, morphological, and optical properties of pure ZnO and Cd-doped ZnO films, we now assess their photocatalytic efficacy under natural sunlight exposure. Following to the previously established protocol.

IV.4.1 Photodegradation of MB

The photocatalytic activity of $Zn_{1-x}Cd_xO$ thin films (0, 3, 7 and 10 wt.%) was evaluated using an aqueous solution of methylene blue as the organic pollutant, where the initial MB concentration was 5 ppm under solar irradiation for 120 minutes.

Figure IV. 9(a-d) presents the optical adsorption spectra of the MB solution in the presence of photocatalysts under sunlight illumination at varying exposure durations for pure ZnO and CdZO films. As the irradiation duration grew, the absorbance reduced, thereby confirming that the active films effectively degraded the solution. Figure IV. 10 presents the results of MB photodegradation effectiveness assessments as a function of sunlight exposure duration, indicating that Cd-doped ZnO thin films displayed a superior MB degradation rate compared to pristine ZnO. Table IV.5 presents performance values, proving that dye degradation with the different photocatalysts is practically complete after 120 minutes of direct solar light exposure. A significant decrease in MB content and an improvement in photocatalytic performance was observed in Cd-doped ZnO thin films compared to pure ZnO. After 120 min a decomposition of 82.21% of MB was observed in the presence of pure ZnO. Upon the introduction of Cd in varied concentrations (3 wt%, 7 wt.%, and 10 wt.%), a notable enhancement in the degradation rate was seen, yielding rates of 98.35%, 93.12%, and 91.06%, respectively. The rate constant values for the first-order reaction k to Cd-ZnO thin films (0 wt., 3% wt., 7% wt, and 10% wt) were 0.0112 min^{-1}, 0.0269 min^{-1}, 0.0177 min^{-1}, and 0.0159 min^{-1}, respectively **(**Figure IV.11**)**. An uneven fluctuation of the kinetic constant with Cd weight concentrations is observed. The optimal value is achieved with sheets containing 3% Cd-ZnO. The reduction of the band gap and higher surface area in Cd-doped ZnO thin films promote electron-hole separation, hence preventing recombination and enhancing photocatalytic reaction efficiency [156], FESEM and AFM investigations demonstrate that increased surface areas enhance photocatalytic activity [31]. additionally, the enhancement in the breakdown of MB can be ascribed to Cd's role as an active element and an effective catalyst in photocatalytic applications. Moreover, the reduction in the energy gap amplifies the pairs (electrons/holes) accountable for discolouration, resulting in the generation of a substantial quantity of superoxide radicals ($\bullet O_2^-$) and hydroxyl radicals (•OH), respectively [31].

Table IV.5: Kinetic parameters for each catalyst, both undoped and cadmium-doped ZnO.

Samples	k (min^{-1})	D (%)	E	R^2
Pure ZnO	0.0112	82.21	0.0012	0.929
3% Cd-ZnO	0.026	98.35	0.0037	0.89
7% Cd-ZnO	0.0177	93.12	0.0013	0.966
10% Cd-ZnO	0.0159	91.06	0.0013	0.959

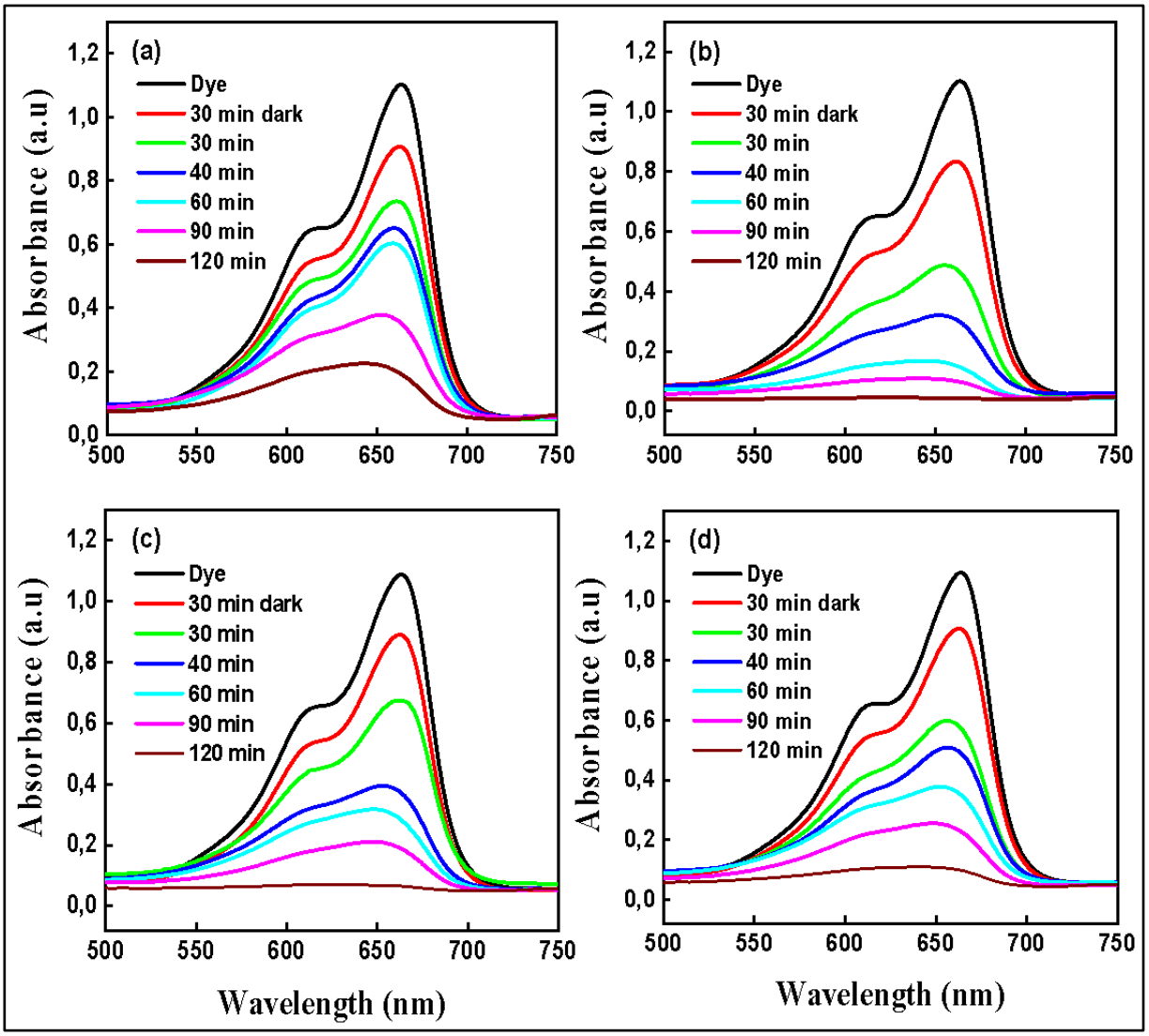


Figure IV. 9: MB absorbance at different time intervals in the presence of ZnO, and Cd-doped ZnO catalysts under sunlight irradiation.

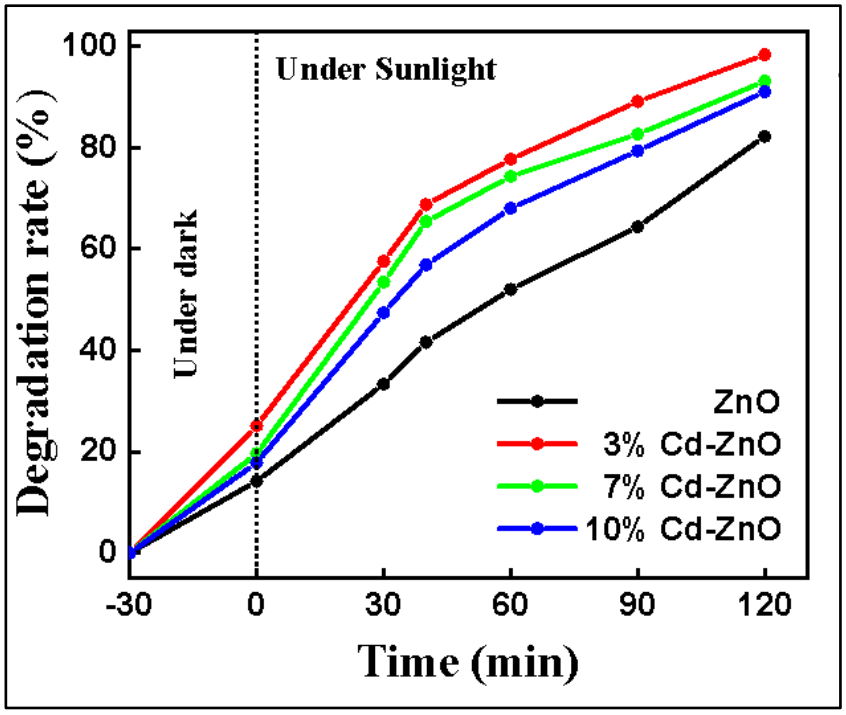


Figure IV. 10: Photocatalytic efficiency of pure and Cd-doped ZnO of MB as a function of time under sunlight exposure.

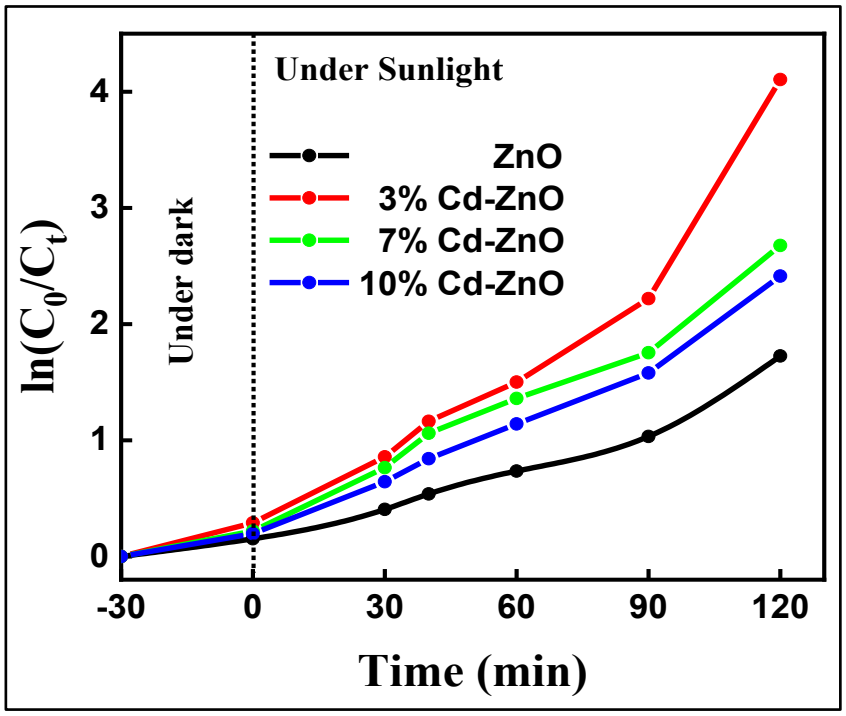


Figure IV. 11: Photocatalytic dye degradation kinetics of the prepared pure and Cd-doped ZnO thin films.

IV.4.2 Mechanism of photodegradation behaviour

Figure IV. 12 illustrates the suggested method for degrading the organic-coloured compound MB using the pristine ZnO and Cd-doped ZnO thin films. Upon exposure to solar light with energy equivalent to or beyond its bandgap ($E_{hv} \geq Eg$), a valence band electron in a photocatalyst becomes excited, transitions to the conduction band, and generates a hole. The generated electron-hole pair may recombine without additional reaction or move to the photocatalyst surface for the photocatalytic destruction of organic dyes. We seek to impede electron-hole recombination to facilitate subsequent reactions. To accomplish this, ZnO and Cd-ZnO thin layers are engineered to efficiently inhibit the recombination of photogenerated electrons and holes by efficient separation. Photogenerated electrons migrate from the valence band (VB) of the photocatalyst to its conduction band (CB), resulting in the formation of a positively charged hole (h^+) in the VB. The catalyst, or photocatalyst, mitigates the recombination of photogenerated holes (h^+) and electrons (e^-) by energising electrons to elevated energy states. The oxidation and reduction reaction occurs on the photocatalyst surface, where molecular oxygen is reduced to the superoxide radical $^{\bullet}O^{-2}$ (a free radical) through the excitation of electrons. The hydroxyl ion is oxidized to the hydroxyl free radical via a vacancy created upon electron excitation. Holes and electrons, the principal active species, engage in redox processes, transforming O_2 and water/OH ions into $^{\bullet}OH/O^{-2}$ secondary active species/free radicals, which subsequently breakdown into non-toxic free radicals [156], [157]. Photo-generated electrons are transported to the valence band (VB) and conduction band (CB). The electrons interact with molecular oxygen to produce the less harmful superoxide anion radical ($^{\bullet}O_2$) through reductive mechanisms. The vacancy in the valence band may draw electrons from hydroxyl ions or water, resulting in the formation of a highly reactive hydroxyl radical ($^{\bullet}OH$) through an oxidative mechanism. The superoxide radical anions($^{\bullet}O_2^-$) and the hydroxyl radical ($^{\bullet}OH$) interact with electron–hole pairs, resulting in the formation of H_2O_2 [156].

The following equations give the degradation reactions of the dye in sunlight [31], [158]:

$$\text{Cd-doped ZnO} \xrightarrow{(E_{hv} \geq Eg)} \text{Cd-doped ZnO } (e^-_{(CB)} + h^+_{(VB)}) \quad \text{(IV.1)}$$

$$h^+ + H_2O \rightarrow H^+ + OH^- \quad \text{(IV.2)}$$

$$h^+ + OH^- \rightarrow {}^{\bullet}OH \quad \text{(IV.3)}$$

$$e^- + O_2 \rightarrow {}^{\bullet}O_2^- \quad \text{(IV.4)}$$

$$^{\bullet}O_2^- + H+ \rightarrow HO_2^{\bullet} \quad \text{(IV.5)}$$

$$2HO_2^{\bullet} \rightarrow H_2O_2 + O_2 \quad \text{(IV.6)}$$

$$H_2O_2 + {}^{\bullet}O_2^- \rightarrow OH^- + {}^{\bullet}OH + O_2 \quad \text{(IV.7)}$$

$$H_2O_2 + e^- \rightarrow OH^- + {}^{\bullet}OH \quad \text{(IV.8)}$$

$$\text{Dye} + OH^{\bullet} \rightarrow \text{dye decolorization} \quad \text{(IV.9)}$$

$$\text{Dye} + h^+_{VB} \rightarrow \text{dye oxidation} \quad \text{(IV.10)}$$

$$\text{Dye} + e^-_{CB} \rightarrow \text{dye reduction} \quad \text{(IV.11)}$$

$$MB + ({}^{\bullet}OH, {}^{\bullet}O_2^-) \rightarrow H_2O + CO_2 + \text{Other products} \quad \text{(IV.12)}$$

The Butler and Ginley equations are employed to ascertain the EVB and ECB of a semiconductor in its zero-charge state. The band gap energies (Eg) of pure ZnO and Cd-doped ZnO thin films are detailed below: 3.32 eV for pure ZnO; 3.21 eV for 3% Cd-doped ZnO; 3.23 eV for 7% Cd-doped ZnO; and 3.24 eV for 10% Cd-doped ZnO. The conduction and valence band values (ECB, EVB) for the samples are: (-0.26, 3.06), (-0.205, 3.005), (-0.215, 3.015), and (-0.22, 3.02 eV) for pure ZnO and Cd-ZnO at 3, 7, and 10 wt %, respectively.

The addition of Cd reduces the band gap and alters the positions of the conduction and valence band boundaries. Consequently, the effect of Cd enhanced the reducing characteristics in the conduction band and the oxidising capabilities of holes in the valence band [31], [159]. The degrading efficacy is intricately linked to the band gap properties of the photocatalyst. Cadmium-doped zinc oxide demonstrates a decreased band gap energy of 3.21 eV in contrast to pure zinc oxide, which has a band gap of 3.32 eV. The decrease in the band gap facilitates improved electron excitation from the valence band to the conduction band upon irradiation. As a result, the production of photo-induced charge carriers escalates, facilitating interactions with adsorbed oxygen and water molecules to generate reactive free radicals. These reactive species are essential in photocatalytic degradation, which points to the importance of band gap regulation in enhancing the photocatalytic process [149]. Cadmium functions as an electron trap, diminishing the recombination rate of electrons and holes, hence enhancing the availability of charge carriers for photocatalytic processes [160].

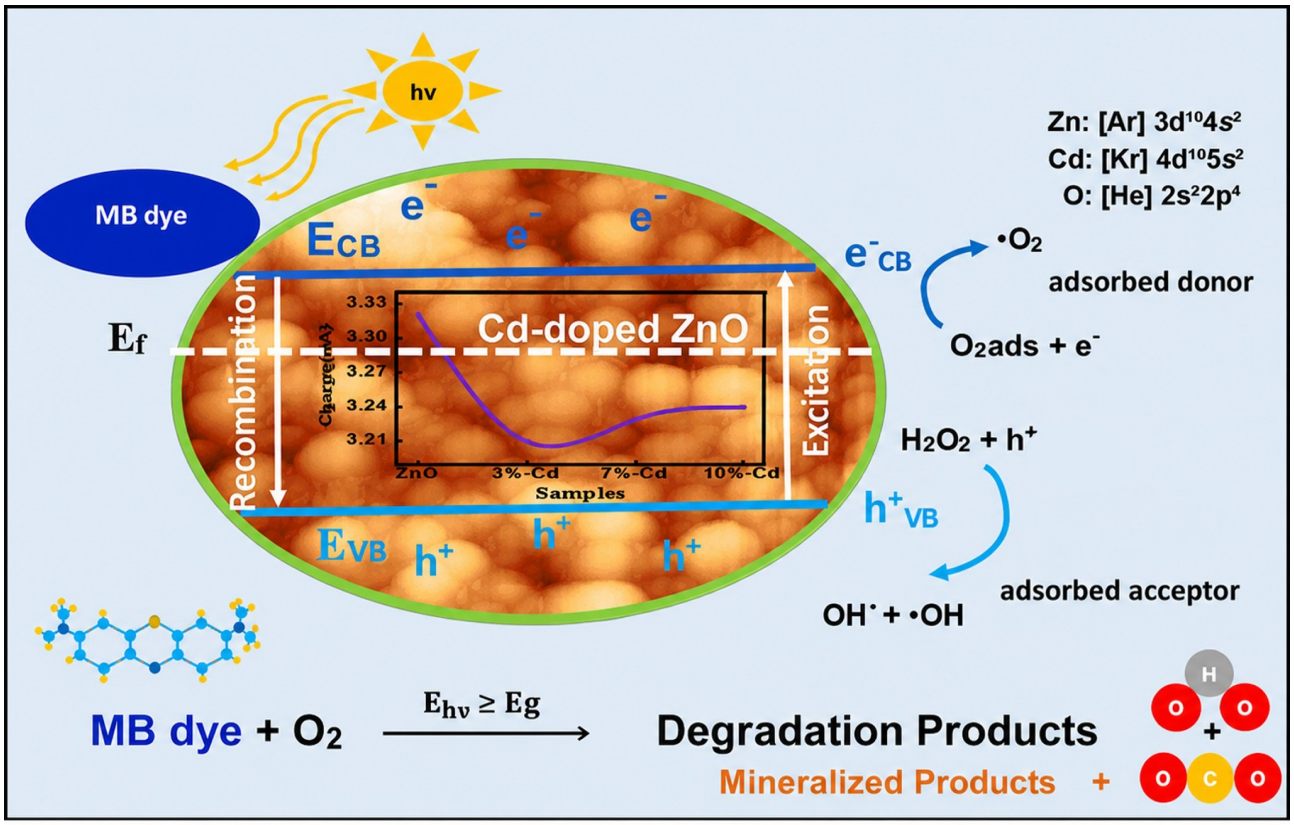


Figure IV. 12: Photocatalytic dye degradation mechanism of Cd-ZnO film.

IV.4.3 Trapping element study

The determination of the radical species responsible for dye discolouration can be efficiently conducted using a scavenger or trapping agent investigation. This method entails the incorporation of designated scavenger materials to sequester reactive radicals throughout the photocatalytic degradation process; hence, it aids in the identification of the relevant species. Diverse scavengers, including EDTA (ethylenediaminetetraacetic acid, disodium salt), CN (cupric nitrate), AscA (L-ascorbic acid), and IPA (isopropyl alcohol), were used in the trapping investigations of the primary reactive species. These scavengers were employed to capture holes (h^+), electrons (e^-), superoxide ($^{\bullet}O_2$), and hydroxyl radicals ($^{\bullet}OH$), respectively. Radical trapping experiments were conducted to elucidate the photocatalytic mechanism and identify the principal active species responsible for the degradation of methyl blue using Cd-doped ZnO thin films under sunlight exposure. Figure IV. 13 illustrates that a scavenger test was conducted by observing the degradation of MB before and after two hours of sunlight exposure, both in

the presence and absence of scavengers. The graph demonstrates that the incorporation of EDTA, a hole (h^+) scavenger, resulted in a significant reduction in degradation efficiency, decreasing it from 98.35% to 12.64%. This finding indicates that h^+ serve as the principal oxidising agents in the system. The addition of IPA, a hydroxyl radical (•OH) scavenger, markedly hindered the process, highlighting the secondary role of •OH. Under these conditions, the pollutant degradation rate reached 38.29%. In contrast, the addition of AscA, a superoxide radical anion ($•O_2$) scavenger, showed a significant effect, with decomposition in the range of 46.87%. The incorporation of CN, an electron (e-) scavenger, exhibited a negligible impact. The findings strongly support a mechanism whereby photogenerated electrons are captured by Cd sites, which then react efficiently with adsorbed oxygen to generate $^{\bullet}O_2$ radicals. The prolonged existence of the holes leads to a substantial production of $^{\bullet}$OH radicals, either from direct water oxidation or the subsequent transformation of $•O_2$, which serve as the primary catalysts for dye degradation [159] .

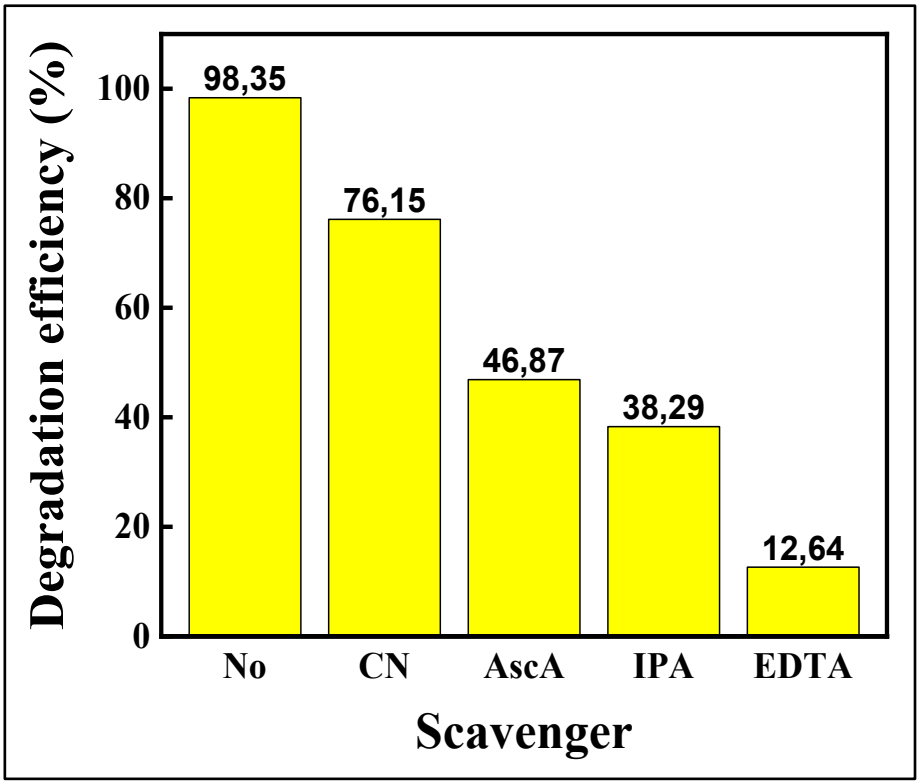


Figure IV. 13: Degradation efficiency of MB over the 3% Cd-ZnO catalyst in the absence and presence of different scavengers under sunlight irradiation.

IV.4.4 Stability and reusability study

The potential for repeated use of the photocatalyst 3% Cd-doped ZnO thin film, as depicted in Figure IV.14(a). The catalyst as a photocatalyst was assessed via photodegradation tests targeting the degradation of methyl blue (MB) under suns for 120 minutes. In these tests, consistent conditions (sample area of 2 cm × 2 cm in a 10 ml solution with a pH of about 7.5 and a concentration of 2.5×10^{-5} mol L-1 MB) were maintained during six cycles to decompose MB. After each cycle, the catalyst was extracted and meticulously cleaned with distilled water to eliminate any remaining colours and reaction byproducts before being dried for future reuse.

The results indicated that the catalyst maintained a high degree of photocatalytic efficacy throughout the cycles (Figure IV.14), with a slight decrease below 5%. The results demonstrate that the catalyst exhibits excellent stability and reusability under the evaluated conditions. The marginal decline in performance is ascribed to variables such as surface photo-corrosion, surface pollution, minor structural alterations, or insufficient removal of residues during the recovery process (Table IV.6) [161], [162]. In conclusion, these findings affirm that the Cd-ZnO film is a viable and resilient photocatalyst for the recurrent degradation of dyes under solar illumination.

Figure IV.14(b, c, d, e and f) illustrates the XRD, FESEM, and EDX investigations of 3 wt% Cd-doped ZnO, both prior to and following six regeneration cycles. X-ray diffraction (XRD) images demonstrate that the crystal structure remained invariant. Subsequent to the experiment, the diffraction peaks exhibited diminished intensity and enhanced form, accompanied by the emergence of novel peaks aligning with the ICDD ZnO pattern. This is ascribed to enhanced crystallinity and the elimination of surface impurities during the process. No supplementary peaks associated with secondary phases were seen, signifying that the material preserved its structural integrity **(**Figure IV.14(a, b)**)**. Figure IV.14.(c. d) illustrates that the catalyst's morphology remains fundamentally unaltered in both form and particle size after six consecutive cycles, hence affirming its exceptional stability. Figure IV.14(e. f) EDS revealed little variations in the composition of the 3 wt% doped-ZnO, with O and Cd increasing slightly from 55.77% to 57.21% and from 1.18% to 1.93%, respectively, while Zn declined from 43.05% to 40.86%, indicating that the films predominantly maintain their composition. Ultimately, the results indicate the strong stability of the catalysts and confirm that no photocorrosion transpired during the photocatalytic performance.

Table IV. 6: Reusability of the catalyst, reaction time, and degradation efficiency (D) of methylene blue for 3% Cd-doped ZnO at 120 min

No. of cycles	**1**	**2**	**3**	**4**	**5**	**6**
D (%)	98.35	96.12	97.78	97.88	96.95	95.52
K (min^{-1})	0.63	0.67	0.68	0.69	0.64	0.67
R^2	0.89	0.90	0.92	0.93	0.89	0.91

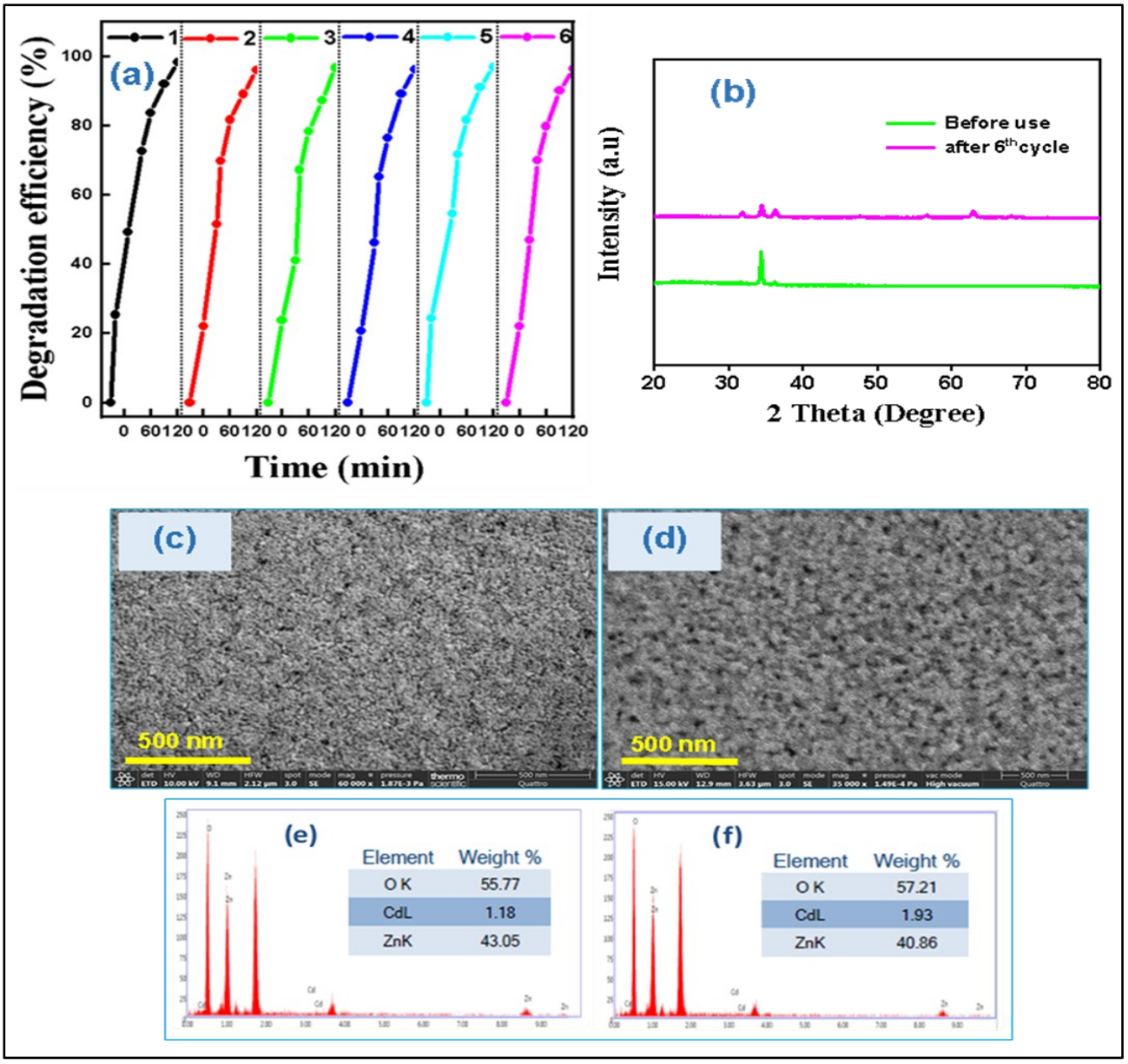


Figure IV. 14: Photocatalytic test of reusability of the 3% Cd-ZnO thin film for MB dye under sunlight: (a) Degradation efficiency; (b) DRX prior to and subsequent to the 6th cycle; (c) SEM-FEG preceding and (d) following the study; (e) and (f) EDX before and after the test reusability, respectively.

IV.5 Photodetection investigation

The pure and cadmium-doped ZnO thin film samples were analysed for photocurrent under dark conditions and UV illumination at a wavelength of 365 nm with a power intensity of 90 mW/cm². The sample had an area of 1.5 x 2 cm², and the corresponding photocurrent was documented using a source meter connected via copper electrodes, as shown in the schematic design in Figure IV.15. Figure IV. 16(a-b) shows the I-V curves for Cd-doped ZnO and pure ZnO in the dark and under UV illumination. The ohmic characteristics of the manufactured devices are displayed in the linear voltage (V) vs. current (i) graph.

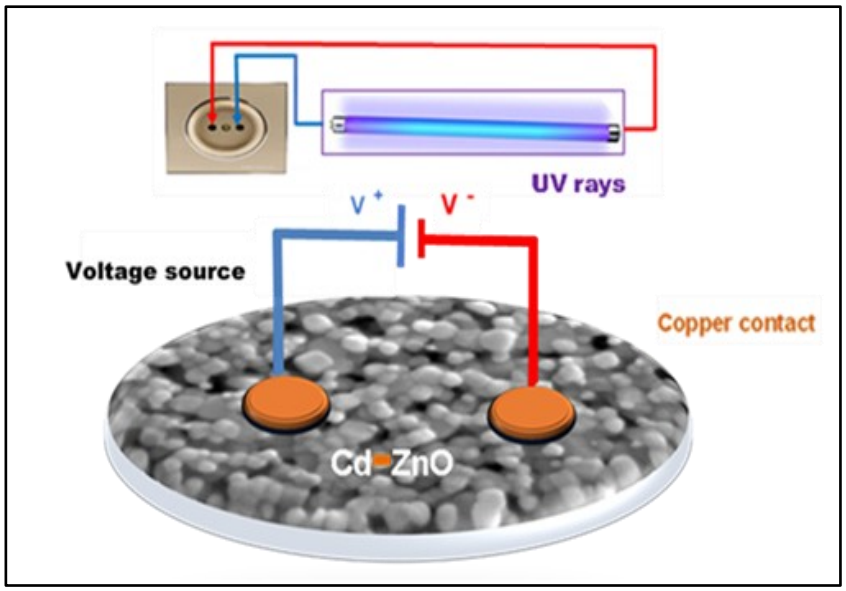


Figure IV. 15: Schematic for a fabricated photodetector device.

The sensitivity of a photodetector is defined by the fluctuation of its electrical signal in response to illumination. Under a bias voltage of 5 V and at ambient temperature, the currents recorded under UV irradiation for pure ZnO and samples doped with 3%, 7%, and 10% wt of cadmium were 6.96 nA, 12.46 nA, 9.46 nA, and 12.86 nA, respectively. The respective dark currents were 6.43 nA, 7.96 nA, 7.023 nA, and 7.56 nA (Table IV.7).

The photodetection efficacy of the cadmium-doped ZnO-based photodetector, particularly its sensitivity (S), responsiveness (R), and detectivity (D), was ascertained from the obtained current-voltage (I-V) curves. Table 7 illustrates the corresponding values for each sample.

The sensitivity of a photodetector denotes its capacity to transform incident light into a quantifiable electrical signal. The computed values for pure and cadmium-doped ZnO samples (3%, 7%, and 10%) are 1.06, 1.57, 1.35, and 1.57, respectively.

The responsiveness of a photodetector indicates its capacity to effectively transform incident radiation into a quantifiable electrical signal. The sensitivity of the pure ZnO film was measured at 25.79 nA/W. The value climbs to 46.14 nA/W for the sample doped with 3% cadmium, subsequently lowers to 35.03 nA/W for the film doped with 7% cadmium, and then rises to 43.92 nA/W for the sample with 10% cadmium.

The detectivity of a photodetector signifies its capacity to identify minimal optical powers. The detectivity values for pure ZnO and samples doped with 3%, 7%, and 10% Cd are 9.85×10^5, 15.34×10^5, 12.8×10^5, and 15.47×10^5 Jones, respectively.

Cd-ZnO-based photodetectors doped with 3% and10% exhibit enhanced performance, marked by elevated detectivity, responsiveness, and sensitivity. This enhancement is associated with augmented generation and effective separation of charge carriers under ultraviolet irradiation.

This resistance increases in direct proportion to the number of free electrons and, consequently, the concentration of holes associated with oxygen ions. Cadmium doping improves device performance by reducing the sample's resistivity and increasing charge carrier density. [70], [137], [138], [139].

Table IV.7: Photocurrent performance of pure and cadmium-doped ZnO thin films measured at 5 volts.

Samples Cd (%)	S	R (nA/W)	D $\times 10^5$ (Jones)
0	1.06	25.79	9.85
3	1.57	46.14	15.84
7	1.35	35.03	12.8
10	1.57	43.92	15.46

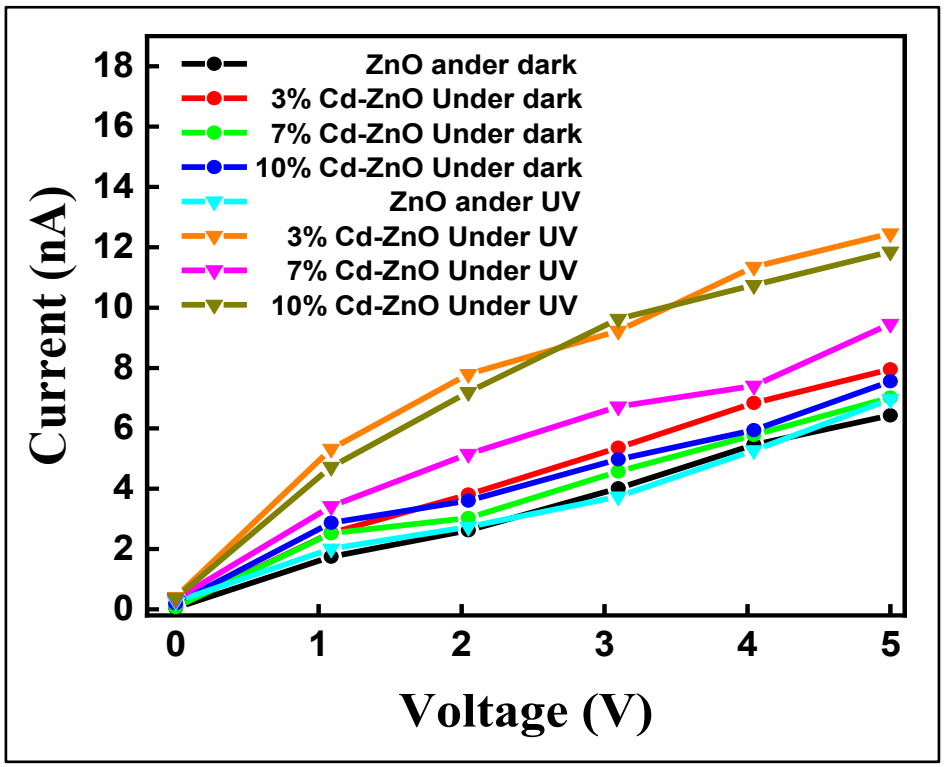


Figure IV. 16: Current measured as a function of voltage in darkness mode and under UV light for (**a**) pure ZnO, (**b**) 3% Cd-doped ZnO, (**c**) 7% Cd-doped ZnO and (**d**) 10% Cd-doped ZnO thin films.

IV.6 Conclusion

On to glass substrates via the dip-coating process. The synthesised materials were characterised using multiple techniques, including X-ray diffraction (XRD), energy-dispersive spectroscopy (EDS), scanning electron microscopy (FESEM), atomic force microscopy (AFM), and ultraviolet-visible spectroscopy (UV-VIS). His study involved the deposition of pristine and Cd-doped ZnO thin films. The deposited thin films were employed as photocatalysts for the degradation of methylene blue under solar radiation. Compared to pristine ZnO, Cd-doped ZnO films exhibited superior photocatalytic activity. Under sunlight exposure, the 3% Cd-doped ZnO sample achieved the highest photocatalytic performance, with efficiencies of 98.35% after 120 minutes. The active species trapping experiments confirmed that h+ and •OH play crucial roles in the photocatalytic degradation of MB. Moreover, reusability tests validated the stability and reliability of the film after six consecutive cycles. Further investigation is warranted for this thin film, as it holds a potential as an eco-friendly photocatalyst for a broader range of pollutants; therefore, we suggest that cadmium doping is an effective method to enhance the

photocatalytic capabilities of ZnO thin films for environmental applications. Examination of photodetection metrics (sensitivity, responsiveness, and detectivity) indicates that ZnO films doped with 3% and 10% cadmium demonstrate enhanced performance relative to other samples.

General conclusion and future works

This work seeks to create high-performance transparent conductive oxide thin films by evaluating the impacts of doping zinc oxide with non-metal (sulfur) and metal (cadmium). The physical attributes and photocatalytic properties of these specimens have been examined. Subsequently, a little component was incorporated into the conclusion of this investigation, specifically a photodetection application. This study synthesized virgin ZnO and ZnO modified with sulfur and cadmium thin films using a simple and cost-effective dip coating process, and examined their structural, morphological, optical, photocatalytic, and photocurrent properties.

The films were evaluated using XRD, FESEM, EDS (EDX), AFM, and UV-vis spectrophotometry to evaluate their structural, morphological, and optical features.

The paper presents the development of pure ZnO, S-doped ZnO, and Cd-doped ZnO thin films fabricated using the sol-gel dip coating technique. X-ray diffraction analysis verified the formation of zinc oxide (ZnO) crystals and sulfur and cadmium-modified zinc oxide as thin-film phases in the fabricated film system. This signifies that all films possess a hexagonal wurtzite structure and demonstrate a preferred orientation along the (002) plane of zinc oxide. SEM morphological examinations have revealed a high level of homogeneity in the produced films. The thin film samples exhibit nanostructures characterised by minimal size dispersion, spherical morphology, and an exceptionally high density. The 2 wt% sulfur-doped thin film exhibits wrinkles and diminutive spherical particles, with an average grain size of 174.225 nm and a porosity of 15.162%; these wrinkles are linked. The creases expanded the film's surface area beyond early projections, possibly augmenting catalytic activity. In contrast, zinc oxide doped with 3 wt% cadmium showed very small particles and high density, potentially enhancing catalytic activity. EDS verifies the presence of the deposited element peaks (Zn, O, S, and Cd) in this study, which were distinctly observable. According to AFM analysis, for S-doped ZnO on the substrate surface, the grains are evenly distributed in all of the films. One of the various features of the ZnO thin film is its rough surface, which is caused by internal strain and the lattice mismatch that forms within them. Consequently, the active surface area grows and becomes more capable of absorbing light, while the 3% cadmium-doped zinc oxide displays a smooth, homogeneous, and dense surface characterised by diminished root-mean-square roughness, resulting in enhanced charge mobility and decreased recombination. Optical tests show that adding sulphur to zinc oxide slightly reduces the average light transmittance and lowers the energy gap. In contrast, adding cadmium improves light transmittance and also lowers the energy gap.

The concluding section described the photocatalytic degradation of methylene blue dye using both pure oxides and doped thin films. Cadmium-doped zinc oxide demonstrated high photocatalytic activity, achieving 98.35% degradation of methylene blue within 120 minutes under sunlight, while sulphur-doped zinc oxide showed significant pollutant degradation, reaching 96.71% within 90 minutes under direct sunlight and 94.69% within 50 minutes under UV light. Over six consecutive cycles, the doped thin films exhibited remarkable reusability and high photostability, making them an attractive option for organic pollutant removal in wastewater treatment.

Doped thin films demonstrate enhanced sensitivity in ultraviolet photodetection relative to undoped zinc oxide. Cadmium-doped zinc oxide exhibits enhanced performance relative to sulphur-doped zinc oxide.

This thesis presents a cost-efficient method for producing doped thin films, designed to expand absorption bands while preserving stable photocatalytic characteristics, specifically for water treatment applications utilising sunlight.

According to the results of this study, the following future studies are suggested:

- ✓ More extensive characterizations are necessary such us Raman spectroscopy, measurements of Hall effect, XPS.
- ✓ Testing other types of pollutants such as: pesticides, antibiotics, etc.
- ✓ Studying another application of the deposited films in, gas sensing and antibacterial, etc.

Bibliography

[1] A. D. Terna, E. E. Elemike, J. I. Mbonu, O. E. Osafile, and R. O. Ezeani, "The future of semiconductors nanoparticles: Synthesis, properties and applications," *Materials Science and Engineering: B*, vol. 272, no. June, p. 115363, 2021, doi: 10.1016/j.mseb.2021.115363.

[2] K. Zhao *et al.*, "Investigation on Transparent, Conductive ZnO:Al Films Deposited by Atomic Layer Deposition Process," *Nanomaterials*, vol. 12, no. 1, pp. 1–10, 2022, doi: 10.3390/nano12010172.

[3] P. Jongnavakit, P. Amornpitoksuk, S. Suwanboon, and T. Ratana, "Surface and photocatalytic properties of ZnO thin film prepared by sol-gel method," *Thin Solid Films*, vol. 520, no. 17, pp. 5561–5567, 2012, doi: 10.1016/j.tsf.2012.04.050.

[4] M. Kumar, H. Jeong, and D. Lee, "Sol-gel derived Hf- and Mg-doped high-performance ZnO thin film transistors," *J. Alloys Compd.*, vol. 720, pp. 230–238, 2017, doi: 10.1016/j.jallcom.2017.05.266.

[5] M. Caglar, K. Sever, S. Aktas, and A. Demiroglu, "Improving the electrical performance of NiO based photodiode fabricated by sol-gel process with Al doping," *Sens. Actuators A Phys.*, vol. 350, no. November 2022, p. 114099, 2023, doi: 10.1016/j.sna.2022.114099.

[6] R. S. Pedanekar, S. K. Shaikh, and K. Y. Rajpure, "Thin film photocatalysis for environmental remediation: A status review," *Current Applied Physics*, vol. 20, no. 8, pp. 931–952, Aug. 2020, doi: 10.1016/J.CAP.2020.04.006.

[7] "Handbook of Electronic and Photonic Materials," *Materials Today*, vol. 10, no. 1–2, p. 55, Jan. 2007, doi: 10.1016/S1369-7021(06)71793-X.

[8] H. Adachi and K. Wasa, "Thin Films and Nanomaterials," *Handbook of Sputter Deposition Technology: Fundamentals and Applications for Functional Thin Films, Nano-Materials and MEMS: Second Edition*, pp. 3–39, Jan. 2012, doi: 10.1016/B978-1-4377-3483-6.00001-2.

[9] G. Kumar, "The Crucial Role of Semiconductors in Advancing Electrical Engineering," Jan. 2024.

[10] H. He, *Metal oxide semiconductors and conductors*. Elsevier Inc., 2020. doi: 10.1016/B978-0-12-814930-0.00010-4.

[11] S. Calnan and A. N. Tiwari, "High mobility transparent conducting oxides for thin film solar cells," *Thin Solid Films*, vol. 518, no. 7, pp. 1839–1849, Jan. 2010, doi: 10.1016/J.TSF.2009.09.044.

[12] A. N. Banerjee and K. K. Chattopadhyay, "Recent developments in the emerging field of crystalline p-type transparent conducting oxide thin films," *Progress in Crystal Growth and Characterization of Materials*, vol. 50, no. 1–3, pp. 52–105, Jan. 2005, doi: 10.1016/J.PCRYSGROW.2005.10.001.

[13] H. Natsuhara *et al.*, "TiO2 thin films as protective material for transparent-conducting oxides used in Si thin film solar cells," *Solar Energy Materials and Solar Cells*, vol. 90, no. 17, pp. 2867–2880, 2006, doi: 10.1016/j.solmat.2006.05.001.

[14] Z. L. Wang, "Zinc oxide nanostructures: Growth, properties and applications," *Journal of Physics Condensed Matter*, vol. 16, no. 25, 2004, doi: 10.1088/0953-8984/16/25/R01.

[15] M. F. Al-Kuhaili, S. M. A. Durrani, A. S. El-Said, and R. Heller, "Enhancement of the refractive index of sputtered zinc oxide thin films through doping with Fe2O3," *J. Alloys Compd.*, vol. 690, pp. 453–460, Jan. 2017, doi: 10.1016/J.JALLCOM.2016.08.165.

[16] L. Lew Yan Voon, M. Willatzen, M. Cardona, and N. Christensen, "Terms linear in k in the band structure of wurtzite-type semiconductors," *Phys. Rev. B Condens. Matter Mater. Phys.*, vol. 53, no. 16, pp. 10703–10714, 1996, doi: 10.1103/PhysRevB.53.10703.

[17] A. Janotti and C. G. Van De Walle, "Fundamentals of zinc oxide as a semiconductor," *Reports on Progress in Physics*, vol. 72, no. 12, 2009, doi: 10.1088/0034-4885/72/12/126501.

[18] Y. Kang, F. Yu, L. Zhang, W. Wang, L. Chen, and Y. Li, "Review of ZnO-based nanomaterials in gas sensors," *Solid State Ion.*, vol. 360, p. 115544, Feb. 2021, doi: 10.1016/J.SSI.2020.115544.

[19] M. D. McCluskey and S. J. Jokela, "Defects in ZnO," *J. Appl. Phys.*, vol. 106, no. 7, pp. 1–13, 2009, doi: 10.1063/1.3216464.

[20] M. D. McCluskey, *Defects in ZnO*, no. 0. Elsevier Ltd, 2018. doi: 10.1016/B978-0-08-102053-1.00001-6.

[21] K. Saravanan, P. Seenuvasakumaran, N. J. Begum, R. Balaji, N. Jabena Begum, and R. Balaji, "Synthesis and characterization of ZnO and Ce-doped ZnO thin films by simplified spray pyrolysis technique," *Ceram. Int.*, vol. 51, no. 29PC, pp. 62074–62082, Dec. 2025, doi: 10.1016/j.ceramint.2025.10.440.

[22] E. Edgardo, G. Sánchez, V. Hugo, M. Landeros, and S. García, "Ag - doped ZnO thin films prepared by the SILAR method and their application in the photocatalytic degradation of methylene blue," *MRS Adv.*, no. 0123456789, 2024, doi: 10.1557/s43580-024-01013-w.

[23] A. Rana, M. Rana, R. Malik, S. P. Khanna, R. Srivastava, and C. K. Suman, "Effect of Cd-doping on optoelectronic properties of ZnO thin films and their application for MAPbI3 photodetector," *Nano Express*, vol. 5, no. 4, 2024, doi: 10.1088/2632-959X/ad8467.

[24] J. K. Jogi, S. K. Singhal, A. Tanna, M. Singh, and P. Mishra, "Synthesis of ZnO nanostructures and their medical applications," *Oxides for Medical Applications*, pp. 147–165, Jan. 2023, doi: 10.1016/B978-0-323-90538-1.00012-1.

[25] T. Hu, J. Stefania, and M. Quimbayo, "Enhanced photocatalytic degradation of Rhodamine B dye over novel BiOCl / Bi_2O_3 -intercalated bentonite nanocomposites under UV-B and visible light," vol. 80, no. December 2025, 2026, doi: 10.1016/j.surfin.2025.108370.

[26] H. K. Hakki and M. Sillanpää, "Comprehensive analysis of photocatalytic and photoreactor challenges in photocatalytic wastewater treatment: A case study with ZnO photocatalyst," *Mater. Sci. Semicond. Process.*, vol. 181, no. April, 2024, doi: 10.1016/j.mssp.2024.108592.

[27] A. J. Bard, "Photoelectrochemistry and heterogeneous photo-catalysis at semiconductors," *Journal of Photochemistry*, vol. 10, no. 1, pp. 59–75, Jan. 1979, doi: 10.1016/0047-2670(79)80037-4.

[28] B. Kharroubi *et al.*, "Photocatalytic efficiency of undoped and Cu-doped ZnO thin films coated inside transparent glass tube as one-piece photoreactor," *Appl. Surf. Sci.*, vol. 601, no. January, p. 154121, 2022, doi: 10.1016/j.apsusc.2022.154121.

[29] A. Pradhan *et al.*, "Probing antibacterial activity of ZnO and ZnO:S thin films against E. coli and S. typhi with structural, optical and electrical properties," *Inorg. Chem. Commun.*, vol. 184, no. September 2025, p. 115865, Feb. 2026, doi: 10.1016/j.inoche.2025.115865.

[30] C. Mrabet, R. Jaballah, N. Mahdhi, A. Boukhachem, and M. Amlouk, "Structural, optical, photoluminescence and sunlight photocatalytic properties of sprayed NiO-ZnO nanocomposite thin films," *Materials Science and Engineering: B*, vol. 300, no. October 2023, p. 117130, 2024, doi: 10.1016/j.mseb.2023.117130.

[31] K. Lahouel, A. Boumaza, A. Djelloul, and M. Gasmi, "Effect of sulfur-modified zinc oxide thin layers on structural, morphological, optical, and photocatalytic properties for environmental applications," *Inorg. Chem. Commun.*, vol. 182, no. P1, p. 115483, 2025,

doi: 10.1016/j.inoche.2025.115483.

[32] M. Gasmi, A. Djelloul, S. Iaiche, K. Lahouel, and N. Baydogan, "Excellent photocatalytic activity of ZnO-NiO heterojunction thin fi lm in the sunlight range with enhanced of UV photodetection behavior," *J. Solgel Sci. Technol.*, 2025, doi: 10.1007/s10971-025-06728-2.

[33] C. Ravidhas *et al.*, "Tunable morphology with selective faceted growth of visible light active TiO2 thin films by facile hydrothermal method: structural, optical and photocatalytic properties," *Journal of Materials Science: Materials in Electronics*, vol. 27, no. 5, pp. 5020–5032, 2016, doi: 10.1007/s10854-016-4389-5.

[34] D. A. S. Mulus, M. D. Permana, Y. Deawati, and D. R. Eddy, "A current review of TiO2 thin films: synthesis and modification effect to the mechanism and photocatalytic activity," *Applied Surface Science Advances*, vol. 27, no. April, p. 100746, 2025, doi: 10.1016/j.apsadv.2025.100746.

[35] A. Šuligoj, R. Cerc Korošec, G. Žerjav, N. Novak Tušar, and U. Lavrenčič Štangar, *Solar-Driven Photocatalytic Films: Synthesis Approaches, Factors Affecting Environmental Activity, and Characterization Features*, vol. 380, no. 6. Springer International Publishing, 2022. doi: 10.1007/s41061-022-00409-2.

[36] C. Zhu and X. Wang, "Nanomaterial ZnO Synthesis and Its Photocatalytic Applications: A Review," *Nanomaterials*, vol. 15, no. 9, pp. 1–32, 2025, doi: 10.3390/nano15090682.

[37] S. A. M. Abdel-Hameed, F. H. Margha, O. N. Almasarawi, and M. A. Marzouk, "Synthesis, Characterization, and Photoluminescence Properties of High and Low-Temperature Dimorphs of Pb2WO5 Glass-Ceramic for Photocatalytic Application," *J. Inorg. Organomet. Polym. Mater.*, vol. 35, no. 7, pp. 5631–5650, 2025, doi: 10.1007/s10904-025-03612-y.

[38] V. Ho *et al.*, "Robustness of visible-light photocatalytic degradation of volatile organic compounds using Wolfram-doped TiO 2 anatase," *Chem. Eng. Commun.*, vol. 212, pp. 1–16, Jun. 2025, doi: 10.1080/00986445.2024.2445222.

[39] X. Ren, R. Chen, S. Ding, and N. Fu, "Preparation and photocatalytic performance of a magnetically recyclable ZnFe2O4@TiO2@Ag2O p-n/Z-type tandem heterojunction photocatalyst: Degradation pathway and mechanism," *Colloids Surf. A Physicochem. Eng. Asp.*, vol. 658, p. 130604, Feb. 2023, doi: 10.1016/J.COLSURFA.2022.130604.

[40] M. Z. Shafiq *et al.*, "Enhanced photocatalytic activity of V2O5/ZnO heterostructures for malachite green dye using solar simulator irradiation," *Opt. Mater. (Amst).*, vol. 158, p. 116458, Jan. 2025, doi: 10.1016/J.OPTMAT.2024.116458.

[41] K. Chen, W. Dong, Y. Huang, F. Wang, J. L. Zhou, and W. Li, "Photocatalysis for sustainable energy and environmental protection in construction: A review on surface engineering and emerging synthesis," *J. Environ. Chem. Eng.*, vol. 13, no. 5, p. 117529, 2025, doi: 10.1016/j.jece.2025.117529.

[42] Y. Zhu, Z. Zhang, N. Lu, R. Hua, and B. Dong, "Prolonging charge-separation states by doping lanthanide-ions into {001}/{101} facets-coexposed TiO2 nanosheets for enhancing photocatalytic H2 evolution," *Chinese Journal of Catalysis*, vol. 40, no. 3, pp. 413–423, Mar. 2019, doi: 10.1016/S1872-2067(18)63182-1.

[43] T. Mao, M. Liu, L. Lin, Y. Cheng, and C. Fang, "A Study on Doping and Compound of Zinc Oxide Photocatalysts," *Polymers (Basel).*, vol. 14, no. 21, 2022, doi: 10.3390/polym14214484.

[44] V. Kumari, A. Mittal, J. Jindal, S. Yadav, and N. Kumar, "S-, N- and C-doped ZnO as semiconductor photocatalysts: A review," *Front. Mater. Sci.*, vol. 13, no. 1, pp. 1–22, Mar. 2019, doi: 10.1007/s11706-019-0453-4.

[45] M. Arif, "Tunable photocatalytic activity of metal oxides: designing, principles, parameters, and progress," *J. Environ. Manage.*, vol. 395, p. 127697, Dec. 2025, doi:

10.1016/J.JENVMAN.2025.127697.

[46] P. Aina, S. Lawson, A. A. Rownaghi, and F. Rezaei, "Abatement of Indoor Formaldehyde Vapor via Sequential Adsorption and Photocatalytic Degradation over HKUST-1@TiO2 Nanocomposites," *Ind. Eng. Chem. Res.*, vol. 64, no. 7, pp. 3989–4000, Feb. 2025, doi: 10.1021/acs.iecr.4c03052.

[47] M. Yasar *et al.*, "Synergistic effect of Al doping and sol-gel synthesis on the photocatalytic degradation of ciprofloxacin," *J. Solgel Sci. Technol.*, vol. 115, no. 3, pp. 1374–1390, 2025, doi: 10.1007/s10971-025-06832-3.

[48] M. Hajji, A. Akkari, A. Garcia-Loureiro, and N. T. Kamoun, "Bi and Bi-Ni Codoped CuO-ZnO Mixed Oxides: Advanced Catalysts for Efficient Rifampicin Degradation: Influence of Catalyst Dosage, pH, and Scavengers," *Chemistry Africa*, vol. 8, no. 7, pp. 3125–3138, 2025, doi: 10.1007/s42250-025-01252-w.

[49] V. Natarajan, K. Sathiyamoorthy, R. T. Kumar, M. Navaneethan, and S. Harish, "Effect of Yttrium on structural, optical, morphological, magnetic and photocatalytic properties of CuO nanostructures," *Journal of Materials Science: Materials in Electronics*, vol. 36, no. 4, p. 282, 2025, doi: 10.1007/s10854-025-14283-3.

[50] M. C. Naranthatta, A. Pullanhi, and S. T. Malikayil, "Morphological variations of hydrothermally synthesised ZnO nanostructures and its impact on optical properties and photocatalytic degradation of methylene blue," *Reaction Kinetics, Mechanisms and Catalysis*, vol. 138, no. 1, pp. 375–391, 2025, doi: 10.1007/s11144-024-02759-y.

[51] L. Yosefi, M. Haghighi, and S. Allahyari, "Solvothermal synthesis of flowerlike p-BiOI/n-ZnFe2O4 with enhanced visible light driven nanophotocatalyst used in removal of acid orange 7 from wastewater," *Sep. Purif. Technol.*, vol. 178, pp. 18–28, May 2017, doi: 10.1016/J.SEPPUR.2017.01.005.

[52] X. Li *et al.*, "Challenges of photocatalysis and their coping strategies," *Chem Catalysis*, vol. 2, no. 6, pp. 1315–1345, 2022, doi: 10.1016/j.checat.2022.04.007.

[53] Z. Warren, J. Wenk, and D. Mattia, "Increased photocorrosion resistance of ZnO foams via transition metal doping," *RSC Adv.*, vol. 13, no. 4, pp. 2438–2450, 2023, doi: 10.1039/d2ra06730g.

[54] R. A. Surmenev and M. A. Surmeneva, "The influence of the flexoelectric effect on materials properties with the emphasis on photovoltaic and related applications: A review," *Materials Today*, vol. 67, pp. 256–298, Jul. 2023, doi: 10.1016/J.MATTOD.2023.05.026.

[55] K. Ramakrishnan, B. Ajitha, and Y. Ashok Kumar Reddy, "Review on metal sulfide-based nanostructures for photodetectors: From ultraviolet to infrared regions," *Sens. Actuators A Phys.*, vol. 349, p. 114051, Jan. 2023, doi: 10.1016/J.SNA.2022.114051.

[56] V. Selamneni and P. Sahatiya, "Mixed dimensional Transition Metal Dichalcogenides (TMDs) vdW Heterostructure based Photodetectors: A review," *Microelectron. Eng.*, vol. 269, p. 111926, Jan. 2023, doi: 10.1016/J.MEE.2022.111926.

[57] N. Mokrani, "Synthèse et caractérisation des couches minces à base d ' oxyde pour l ' application photocatalytique Présentée par : Synthesis and characterization of oxide-based thin films for photocatalytic application," 2025.

[58] F. Lévy, "Film Growth and Epitaxy: Methods," *Reference Module in Materials Science and Materials Engineering*, no. April 2015, pp. 1–16, 2016, doi: 10.1016/b978-0-12-803581-8.01012-2.

[59] I. A. Neacşu, A. I. Nicoară, O. R. Vasile, and B. Ş. Vasile, "Inorganic micro- and nanostructured implants for tissue engineering," *Nanobiomaterials in Hard Tissue Engineering: Applications of Nanobiomaterials*, pp. 271–295, Jan. 2016, doi: 10.1016/B978-0-323-42862-0.00009-2.

[60] Y. F. Ma *et al.*, "Review of roll-to-roll fabrication techniques for colloidal quantum dot

solar cells," *Journal of Electronic Science and Technology*, vol. 21, no. 1, p. 100189, Mar. 2023, doi: 10.1016/J.JNLEST.2023.100189.

[61] L. Nagyal, S. S. Gupta, R. Singh, A. Kumar, and P. Chaudhary, "Sol – Gel Deposition of Thin Films 2 Film Formation and Methods of Thin-Film Deposition," no. Figure 1, pp. 1–18, 2019.

[62] A. Jilani, M. S. Abdel-wahab, and A. H. Hammad, "Advance Deposition Techniques for Thin Film and Coating," *Modern Technologies for Creating the Thin-film Systems and Coatings*, 2017, doi: 10.5772/65702.

[63] *https://doi.org/10.1007/978-981-99-0961-2*.

[64] D. D. Le Pevelen, *X-ray crystallography of small molecules: Theory and workflow*, 3rd ed. Elsevier Ltd., 2016. doi: 10.1016/B978-0-12-409547-2.05260-4.

[65] "https://www.bruker.com/en/products-and-solutions/diffractometers-and-x-ray-microscopes/x-ray-diffractometers/d8-advance-family/d8-advance.ht."

[66] D. K. Unruh and T. Z. Forbes, "X-ray Diffraction Techniques," in *Analytical Geomicrobiology: A Handbook of Instrumental Techniques*, J. P. L. Kenney, H. Veeramani, and D. S. E. Alessi, Eds., Cambridge University Press, 2019, pp. 215–237.

[67] A. Alasmari, A. A. Awad, and A. A. Aboud, "Investigating the influence of yttrium doping on physical properties of ZnO thin films deposited via spray pyrolysis," *Opt. Mater. (Amst).*, vol. 148, no. January, p. 114899, 2024, doi: 10.1016/j.optmat.2024.114899.

[68] A. S. Enigochitra, P. Perumal, C. Sanjeeviraja, D. Deivamani, and M. Boomashri, "Influence of substrate temperature on structural and optical properties of ZnO thin films prepared by cost-effective chemical spray pyrolysis technique," *Superlattices Microstruct.*, vol. 90, pp. 313–320, 2016, doi: 10.1016/j.spmi.2015.10.026.

[69] M. Sathya *et al.*, "Photocatalytic Degradation Properties of SILAR Grown ZnO:Ag Thin Films: Investigation on the Effect of Ag Loading," *Brazilian Journal of Physics*, vol. 52, no. 1, pp. 1–11, Feb. 2022, doi: 10.1007/s13538-021-01026-y.

[70] B. Dikra *et al.*, "Improvement of photocatalytic performance and sensitive ultraviolet photodetectors using AC-ZnO/ZC-Ag2O/AZ-CuO multilayers nanocomposite prepared by spin coating method," *Journal of Science: Advanced Materials and Devices*, vol. 9, no. 1, p. 100642, Mar. 2024, doi: 10.1016/j.jsamd.2023.100642.

[71] A. Tiwari and P. P. Sahay, "Physica B : Physics of Condensed Matter Modification in the physical properties of nanocrystalline ZnO thin films by Sn / Ni co-doping for transparent conductive oxide applications," *Physica B: Physics of Condensed Matter*, vol. 629, no. November 2021, p. 413638, 2022, doi: 10.1016/j.physb.2021.413638.

[72] H. Saadi, F. I. H. Rhouma, Z. Benzarti, Z. Bougrioua, S. Guermazi, and K. Khirouni, "Electrical conductivity improvement of Fe doped ZnO nanopowders," *Mater. Res. Bull.*, vol. 129, no. November 2019, p. 110884, 2020, doi: 10.1016/j.materresbull.2020.110884.

[73] G. Vijayaprasath, R. Murugan, G. Ravi, T. Mahalingam, and Y. Hayakawa, "Characterization of dilute magnetic semiconducting transition metal doped ZnO thin films by sol-gel spin coating method," *Appl. Surf. Sci.*, vol. 313, pp. 870–876, 2014, doi: 10.1016/j.apsusc.2014.06.093.

[74] S. Khera and P. Chand, "Influence of different solvents on the structural, optical, impedance and dielectric properties of ZnO nanoflakes," *Chinese Journal of Physics*, vol. 57, no. December 2018, pp. 28–46, Feb. 2019, doi: 10.1016/j.cjph.2018.12.015.

[75] R. Majumder, S. Kundu, M. P Chowdhury, M. P. Chowdhury, and M. P Chowdhury, "Investigation of ambient regulated enhanced photo-responsive properties of GO-ZnO and transition metal doped GO-ZnO nanocomposite: Improved photocurrent and swift response," *Opt. Mater. (Amst).*, vol. 142, no. June, p. 113981, Aug. 2023, doi:

10.1016/j.optmat.2023.113981.
[76] "DOI https://doi.org/10.1007/978-1-0716-4406-5."
[77] "https://asrc.gc.cuny.edu/instruments/thermo-scientific-quattro-esem/."
[78] M. Biology, *Spermatology*.
[79] J. Bernardi, "Energy-dispersive X-ray spectroscopy," *Imaging Modalities for Biological and Preclinical Research: A Compendium, Volume 1: Part I: Ex vivo biological imaging*, vol. 1, p. I.9.e-1-I.9.e-9, 2021, doi: 10.1088/978-0-7503-3059-6ch41.
[80] Z. P. Tshabalala, D. N. Oosthuizen, H. C. Swart, and D. E. Motaung, "Tools and techniques for characterization and evaluation of nanosensors," *Nanosensors for Smart Cities*, pp. 85–110, Jan. 2020, doi: 10.1016/B978-0-12-819870-4.00005-0.
[81] W. C. Sanders, *Tip-Sample Forces*. 2019. doi: 10.1201/9780429266553-2.
[82] F. Sumbul and F. Rico, *Single-molecule force spectroscopy: Experiments, analysis, and simulations*, vol. 1886. 2019. doi: 10.1007/978-1-4939-8894-5_9.
[83] Z. Chen, H. N. Dinh, and E. Miller, "Photoelectrochemical water splitting: standards, experimental methods, and protocols," p. 126, 2013, doi: 10.1007/978-1-4614-8298-7.
[84] A. Mahroug *et al.*, "Optical, luminescence, photocurrent and structural properties of sol-gel ZnO fibrous structure thin films for optoelectronic applications: A combined experimental and DFT study," *Opt. Mater. (Amst).*, vol. 142, no. May, p. 114043, Aug. 2023, doi: 10.1016/j.optmat.2023.114043.
[85] G. Demircan *et al.*, "The effect of Co and Mn Co-Doping on structural and optical properties of ZnO thin films," *Opt. Mater. (Amst).*, vol. 126, no. February, 2022, doi: 10.1016/j.optmat.2022.112163.
[86] A. O. Oluwole and O. S. Olatunji, "Photocatalytic degradation of tetracycline in aqueous systems under visible light irridiation using needle-like SnO2 nanoparticles anchored on exfoliated g-C3N4," *Environ. Sci. Eur.*, vol. 34, no. 1, 2022, doi: 10.1186/s12302-021-00588-7.
[87] J. Liu *et al.*, "Highly efficient photocatalytic degradation of oil pollutants by oxygen deficient SnO2 quantum dots for water remediation," *Chemical Engineering Journal*, vol. 404, p. 127146, Jan. 2021, doi: 10.1016/J.CEJ.2020.127146.
[88] M. Zerouali *et al.*, "Effect of Zn-doped CuO thin films on structural, morphological, optical, and electrical properties for photocatalysis application," *Opt. Mater. (Amst).*, vol. 152, no. 1, pp. 473–490, 2024, doi: 10.1016/j.optmat.2024.115495.
[89] K. Ozel, "Strain-induced photoresponsivity in gallium-doped ZnO thin film based UV photodetectors," *Sens. Actuators A Phys.*, vol. 366, no. September 2023, p. 114953, 2024, doi: 10.1016/j.sna.2023.114953.
[90] B. Tan *et al.*, "Space-limited domain annealing of CuI thin films for highly responsive ZnO nanorods based ultraviolet photodetectors," *Mater. Sci. Semicond. Process.*, vol. 134, no. June, p. 106008, 2021, doi: 10.1016/j.mssp.2021.106008.
[91] Z. Mirzaeifard, Z. Shariatinia, M. Jourshabani, and S. M. Rezaei Darvishi, "ZnO Photocatalyst Revisited: Effective Photocatalytic Degradation of Emerging Contaminants Using S-Doped ZnO Nanoparticles under Visible Light Radiation," *Ind. Eng. Chem. Res.*, vol. 59, no. 36, pp. 15894–15911, 2020, doi: 10.1021/acs.iecr.0c03192.
[92] Y. Rati *et al.*, "Visible light assisted degradation of Rhodamin B by reusable S-doped ZnO thin film photocatalyst," *Opt. Mater. (Amst).*, vol. 135, no. December 2022, p. 113370, Jan. 2023, doi: 10.1016/j.optmat.2022.113370.
[93] N. Allouche *et al.*, "Morphological and optical characterization of spin-coated CuO nanostructured thin films doped with V, Na, Ba, and Er for enhanced CO2 sensing," *Journal of Materials Research and Technology*, vol. 35, no. September 2024, pp. 379–391, 2025, doi: 10.1016/j.jmrt.2025.01.048.
[94] A. K. Ambedkar *et al.*, "Structural, optical and thermoelectric properties of Al-doped

ZnO thin films prepared by spray pyrolysis," *Surfaces and Interfaces*, vol. 19, no. March, p. 100504, 2020, doi: 10.1016/j.surfin.2020.100504.

[95] R. Sagheer, M. Khalil, V. Abbas, Z. N. Kayani, U. Tariq, and F. Ashraf, "Effect of Mg doping on structural, morphological, optical and thermal properties of ZnO nanoparticles," *Optik (Stuttg).*, vol. 200, no. May 2019, 2020, doi: 10.1016/j.ijleo.2019.163428.

[96] A. El Hamidi, E. El Mahboub, K. Meziane, A. El Hichou, and A. Almaggoussi, "The effect of electronegativity on optical properties of Mg doped ZnO," *Optik (Stuttg).*, vol. 241, no. March, p. 167070, 2021, doi: 10.1016/j.ijleo.2021.167070.

[97] R. Baghdad *et al.*, "Structural and magnetic properties of Co-doped ZnO thin films grown by ultrasonic spray pyrolysis method," *Superlattices Microstruct.*, vol. 104, no. 2017, pp. 553–569, 2017, doi: 10.1016/j.spmi.2016.11.069.

[98] T. D. Rani, K. Tamilarasan, K. Thangaraj, E. Elamurugu, K. Ramamurthi, and S. Leela, "Structural and optical properties of Nd3+ doped zinc oxide thin films deposited by spray pyrolysis," *Optik (Stuttg).*, vol. 127, no. 1, pp. 72–75, 2016, doi: 10.1016/j.ijleo.2015.10.007.

[99] A. Tiwari and P. P. Sahay, "Improved transparent conductive properties of highly c-axis oriented ZnO thin films upon (Ga, Mg) co-doping," *Micro and Nanostructures*, vol. 181, no. June, p. 207617, 2023, doi: 10.1016/j.micrna.2023.207617.

[100] A. Goktas, F. Aslan, B. Yeşilata, and Boz, "Physical properties of solution processable n-type Fe and Al co-doped ZnO nanostructured thin films: Role of Al doping levels and annealing," *Mater. Sci. Semicond. Process.*, vol. 75, no. November 2017, pp. 221–233, 2018, doi: 10.1016/j.mssp.2017.11.033.

[101] B. B. Straumal *et al.*, "Ferromagnetic behaviour of ZnO: The role of grain boundaries," *Beilstein Journal of Nanotechnology*, vol. 7, no. 1, pp. 1936–1947, 2016, doi: 10.3762/bjnano.7.185.

[102] X. Y. Xie *et al.*, "Synthesis of S-doped ZnO by the interaction of sulfur with zinc salt in PEG200," *J. Alloys Compd.*, vol. 644, pp. 383–389, 2015, doi: 10.1016/j.jallcom.2015.04.214.

[103] B. Brioual *et al.*, "Influence of Hf doping on structural, morphological, optical and electrochemical properties of NiO thin films: Electrochromic application," *J. Solid State Chem.*, vol. 333, no. February, p. 124637, 2024, doi: 10.1016/j.jssc.2024.124637.

[104] S. Besra *et al.*, "Facile synthesis and characterization of ZnO:Al/ZnS/NiO heterojunction thin films with enhanced photocatalytic activities," *Solid State Sci.*, vol. 143, no. August, p. 107282, 2023, doi: 10.1016/j.solidstatesciences.2023.107282.

[105] Y. M. Hunge *et al.*, "Oxidative degradation of benzoic acid using spray deposited WO3/TiO2 thin films," *Journal of Materials Science: Materials in Electronics*, vol. 28, no. 23, pp. 17976–17984, 2017, doi: 10.1007/s10854-017-7740-6.

[106] A. S. Hassanien, "Studies on dielectric properties, opto-electrical parameters and electronic polarizability of thermally evaporated amorphous Cd50S50−xSex thin films," *J. Alloys Compd.*, vol. 671, pp. 566–578, Jun. 2016, doi: 10.1016/J.JALLCOM.2016.02.126.

[107] A. S. Hassanien and A. A. Akl, "Influence of composition on optical and dispersion parameters of thermally evaporated non-crystalline Cd50S50−xSex thin films," *J. Alloys Compd.*, vol. 648, pp. 280–290, Nov. 2015, doi: 10.1016/J.JALLCOM.2015.06.231.

[108] I. Sharma, P. Sharma, and A. S. Hassanien, "Optical properties and optoelectrical parameters of the quaternary chalcogenide amorphous Ge15SnxS35-xTe50 films," *J. Non. Cryst. Solids*, vol. 590, p. 121673, Aug. 2022, doi: 10.1016/J.JNONCRYSOL.2022.121673.

[109] A. S. Hassanien, "Intensive linear and nonlinear optical studies of thermally evaporated

amorphous thin Cu-Ge-Se-Te films," *J. Non. Cryst. Solids*, vol. 586, p. 121563, Jun. 2022, doi: 10.1016/J.JNONCRYSOL.2022.121563.

[110] E. B. Buzok, S. Yalcin, G. Demircan, D. Yılmaz, B. Aktas, and E. Aytar, "The structural, optical, electrical and radiation shielding properties of Co-doped ZnO thin films," *Radiation Physics and Chemistry*, vol. 222, no. November 2023, p. 111840, 2024, doi: 10.1016/j.radphyschem.2024.111840.

[111] A. S. Rini, Y. Rati, A. A. Umar, and N. A. Abdullah, "Investigation of structural, morphological and optical properties of sulfur doped zinc oxide nanorod," *International Journal of Nanoelectronics and Materials*, vol. 13, no. Special issue NANOSYM 2019, pp. 21–32, 2020.

[112] M. Dutta, S. Mridha, and D. Basak, "Effect of sol concentration on the properties of ZnO thin films prepared by sol–gel technique," vol. 254, no. 9, pp. 2743–2747, Feb. 2008, doi: 10.1016/J.APSUSC.2007.10.009.

[113] D. Li *et al.*, "Effects of particle size on the structure and photocatalytic performance by alkali-treated TiO2," *Nanomaterials*, vol. 10, no. 3, pp. 1–14, 2020, doi: 10.3390/nano10030546.

[114] A. M. Mohammed, S. S. Mohtar, F. Aziz, S. A. Mhamad, and M. Aziz, "Review of various strategies to boost the photocatalytic activity of the cuprous oxide-based photocatalyst," *J. Environ. Chem. Eng.*, vol. 9, no. 2, p. 105138, Apr. 2021, doi: 10.1016/J.JECE.2021.105138.

[115] F. Atay and O. Gultepe, "Structural, optical and surface properties of sol–gel-derived boron-doped ZnO films for photocatalytic applications," *Appl. Phys. A Mater. Sci. Process.*, vol. 128, no. 2, Feb. 2022, doi: 10.1007/s00339-022-05261-1.

[116] B. Al Farsi, F. Al Marzouqi, M. Al-Maashani, M. T. Souier, M. Tay Zar Myint, and M. Z. Al-Abri, "Rapid microwave-assisted fabrication of Al-doped zinc oxide nanorods on a glass substrate for photocatalytic degradation of phenol under visible light irradiation," *Materials Science and Engineering: B*, vol. 264, p. 114977, Feb. 2021, doi: 10.1016/J.MSEB.2020.114977.

[117] J. S. Luis *et al.*, "S-doped ZnO photoelectrode modified with silver and platinum nanoparticles and their photocatalytic activity for progesterone degradation," *J. Mol. Struct.*, vol. 1305, no. August 2023, 2024, doi: 10.1016/j.molstruc.2024.137764.

[118] M. M. H. Tusher *et al.*, "Impact of Mg-doping on morphology, structure, optical properties, and enhancing photocatalytic performance of ZnO thin films, prepared by sol–gel spin-coated method," *Vietnam Journal of Chemistry*, vol. 62, no. 4, pp. 566–577, 2024, doi: 10.1002/vjch.202300191.

[119] A. Muhammed, T. G. Asere, and T. F. Diriba, "Photocatalytic and Antimicrobial Properties of ZnO and Mg-Doped ZnO Nanoparticles Synthesized Using Lupinus albus Leaf Extract," *ACS Omega*, vol. 9, no. 2, pp. 2480–2490, 2024, doi: 10.1021/acsomega.3c07093.

[120] H. Barkat, E. G. Temam, H. Ben Temam, N. Mokrani, S. Rahmane, and M. Althamthami, "Enhancing Sunlight-Driven Photocatalysis: High Transparency and Hydrophilic Advancements in Ba-Doped ZnO Thin Films," *J. Mater. Eng. Perform.*, 2024, doi: 10.1007/s11665-024-10126-0.

[121] N. Mokrani, E. Guettaf Temam, H. Barkat, H. Ben Temam, S. Rahmane, and M. Althamthami, "Boosting photocatalytic stability: hydrophilic Sr-doped ZnO thin films prepared via the SILAR method for enhanced performance over multiple cycles," *Phys. Scr.*, vol. 99, no. 9, p. 0959a4, 2024, doi: 10.1088/1402-4896/ad6ffb.

[122] R. Peter *et al.*, "Large enhancement of visible light photocatalytic efficiency of ZnO films doped in-situ by copper during atomic layer deposition growth," *Ceram. Int.*, no. August, 2023, doi: 10.1016/j.ceramint.2023.08.196.

[123] W. Vallejo, A. Cantillo, and C. Díaz-Uribe, "Improvement of the photocatalytic activity of ZnO thin films doped with manganese," *Heliyon*, vol. 9, no. 10, p. e20809, 2023, doi: 10.1016/j.heliyon.2023.e20809.
[124] M. Sathya *et al.*, "Synthesis and characterization of cadmium doped on ZnO thin films prepared by SILAR method for photocatalytic degradation properties of MB under UV irradiation," *The European Physical Journal Plus*, vol. 138, no. 1, p. 67, 2023, doi: 10.1140/epjp/s13360-023-03667-1.
[125] S. Roguai and A. Djelloul, "Efficient methylene blue degradation with spray-deposited ZnO, and V-doped ZnO thin films photocatalysts," *Reaction Kinetics, Mechanisms and Catalysis*, no. 0123456789, 2025, doi: 10.1007/s11144-025-02795-2.
[126] M. Sathya *et al.*, "Photocatalytic Degradation Properties of SILAR Grown ZnO:Ag Thin Films: Investigation on the Effect of Ag Loading," *Brazilian Journal of Physics*, vol. 52, no. 1, Feb. 2022, doi: 10.1007/s13538-021-01026-y.
[127] Y. Gündoğdu, S. Dursun, S. Yiğit Gezgin, and H. Ş. Kiliç, "Femtosecond laser-induced production of ZnO@Ag nanocomposites for an improvement in photocatalytic efficiency in the degradation of organic pollutants," *Opt. Laser Technol.*, vol. 170, no. April 2023, 2024, doi: 10.1016/j.optlastec.2023.110291.
[128] M. Irfan *et al.*, "Improving photocatalytic efficiency of ZnO nanoflowers through gold incorporation for Rhodamine B photodegradation," *Opt. Mater. (Amst).*, vol. 154, p. 115681, Aug. 2024, doi: 10.1016/J.OPTMAT.2024.115681.
[129] H. M. W. Safdar, E. Muhammad, A. Ullah, and T. Jan, "Photoluminescence, Raman scattering and photocatalytic properties of Pd doped ZnO nanostructures synthesized via wet chemical route," *Chemical Papers*, 2025, doi: 10.1007/s11696-025-04003-w.
[130] S. Roguai and A. Djelloul, "ZnO and La-doped ZnO films by USP method and their characterizations for ultraviolet photodetectors and photocatalysis applications," *Inorg. Chem. Commun.*, vol. 157, no. August, p. 111372, 2023, doi: 10.1016/j.inoche.2023.111372.
[131] P. Pascariu, C. Cojocaru, P. Samoila, and C. Romanitan, "Nd-Doped ZnO Nanostructures with Enhanced Photocatalytic Performance for Environmental Protection," *Int. J. Mol. Sci.*, vol. 24, no. 7, 2023, doi: 10.3390/ijms24076436.
[132] O. K. Hussien *et al.*, "Synthesis, characterization of Gd-doped ZnO nanocrystals and their photocatalytic activity in the degradation of C.I. Acid Red 18," *Inorganica Chim. Acta*, vol. 565, p. 121996, May 2024, doi: 10.1016/J.ICA.2024.121996.
[133] A. Joy *et al.*, "Solar photocatalysts: non-metal (C, N, and S)-doped ZnO synthesized through an industrially sustainable in situ approach for environmental remediation applications," *RSC Adv.*, vol. 14, no. 30, pp. 21655–21667, 2024, doi: 10.1039/d4ra03492a.
[134] M. Shaban, M. Mustafa, and A. M. El Sayed, "Structural, optical, and photocatalytic properties of the spray deposited nanoporous CdS thin films; influence of copper doping, annealing, and deposition parameters," *Mater. Sci. Semicond. Process.*, vol. 56, pp. 329–343, Dec. 2016, doi: 10.1016/J.MSSP.2016.09.006.
[135] J. C. Moore, R. Louder, and C. V. Thompson, "Photocatalytic activity and stability of porous polycrystalline ZnO thin-films grown via a two-step thermal oxidation process," *Coatings*, vol. 4, no. 3, pp. 651–669, 2014, doi: 10.3390/coatings4030651.
[136] A. S. Altowyan, J. Hakami, H. Algarni, and M. Shkir, "A highly sensitive rare earth erbium doped In2S3 thin films for photodetection applications," *Inorg. Chem. Commun.*, vol. 153, no. April, p. 110738, 2023, doi: 10.1016/j.inoche.2023.110738.
[137] M. A. Hassan, M. H. Mohsin, and R. A. Ismail, "Preparation of high-responsivity strontium–doped CuO/Si heterojunction photodetector by spray pyrolysis," *Journal of Materials Science: Materials in Electronics*, vol. 34, no. 10, p. 912, 2023, doi:

10.1007/s10854-023-10348-3.
[138] F. Abbasi, F. Zahedi, and M. hasan Yousefi, "Performance improvement of UV photodetectors using Cd-doped ZnO nanostructures," *Journal of Materials Science: Materials in Electronics*, vol. 32, no. 14, pp. 19614–19625, 2021, doi: 10.1007/s10854-021-06482-5.
[139] M. Shkir, M. T. Khan, and A. Khan, "Impact of Mo doping on photo-sensing properties of ZnO thin films for advanced photodetection applications," *J. Alloys Compd.*, vol. 985, no. February, p. 174009, May 2024, doi: 10.1016/j.jallcom.2024.174009.
[140] S. Aksoy Pehlivanoglu and O. Polat, "Exploring the structural and optical properties of Ir-doped ZnO thin films," *Opt. Mater. (Amst).*, vol. 143, no. April, p. 114179, 2023, doi: 10.1016/j.optmat.2023.114179.
[141] B. Wang *et al.*, "Influences of Co doping on the structural, optical and magnetic properties of ZnO nanorods synthesized by hydrothermal route," *Solid State Sci.*, vol. 11, no. 8, pp. 1419–1422, 2009, doi: 10.1016/j.solidstatesciences.2009.04.024.
[142] "Investigation of the effect of material structure on radiation protection by Monte Carlo simulation method".
[143] "Structure of solids," *Construction Materials: Their Nature and Behaviour: Fifth Edition*, pp. 47–58, 2017, doi: 10.1201/b16000-44.
[144] B. Rahal, B. Boudine, A. R. Khantoul, M. Sebais, and O. Halimi, "Colloidal synthesis of nanostructured pure ZnO and Cd doped ZnO thin films and their characterization," *Optik (Stuttg).*, vol. 127, no. 17, pp. 6943–6951, 2016, doi: 10.1016/j.ijleo.2016.05.006.
[145] B. Rahal *et al.*, "Sol-gel synthesis and nanostructured semiconductor analysis of undoped and Cd-doped ZnO thin films," *Optik (Stuttg).*, vol. 169, no. March, pp. 303–313, 2018, doi: 10.1016/j.ijleo.2018.05.070.
[146] M. S. Nadeem *et al.*, "Hydrothermally derived co, Ni co-doped ZnO nanorods; structural, optical, and morphological study," *Opt. Mater. (Amst).*, vol. 111, no. November, p. 110606, 2021, doi: 10.1016/j.optmat.2020.110606.
[147] B. Stefano, "Porosity : Exploring the Fascinating World of Empty Spaces," vol. 13, no. March, pp. 1–2, 2023, doi: 10.37421/2090-5025.2023.13.230.
[148] A. Hussain, S. Fiaz, A. Almohammedi, and A. Waqar, "Optimizing photocatalytic performance with AG-doped ZNO nanoparticles: Synthesis and characterization," *Heliyon*, vol. 10, no. 15, 2024, doi: 10.1016/j.heliyon.2024.e35725.
[149] S. S. A. Al Ghafry *et al.*, "Ga-doped ZnO nanorods: The photocatalytic performance of methylene blue under solar irradiation," *Opt. Mater. (Amst).*, vol. 126, no. March, p. 112139, 2022, doi: 10.1016/j.optmat.2022.112139.
[150] D. Upadhaya and D. Dhar Purkayastha, "Enhanced wettability and photocatalytic activity of seed layer assisted one dimensional ZnO nanorods synthesized by hydrothermal method," *Ceram. Int.*, vol. 46, no. 10, pp. 15831–15839, 2020, doi: 10.1016/j.ceramint.2020.03.130.
[151] M. B. Ochang *et al.*, *Influence of Mn content on the optical, structural and electrical properties of spray pyrolysis deposited quinternary Cu2Cd1−xMnxSnS4 thin films for solar cells*, vol. 55, no. 6. Springer US, 2023. doi: 10.1007/s11082-023-04819-4.
[152] R. Sharma, S. Sharda, K. A. Aly, A. Dahshan, and P. Sharma, "Nanocrystallization and optical properties of quaternary Sn–Se–Bi–Te chalcogenide thin films," *Journal of Materials Science: Materials in Electronics*, vol. 33, no. 20, pp. 16320–16333, 2022, doi: 10.1007/s10854-022-08524-y.
[153] F. Haninl *et al.*, "Correlating electronic structure and antibacterial activity in sol–gel synthesized iron-doped TiO_2 nanostructured thin films," *Surfaces and Interfaces*, vol. 72, no. April, p. 106978, 2025, doi: 10.1016/j.surfin.2025.106978.
[154] H. Khan and M. U. H. Shah, "Modification strategies of TiO2 based photocatalysts for

enhanced visible light activity and energy storage ability: A review," *J. Environ. Chem. Eng.*, vol. 11, no. 6, p. 111532, 2023, doi: 10.1016/j.jece.2023.111532.

[155] M. Iliaš and P. Neogrády, "Ionization potentials of Zn, Cd, Hg and dipole polarizabilities of Zn+, Cd+, Hg+: Correlation and relativistic effects," *Chem. Phys. Lett.*, vol. 309, no. 5–6, pp. 441–449, 1999, doi: 10.1016/S0009-2614(99)00665-X.

[156] A. Palai, N. R. Panda, S. Chhotaray, and D. Sahu, "Sm doped ZnO-SnO2 nanocomposites with improved photo-degradation strength and antibacterial properties," *Surfaces and Interfaces*, vol. 41, no. May, p. 103217, 2023, doi: 10.1016/j.surfin.2023.103217.

[157] S. B. Endeshaw, M. Goddati, J. Lee, F. G. Aga, L. T. Tufa, and F. K. Sabir, "ZnO/CuO nanocomposites for enhanced photocatalytic and antibacterial applications: A comparative study of synthesis methods," *Journal of Science: Advanced Materials and Devices*, vol. 10, no. 3, 2025, doi: 10.1016/j.jsamd.2025.100898.

[158] M. F. Lanjwani, M. Tuzen, M. Y. Khuhawar, and T. A. Saleh, "Trends in photocatalytic degradation of organic dye pollutants using nanoparticles: A review," *Inorg. Chem. Commun.*, vol. 159, no. July 2023, p. 111613, 2024, doi: 10.1016/j.inoche.2023.111613.

[159] M. Sellam *et al.*, "Enhanced solar dye degradation using Ni-doped ZnO and SnO thin films," *Solar Energy*, vol. 304, no. July 2025, p. 114198, 2026, doi: 10.1016/j.solener.2025.114198.

[160] O. Kamoun, A. Akkari, B. Alhalaili, R. Vidu, and N. Turki-Kamoun, "Investigations on the synthesis and characterization of silver-doped MoO3 thin films for photocatalytic applications," *Sci. Rep.*, vol. 15, no. 1, pp. 1–16, 2025, doi: 10.1038/s41598-024-84485-y.

[161] S. Khan *et al.*, "Photocatalytic degradation of Rhodamine B dye over Ni–Cd doped and co-doped ZnO nanoparticles," *Sci. Rep.*, vol. 15, no. 1, pp. 1–22, 2025, doi: 10.1038/s41598-025-17684-w.

[162] N. Matinise, N. Botha, A. Fall, and M. Maaza, "Enhanced photocatalytic degradation of methylene blue using zinc vanadate nanomaterials with structural and electrochemical properties," *Sci. Rep.*, vol. 15, no. 1, pp. 1–16, 2025, doi: 10.1038/s41598-025-11418-8.